



Ludimar Lima de Aguiar

**A Three-Dimensional Pipe Beam Finite
Element For Nonlinear Analysis of
Multilayered Risers and Pipelines**

TESE DE DOUTORADO

Thesis presented to the Programa de Pós-Graduação em Engenharia Mecânica of the Departamento de Engenharia Mecânica, PUC-Rio as partial fulfillment of the requirements for the degree of Doutor em Engenharia Mecânica.

Advisor: Prof. Arthur Martins Barbosa Braga

Co-advisor: Prof. Carlos Alberto de Almeida

Rio de Janeiro
November 2013



Ludimar Lima de Aguiar

**A Three-Dimensional Pipe Beam Finite
Element for Nonlinear Analysis of
Multilayered Risers and Pipelines**

Thesis presented to the Programa de Pós-Graduação em Engenharia Mecânica of the Departamento de Engenharia Mecânica, PUC-Rio as partial fulfillment of the requirements for the degree of Doutor em Engenharia Mecânica.

Prof. Arthur Martins Barbosa Braga

Advisor

Mechanical Engineering Department – PUC-Rio

Prof. Carlos Alberto de Almeida

Co-Advisor

Mechanical Engineering Department – PUC-Rio

Prof. Glaucio Hermogenes Paulino

Department of Civil and Environmental Engineering
University of Illinois at Urbana Champaign

D.Sc. Marcio Martins Mourelle

Research and Development Center - Petrobras

Prof. Luis Volnei Sudati Sagrilo

Department of Civil Engineering - UFRJ

Prof. Ivan Fabio Mota de Menezes

Mechanical Engineering Department – PUC-Rio

Prof. José Luiz de França Freire

Mechanical Engineering Department – PUC-Rio

Rio de Janeiro, November 25, 2013

All rights reserved.

Ludimar Lima de Aguiar

Graduated in Civil Engineering from Federal University of Sergipe in 2000 and obtained a MSc. degree in Structural Engineering from University of Brasilia in 2002. Works at Petrobras Research Center on structural analysis of risers, pipelines and offshore structures.

Bibliographic data

Aguiar, Ludimar Lima de

A Three-Dimensional Pipe Beam Finite Element for Nonlinear Analysis of Multilayered Risers and Pipelines / Ludimar Lima de Aguiar; Advisor: Arthur Martins Barbosa Braga; co-advisor: Carlos Alberto de Almeida; 2013.

124f. : il.(color); 30 cm

Tese (Doutorado) – Pontifícia Universidade Católica do Rio de Janeiro, Departamento de Engenharia Mecânica.

Inclui bibliografia

1. Engenharia Mecânica - Teses. 2. Tubos em multicamadas. 3. Escorregamento não-linear. 4. Método dos Elementos Finitos. 5. Análise Dinâmica Não-linear. I. Braga, Arthur Martins Barbosa. II. Almeida, Carlos Alberto de. III. Pontifícia Universidade Católica do Rio de Janeiro, Departamento de Engenharia Mecânica. IV. Título.

CDD: 621

To my family

Acknowledgments

I would like to express my gratitude to Professor Carlos Alberto de Almeida, for his guidance and support in this work. I am really grateful for the opportunity to learn a little from his knowledge.

I also thank Professor Arthur Martins Barbosa Braga to make this thesis possible.

I am also very grateful for the experience I had at the University of Illinois. Thanks a lot to Professor Glaucio H. Paulino and his wife Berta Paulino for this opportunity and for all the support during that journey. I would also like to thank my colleagues at the UIUC for their help and for sharing a little of their experience during this period. I learned a lot at our weekly group meetings.

This work would not have even started without the encouragement and support of my friends Marcio Mourelle, Dary Kayser Jr., and Ivan Menezes. Thanks a lot!

Special thanks to Professor Ivan Menezes for all his advices, always with great enthusiasm and encouraging me to move on. I also thank his team at TecGraf for all the support with the software Anflex.

I would also like to thank my friends and colleagues at Petrobras: Stael Senra, Edmundo Andrade, Marcos André Martins, Ricardo Martins, Divino Cunha, Ana Lucia Torres, Arleide Araujo, and Valeria Santos for their help, support, and encouragement.

I also thank Petrobras, through my managers Arthur Curty Saad and Luiz Augusto Petrus Levy, for allowing and supporting me in this work.

Finally, I wish to thank my lovely wife Patricia Pessoa and my daughters Luana and Isabel. Words cannot express my gratitude for their support.

Abstract

Aguiar, Ludimar Lima de; advisor: Braga, Arthur Martins Barbosa; co-advisor: Almeida, Carlos Alberto de; **A Three-Dimensional Pipe Beam Finite Element For Nonlinear Analysis of Multilayered Risers and Pipelines**. Rio de Janeiro, 2013. 124p. D.Sc. Thesis – Departamento de Engenharia Mecânica, Pontifícia Universidade Católica do Rio de Janeiro.

This work addresses the behavior of three-dimensional multilayered pipe beams with interlayer slip condition, under general three-dimensional large displacements, in global riser and pipeline analysis. A new finite element model, considering the Timoshenko beam for each element layer, has been formulated and implemented. It comprises axial, bending and torsional degrees-of-freedom, all varying along the element length according to discretization using Hermitian functions: constant axial and torsional loadings, and linear bending moments. Transverse shear strains due to bending are also considered in the formulation by including two generalized constant degrees-of-freedom. To represent various friction conditions between the element layers, nonlinear contact models are considered. These conditions are accounted in the model through a proper representation of the constitutive relation for the shear stresses behavior in the binding material. Derivations of hydrostatic and hydrodynamic loadings due to internal and external fluid acting on respective element layers are presented. The drag and inertia forces due to external fluid are calculated by using the Morison equation. Mass and damping matrices, associated to each element layer, are properly derived by adding their respective contributions to the expression of the virtual work due to external loading. The FE implementation allows for the numerical representation of either bonded or unbonded multilayered risers, including small slip effects between layers. Effects of the pipe-soil interaction are also addressed in this work with two contact models considering either no or full interaction between friction forces in longitudinal and lateral directions, respectively. The element formulation and its numerical capabilities are evaluated by some numerical testing, which are compared to other numerical or analytical solutions available in the literature. These tests results show that the proposed element provides a simple yet robust and reliable tool for general multilayered piping analyses.

Keywords

Multi-layered Pipe Beams, Riser Analysis, Interlayer Slip, Finite Element, Nonlinear Dynamic Analysis.

Resumo

Aguiar, Ludimar Lima de; orientador: Braga, Arthur Martins Barbosa; co-orientador: Almeida, Carlos Alberto de; **Um Modelo de Elementos Finitos de Pórtico Tridimensional Para Análise Não-Linear de Risers e Dutos com Multicamadas**. Rio de Janeiro, 2013. 124p. Tese de Doutorado – Departamento de Engenharia Mecânica, Pontifícia Universidade Católica do Rio de Janeiro.

Neste trabalho, o comportamento tridimensional de tubos multicamadas com escorregamento entre camadas, sob grandes deslocamentos, para aplicação em análise global de risers e dutos é avaliado. Foi desenvolvido um novo elemento finito, considerando o modelo de viga de Timoshenko em cada camada. O elemento contempla os graus de liberdade axial, flexional e torcional, todos variando ao longo do elemento de acordo com as funções de interpolação de Hermite: carregamentos axial e torcional constantes e momentos fletores lineares. As deformações de cisalhamento também foram consideradas na formulação do elemento através de graus de liberdades generalizados, constantes ao longo do elemento. A formulação também considera modelos de contato não-lineares para representar várias possibilidades de atrito entre camadas, através da representação apropriada da relação constitutiva para as tensões de cisalhamento no material adesivo. O trabalho também apresenta os carregamentos hidrostáticos e hidrodinâmicos devidos aos fluidos interno e externo, atuando nos graus de liberdade das respectivas camadas. As forças de arrasto e de inércia devidas ao fluido externo foram calculadas através da fórmula de Morison. As matrizes de massa e amortecimento, associadas a cada camada do elemento, são obtidas através da consideração das respectivas contribuições na expressão do trabalho virtual desenvolvido pelo carregamento externo. O elemento finito desenvolvido permite a representação numérica de risers com camadas aderentes ou não aderentes, incluindo os efeitos de pequenos deslocamentos entre camadas. O problema de interação solo-estrutura também é tratado neste trabalho, sendo que dois modelos de contato entre o solo e o duto são propostos. A formulação do elemento e o seu desempenho numérico são avaliados através de alguns exemplos de aplicação e os resultados são comparados com outros resultados numéricos ou analíticos disponíveis na literatura. Os resultados mostram que o novo elemento é uma solução simples, robusta e confiável para análise de tubos em multicamadas.

Palavras-chave

Tubos em Multicamadas, Análise de Risers, Escorregamento entre Camadas, Método dos Elementos Finitos, Análise Dinâmica Não-Linear.

Contents

| | | |
|--------|--|----|
| 1. | Introduction | 16 |
| 2. | Multilayered Pipe Beam Element | 20 |
| 2.1. | Basic Formulation for Large Rotations | 22 |
| 2.2. | Kinematics of Deformation | 23 |
| 2.3. | Finite Element Formulation | 26 |
| 2.4. | Element Displacement Field Interpolation | 27 |
| 2.5. | Element Layer Stiffness Matrices | 31 |
| 2.6. | Element Layer Mass Matrix | 32 |
| 2.7. | Element Layer Damping Matrix | 33 |
| 2.8. | Contact Conditions | 33 |
| 2.9. | Interface Constitutive Model | 36 |
| 2.10. | Interface Stiffness Matrix | 40 |
| 2.11. | Transverse Displacement Compatibility | 42 |
| 2.12. | Element Stiffness Matrix | 44 |
| 3. | Fluid Loads | 46 |
| 3.1. | Fluid Weight and Buoyancy Forces | 46 |
| 3.2. | Hydrodynamic Loads | 47 |
| 4. | Implementation of the Three-Dimensional Multilayer Pipe Beam Element | 50 |
| 4.1. | Global Equilibrium Equation | 50 |
| 4.2. | Element Updating Procedure | 51 |
| 5. | Pipe-Soil Interaction | 55 |
| 5.1. | Normal Reaction | 56 |
| 5.2. | Longitudinal and Lateral Reactions | 57 |
| 5.2.1. | Coupled Friction | 57 |
| 5.2.2. | Uncoupled Friction | 61 |
| 5.3. | Soil Transformation Matrix | 63 |

| | | |
|--------|---|-----|
| 5.4. | Numerical Implementation | 64 |
| 6. | Numerical Tests | 66 |
| 6.1. | Single Layer Models | 66 |
| 6.1.1. | Cantilever Beam Subjected to Pure Bending | 66 |
| 6.1.2. | Composite Column Subjected to Eccentric Axial Loading | 68 |
| 6.1.3. | Out-of-Plane Loading to a Circular Cantilever Beam | 71 |
| 6.2. | Multilayered Beam Models | 75 |
| 6.2.1. | Two Layer Pipe Beam Subjected to Axial Loading | 75 |
| 6.2.2. | Two-Layer Cantilever Beam | 79 |
| 6.2.3. | Two-Layer Cantilever Beam Submitted to Distributed Loading | 83 |
| 6.2.4. | Dynamic Analysis of a Circular Two-Layer Cantilever Beam | 85 |
| 6.2.5. | Two-Layer Cantilever Under Hydrostatic and Hydrodynamic Loading | 86 |
| 6.3. | Multilayered Riser Analysis | 89 |
| 6.3.1. | Flexible Riser in Catenary Configuration | 89 |
| 6.3.2. | Steel Catenary Riser | 93 |
| 7. | Concluding Remarks | 103 |
| 8. | References | 105 |
| | Appendix A: Two Layer Pipe Beam | 109 |
| A.1. | Two Layer Pipe Under Axial Loading | 109 |
| A.2. | Two Layer Pipe Beam Element Under Bending | 113 |
| | Appendix B: Nonlinear Multilayer Pipe Beam Element Matrices | 121 |
| B.1. | Linear Stiffness Matrix | 121 |
| B.2. | Geometric Stiffness Matrix | 122 |
| B.3. | Mass Matrix | 123 |
| B.4. | Interface Stiffness Matrix | 124 |

List of Figures

| | |
|---|----|
| Figure 1: Beam Element Reference Configurations. | 21 |
| Figure 2: Spatial Transformation Between Two Vectors. | 22 |
| Figure 3: Multilayer Element in Two Successive Configurations. | 23 |
| Figure 4: Details of Interface Straining In a Two-Layer Pipe Wall Segment. | 34 |
| Figure 5: Linear Elastic Constitutive Relation - Slip Model Representation. | 34 |
| Figure 6: Layer contact with static friction. | 35 |
| Figure 7: Layer Contact With Kinetic Friction. | 35 |
| Figure 8: Rupture – Multi-Linear Elastic-Perfect Plastic Model. | 36 |
| Figure 9: Directions for Relative Displacements. | 36 |
| Figure 10: Angular Coordinate ϕ at the Interface. | 40 |
| Figure 11: Reference Systems for Penalty Method. | 44 |
| Figure 12: Fluid Load on a Beam Element. | 46 |
| Figure 13: Soil Springs. | 55 |
| Figure 14: Pipe-Soil Relative Displacements. | 56 |
| Figure 15: Normal Contact Model. | 56 |
| Figure 16: Lateral and Longitudinal Contact. | 57 |
| Figure 17: Pipe-Soil Friction Model. | 58 |
| Figure 18: Radial Return Mapping. | 61 |
| Figure 19: Soil Reference System. | 63 |
| Figure 20: Cantilever Beam Under Pure Bending. | 67 |
| Figure 21: Cantilever Beam: Deformed Configurations. | 68 |
| Figure 22: Normalized Displacements at Beam Tip. | 68 |
| Figure 23: Composite Column Under to Eccentric Axial Load. | 69 |
| Figure 24: Composite Column: Deformed Configurations. | 70 |
| Figure 25: Bending Moment Along the Composite Column, for $P=0.2$ kN. | 70 |
| Figure 26: Normalized Displacement at the Top of the Composite Column. | 71 |
| Figure 27: Circular Cantilever Beam Under Transverse Loading. | 72 |
| Figure 28: Circular Cantilever Beam: Deformed Configurations. | 72 |
| Figure 29: Normalized Displacements for the Circular Cantilever Beam. | 73 |
| Figure 30: Two Layer Pipe Beam Under Axial Loading | 76 |

| | |
|--|----|
| Figure 31: Axial displacements – Linear Elastic Slip. | 76 |
| Figure 32: Longitudinal Contact Stresses at the Interface – Linear Elastic Slip. | 77 |
| Figure 33: Contact Stresses at Interface – Slip with Static Friction. | 78 |
| Figure 34: Residual Contact Stresses at Interface After Unloading – Slip With Static Friction. | 78 |
| Figure 35: Applied Load vs. Axial Displacements at the Free End of Each Layer - Slip With Static Friction. | 79 |
| Figure 36: Applied Load vs. Relative Axial Displacement at the Beam Tip - Slip with Static Friction. | 79 |
| Figure 37: Two-Layer Cantilever Beam. | 80 |
| Figure 38: Bending Moment at Each Element Layer (One Material). | 80 |
| Figure 39: Axial Stress Distribution at Mid-Length Cross Section (One Material). | 81 |
| Figure 40: Bending Moment at Each Element Layer (Layers with Different Materials). | 81 |
| Figure 41: Axial Stress Distribution at Mid-Length Cross Section (Different Materials). | 82 |
| Figure 42: Normalized Displacements at the Two-Layer Cantilever Beam Tip. | 82 |
| Figure 43: Properties for the Two-Layer Cantilever Beam Under Distributed Loading. | 83 |
| Figure 44: Beam Tip Displacements – Static Analysis | 84 |
| Figure 45: Beam Tip Displacements – Dynamic Analysis | 85 |
| Figure 46: Geometrical and Material Properties for the Circular Two-Layer Cantilever Beam. | 86 |
| Figure 47: Circular Cantilever Beam Tip Displacements in Dynamics Analysis. | 86 |
| Figure 48: Submerged Cantilever Beam. | 87 |
| Figure 49: Deformed Shapes for Various Loading Conditions. | 88 |
| Figure 50: Vertical Displacements at Beam Tip. | 88 |
| Figure 51: Flexible Riser in Catenary Configuration. | 89 |
| Figure 52: Bending Moment Distribution Along Multilayered Riser. | 91 |
| Figure 53: Dynamic Analysis Results for Multilayered Flexible Riser. | 92 |
| Figure 54: Initial Deformed Configuration for the Steel Catenary Riser. | 93 |
| Figure 55: SCR Pipe Cross Section. | 94 |
| Figure 56: Static Loading for the SCR Model. | 95 |
| Figure 57: Dynamic Loading for the SCR Model. | 95 |
| Figure 58: Deformed Configuration at the end of Static Analysis. | 96 |
| Figure 59: Axial Forces Envelope – Bonded Model. | 98 |

| | |
|--|-----|
| Figure 60: Bending Moment Envelope – Bonded Model. | 99 |
| Figure 61: von Mises Stresses Envelope – Bonded Model. | 99 |
| Figure 62: Axial Forces Envelope – Unbonded Model. | 100 |
| Figure 63: Bending Moment Envelope – Unbonded Model. | 100 |
| Figure 64: von Mises Stresses Envelope – Unbonded Model. | 101 |
| Figure 65: Time History for Axial Force at Top Connection. | 101 |
| Figure 66: Time History for Bending Moment at Touchdown Point. | 102 |

List of Tables

| | |
|---|----|
| Table 1: Slip Model Conditions. | 37 |
| Table 2: Distributed Loads Proportional Coefficients. | 47 |
| Table 3: Comparison of Displacements at the Free End of the Beam. | 73 |
| Table 4: Multilayer Riser Properties. | 90 |
| Table 5: Support Reactions at Top and Bottom Connections. | 90 |
| Table 6: Multilayered SCR Cross Section Properties. | 94 |
| Table 7: Soil Properties for the SCR Model. | 94 |
| Table 8: SCR Static Analysis Numerical Results. | 97 |

Nomenclature

| | |
|--------------------------------|--|
| i | vector index; node index; iteration; |
| t | time; |
| X, Y, Z | local element reference system; |
| x, y, z | nodal reference system; local coordinates on element cross section; |
| k | element layer index; |
| N_{layers} | number of layers; |
| θ | pseudo-vector of rotation; |
| $\theta_x, \theta_y, \theta_z$ | components of rotations about X , Y and Z axis, respectively; |
| \mathbf{u} | displacement vector; |
| u, v, w | components of displacements in X , Y and Z directions, respectively; |
| ϕ_i | Hermitian polynomials; |
| ξ | element coordinate in the longitudinal (X) direction; |
| ℓ | element length; |
| β | generalized degree-of-freedom for shear strain; |
| \mathbf{H} | interpolation matrix; |
| ε_{xx} | normal strain component; |
| γ_{xy}, γ_{xz} | shear strain components; |
| \mathbf{B}_L | compatibility matrix for linear strains; |
| \mathbf{K}_L | linear stiffness matrix; |
| \mathbf{C} | linear-elastic constitutive tensor; |
| φ | angular coordinate at layer or interface cross section; |
| E^k | layer- k material Young modulus; |
| G^k | layer- k material shear modulus; |
| A^k | layer- k cross section area; |
| I^k | layer- k moment of inertia with respect to the cross section axis of symmetry; |
| J^k | layer- k polar moment of inertia with respect to the cross section geometric center; |

| | |
|-------------------------------|---|
| \mathbf{K}_G | geometric stiffness matrix; |
| \mathbf{B}_G | geometric compatibility matrix; |
| $\boldsymbol{\tau}$ | stress components matrix; |
| τ_{xx} | normal stress component; |
| τ_{xy}, τ_{xz} | shear stress components; |
| $\bar{\boldsymbol{\gamma}}_l$ | interlayer slip vector; |
| $\bar{\gamma}_x$ | longitudinal slip component; |
| $\bar{\gamma}_\varphi$ | circumferential slip component; |
| k_c | contact stiffness between layers (slip modulus); |
| k_c^{ep} | nonlinear slip modulus; |
| τ_x, τ_φ | contact stresses between layers in the longitudinal and circumferential directions, respectively; |
| \mathbf{K}_i | interface stiffness matrix; |
| k^p | penalty parameter; |
| \mathbf{K}_p | penalty stiffness matrix; |
| \mathbf{K}_e | element stiffness matrix, in local coordinate system; |
| \mathbf{K}_G | element stiffness matrix, in global coordinate system; |
| \mathbf{f}_e | element internal forces vector, in local coordinate system; |
| \mathbf{f}_p | penalty internal forces vector, in local coordinate system; |
| \mathbf{f}_G | element internal forces vector, in global coordinate system; |
| \mathbf{K} | structure stiffness matrix, in global coordinate system; |
| \mathbf{U} | structure displacement vector, in global coordinate system; |
| \mathbf{R} | external force vector, in global coordinate system; |
| \mathbf{F} | structure internal forces vector, in global coordinate system; |
| \mathbf{R}_e | element rotation matrix; |
| \mathbf{R}_n | nodal rotation matrix; |

1.

Introduction

Multilayered pipelines have been widely used in the petroleum industry to transport almost all types of fluids in the oil production system. Flexible lines are the most common example of this type of structure, which consists of a tubular arrangement of concentric metallic and polymeric material layers. These layers are assembled to give the structure high tensile strength, good thermal insulation and low bending stiffness, so that it can be reeled in large segments without using intermediate connections. In this fashion, flexible lines can be easily installed, uninstalled and reinstalled in various production fields besides such compliant structures are capable of absorbing large displacements, as imposed by the floating production units. Although widely in use, appropriate representation of flexible lines in simulation analysis still represents a great numerical challenge, mainly due to their nonlinear dynamic behavior in global riser analysis and to nonlinearities caused by its multilayered cross section.

An alternative to the use of flexible lines is the use of steel rigid lines, which have both static (pipelines) and dynamic (risers) applications. However, one difficulty when using this type of structure is the need for corrosion resistance due to the types of fluids from the production process. A possible solution is the use of carbon steel pipes coated with corrosion resistant alloys (CRA). Cladded pipelines (CRA metallurgically bonded to carbon steel) have been used in oil and gas industry for over 25 years, to transport corrosive products. Another alternative is the use of lined pipe (CRA mechanically attached to the carbon steel). In both, mechanical design and global riser analyses, with clad or liner, the presence of this additional corrosion-resistant metal layer is generally neglected, mainly due to difficulties of current available numerical models to adequately represent the behavior of multilayered pipes.

In the literature, several analytical and numerical solutions have been proposed since Newmark et al. [1] first proposed a two-layered Euler-Bernoulli beam model considering the linear behavior. More recently, Schnabl et al. [2], Foraboschi [3] and Ecsedi and Baksa [4], proposed analytical solutions for two-layered laminated beams considering interlayer slip condition, but restricted to small displacements and linear constitutive models for each layer material. Some of these papers also included transverse shear deformation in their formulation. Attempts for more general analytical solutions have been proposed by Girhammar and Gopu [5] and Girhammar and Pan [6] who presented exact solutions, for first and second order analysis procedures, allowing estimations for the magnitude of beam deformation and internal actions between layers. They also considered occurrence of partial shear interactions in beam-column analyses. Later, Girhammar [7] derived an approximate second order analysis procedure for the evaluation of composite beam-columns with interlayer slip. Chen et al. [8] presented a solution where the combined action of arbitrary transverse and constant axial loadings, under static conditions, is considered in a non-uniform slip stiffness model. This study was extended by Xu et al. [9] to include dynamics and buckling behavior of partial-interaction composite members, accounting for transverse shear deformations and cross-section rotary inertia. In a later work, these authors proposed extension of their results by using an approximate expression of the beam-column fundamental frequency under axial loading (Wu et al. [10]). In the same line of investigation, numerical methods were also proposed by many authors, mainly based on the finite element method (FEM) approach. A strain-based FEM, based on the Timoshenko beam theory for each element layer, applicable to linear static analysis of two-layer planar composite beams, with interlayer slip, was proposed by Schnabl et al. [11]. Using a similar approach, Čas et al. [12, 13] presented a finite element formulation that considers non-linear time-dependent constitutive models for the element layers and a non-linear relationship between the slip and the shear stress at the interface. In this formulation, the geometrically non-linear Reissner's beam theory was used. Buckling analysis of axially compressed layered wood columns was carried out and the numerical results were compared with the analytical values of Girhammar and Gopu [5]. Krawczyk and Frey [14, 15], proposed a 2D beam element for geometric nonlinear analysis of multilayered beams considering interlayer slip.

The element formulation is based on the co-rotational approach with Timoshenko's beam theory assumptions. The element is assumed to undergo large displacements and rotations, but with small deformations and moderate slip between layers. A 2D model comparing the FEM solutions with extended Euler-Bernoulli's formulation and Timoshenko's beam model of slab beams for various loadings was presented by Zona and Ranzi [16]. It is shown that displacement and stress results in composite members are controlled by the interaction between bending and shear (short or long beams), in each case study. The behavior of general multi-stacked composite beams with interlayer slip was considered by Sousa Jr. and Silva [17] for the rectangular section where curvature locking difficulties were identified. Their model represents the composite beam as an association of beams and interface elements, providing an efficient solution for the multilayered beam problem.

Several studies on multilayer beams are now available in the literature. However most of them have their applications limited to laminated beams under in plane loading only. To the best of the author's knowledge, an appropriate representation of multilayered pipes in three-dimensional nonlinear analysis has not yet been addressed in the literature.

More recently, in a 2-D numerical formulation, a two-layer pipe beam model under Timoshenko's beam assumptions was proposed by Aguiar and Almeida [18], for small displacement analysis under small strain hypothesis. These model capabilities were extended to consider rupture and possible nonlinear slip conditions at the interface material between layers [19]. The proposed model formulation, which is described in details in Appendix A.2, accounts for axial and bending degrees-of-freedom at each layer in a single element model, including the classical beam modes of deformation and nonlinear interlayer shear deformation condition, which is assumed to be constant through the interlayer material thickness, for all loading conditions. In this model, damage at the interface is accounted by considering a yielding-type function for the interface material constitutive model, in a nonlinear fashion of analysis.

In the present work, these recently proposed model capabilities have been extended to consider the nonlinear behavior of multilayered risers and pipelines in general 3-D large displacement representations. An updated Lagrangian

formulation is employed including large displacements and rotations. The conventional two-node Hermitian displacement functions (Bathe and Bolourchi [22]) are employed to represent the element in convected (co-rotated) coordinates. The element combines Euler-Bernoulli beam solutions with constant transverse shear strains along the length, by adding two generalized degrees-of-freedom to conventional axial, bending and torsional ones. Interface binding conditions, which have been considered in previous 2-D model [19], are also included in the 3-D element model formulation, and are dealt in the formulation in a unique and novel fashion, allowing the element to represent the behavior of multilayered risers and pipelines in both non-linear static and dynamic analyses. The additional shear degrees-of-freedom are statically condensed throughout the solution procedure and few demonstrative solutions are presented and compared to other independently obtained numerical results to demonstrate the element numerical capabilities.

2. Multilayered Pipe Beam Element

Studies for the beam element with co-rotational formulation have been the subject of various publications [20, 21], and may be regarded as an instance of the classical updated Lagrangian formulation [22]. It refers to a straight spatial reference configuration, defined by the updated coordinates of the element two nodal points, using a Hermitian formulation. Variations of this formulation are also available in the literature (Bathe and Bolourchi [22], Crisfield [21] and Mourelle [20]), but the formulation presented here is based on the following model assumptions:

- The element is subjected to large displacements and rotations, but restricted to small strains and small slip condition between layers;
- Initially plane, element layer cross sections remain plane and non-deformed in and out of its plane after element deformation, but not necessarily perpendicular to the beam longitudinal axis (Timoshenko hypothesis);
- Under torsion, cross sections remain plane without warping;
- All element layers share the same transverse displacements at element nodes i.e., no separation between layers is allowed.

In the element formulation, all variables are referred to a co-rotational configuration obtained from geometric transformations, including rigid body translations and rotations, from an initial non-deformed configuration. These variables can be identified from three distinct configurations, illustrated in Figure 1, and described as follows:

- 1) Initial Configuration (C_{ini}): represented by the element in its undeformed configuration, at spatial time $t=0$;

- 2) Reference Configuration (C_{ref}): represented by the configuration in which the element has been subjected, from its initial position, to rigid body motions only, under no straining;
- 3) Deformed Configuration (C_{def}): represented by the element in its current configuration at time t , after moving with rigid body motions and deformations due to applied external loads.

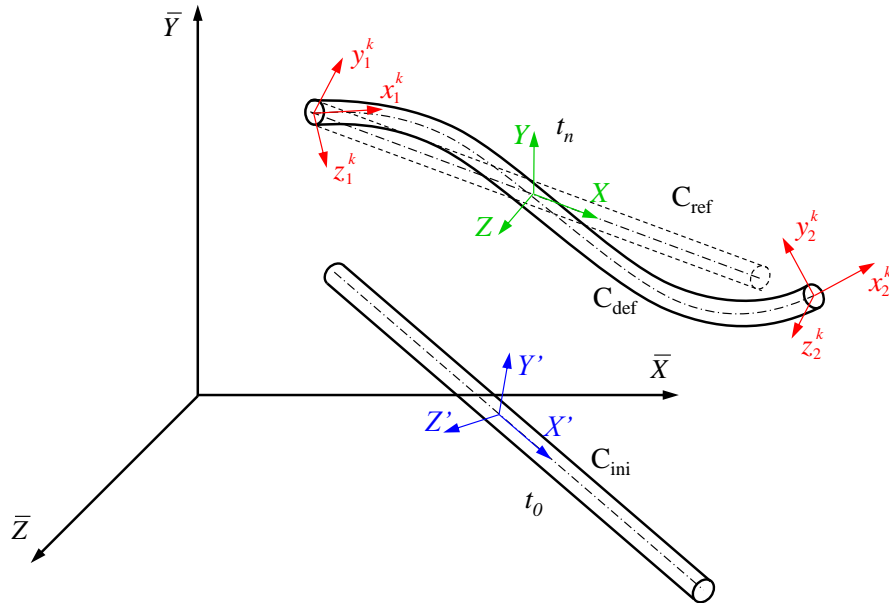


Figure 1: Beam Element Reference Configurations.

Reference systems attached to the beam element at each configuration are shown in Figure 1 and are described as follows:

- The Global Coordinate System ($\bar{X} \bar{Y} \bar{Z}$): is a spatial coordinate system whereby the structure is referred to. This system remains fixed during the entire beam analysis;
- The Initial Local Element Coordinate System ($X' Y' Z'$): is a coordinate system associated to the element at its initial undeformed configuration (C_{ini}). At this configuration, the element is assumed straight with the X' -axis coinciding with the element longitudinal direction and the other two Y' and Z' axes along the cross section principal directions of inertia;
- The Local Element Coordinate System ($X Y Z$): is associated to the Reference Configuration (C_{ref}), which is the Initial Local Element System

subjected to rigid body motion. The X -axis lies on the straight line defined by the two element nodes at updated position. The formulation of the co-rotational element is developed based on this reference system;

- The Element Layer Nodal Coordinate Systems (x_i^k, y_i^k, z_i^k) : are the coordinate systems associated to each node (i), for each layer (k), in the co-rotational formulation. The nodal systems of each layer are fixed to the element nodes, following its movements (translation and rotation).

2.1.

Basic Formulation for Large Rotations

When dealing with a reference vector of transformations in 3-D, an orthogonal spatial transformation $\mathbf{R}(\theta)$ should be considered

$$\mathbf{v}_1 = \mathbf{R}(\theta)\mathbf{v}_0 \quad (1)$$

which is represented in terms of only three independent parameters, as shown by Pacoste and Eriksson [26]. This approach results from the use of a pseudo-vector of rotation, defined as $\boldsymbol{\theta} = \theta \hat{\mathbf{i}}$, which geometrically represents a unique rotation, with an angle θ , about a fixed axis defined by the unit vector $\hat{\mathbf{i}}$.

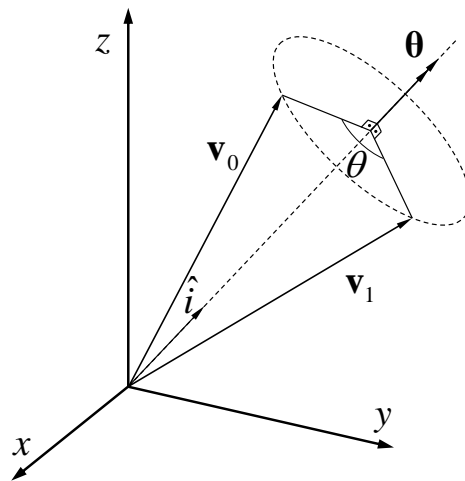


Figure 2: Spatial Transformation Between Two Vectors.

In this case, considering the magnitude of the rotation angle $\theta = \sqrt{\theta_x^2 + \theta_y^2 + \theta_z^2}$, the orthogonal rotation matrix (Rodrigues) can be expressed by

$$\mathbf{R} = \mathbf{I} + \frac{\sin \theta}{\theta} \mathbf{S}(\boldsymbol{\theta}) + \frac{1 - \cos \theta}{\theta^2} \mathbf{S}(\boldsymbol{\theta})\mathbf{S}(\boldsymbol{\theta}) \quad (2)$$

where \mathbf{I} is the 3×3 identity matrix and $\mathbf{S}(\boldsymbol{\theta})$ and $\boldsymbol{\theta}$ are a skew-symmetric matrix and the rotation pseudo-vector, respectively, both defined as function of components θ_x , θ_y and θ_z , as follows

$$\mathbf{S}(\boldsymbol{\theta}) = \begin{bmatrix} 0 & -\theta_z & \theta_y \\ \theta_z & 0 & -\theta_x \\ -\theta_y & \theta_x & 0 \end{bmatrix}, \quad \boldsymbol{\theta} = \begin{bmatrix} \theta_x \\ \theta_y \\ \theta_z \end{bmatrix} = \theta \hat{\mathbf{i}} \quad (3)$$

In the co-rotational formulation used in this work, matrix \mathbf{R} as defined in Eq. (2) is used to update the element reference configuration as well as the nodal point reference systems.

2.2.

Kinematics of Deformation

Incremental and iterative analysis is considered in the formulation with all element reference systems (see Figure 1) being updated after each iteration. In this way, two neighboring configurations of a pipe beam segment with multiple layers, in two successive configurations, at instants t and $t + \Delta t$, are shown in Figure 3,

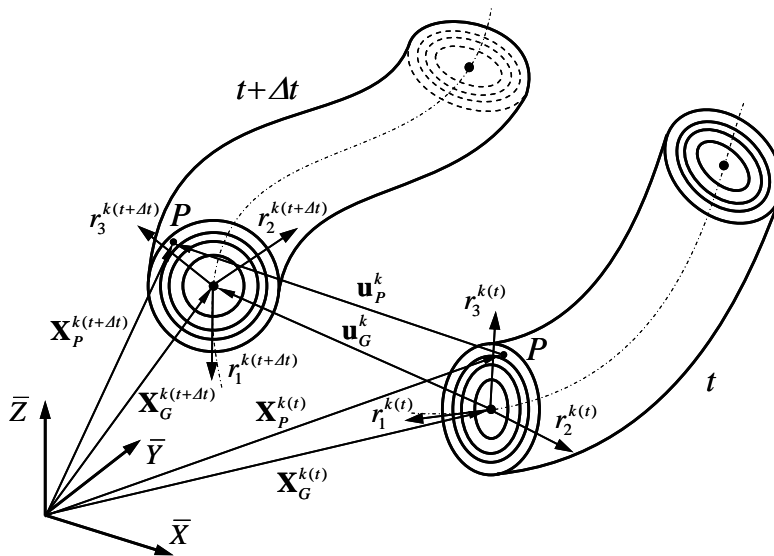


Figure 3: Multilayer Element in Two Successive Configurations.

where Δt is the time increment, $\mathbf{X}_P^{k(t)}$ and $\mathbf{X}_P^{k(t+\Delta t)}$ are the position vectors of a point P in layer- k cross section at instants t and $t + \Delta t$, respectively; $\mathbf{X}_G^{k(t)}$ and $\mathbf{X}_G^{k(t+\Delta t)}$ are layer- k geometric center position vectors at instants t and $t + \Delta t$, respectively; point P position in both configurations is expressed in terms of the coordinates (x, y, z) at the local reference system r^k and the geometric center position vector (\mathbf{X}_G^k) , i.e.:

$$\begin{cases} \mathbf{X}_P^{k(t)} = \mathbf{X}_G^{k(t)} + y\hat{\mathbf{r}}_2^{k(t)} + z\hat{\mathbf{r}}_3^{k(t)} \\ \mathbf{X}_P^{k(t+\Delta t)} = \mathbf{X}_G^{k(t+\Delta t)} + y\hat{\mathbf{r}}_2^{k(t+\Delta t)} + z\hat{\mathbf{r}}_3^{k(t+\Delta t)} \end{cases} \quad (4)$$

The incremental displacement vector at point P is then obtained:

$$\mathbf{u}_P^k = \begin{bmatrix} u_P^k \\ v_P^k \\ w_P^k \end{bmatrix} = \mathbf{X}_P^{k(t+\Delta t)} - \mathbf{X}_P^{k(t)} = \mathbf{u}_G^k + y(\hat{\mathbf{r}}_2^{k(t+\Delta t)} - \hat{\mathbf{r}}_2^{k(t)}) + z(\hat{\mathbf{r}}_3^{k(t+\Delta t)} - \hat{\mathbf{r}}_3^{k(t)}) \quad (5)$$

where

$$\mathbf{u}_G^k = \mathbf{X}_G^{k(t+\Delta t)} - \mathbf{X}_G^{k(t)} = \begin{bmatrix} u^k \\ v \\ w \end{bmatrix} \quad (6)$$

is the k -th layer geometric center incremental displacement vector.

Transformations between the local reference system vectors r_i^k ($i = 2, 3$) at time t and at time $t + \Delta t$ are obtained from incremental rotations $(\theta_x, \theta_y, \theta_z)$. This transformation is obtained by using a suitable rotation matrix $\mathbf{R}(\theta_x, \theta_y, \theta_z)$,

$$\hat{\mathbf{r}}_i^{k(t+\Delta t)} = \mathbf{R} \hat{\mathbf{r}}_i^{k(t)} \quad (i = 2, 3) \quad (7)$$

Substituting Eq. (7) into Eq. (5), one obtains point P incremental displacements as

$$\mathbf{u}_P^k = \mathbf{u}_G^k + y(\mathbf{R} - \mathbf{I})\hat{\mathbf{r}}_2^{k(t)} + z(\mathbf{R} - \mathbf{I})\hat{\mathbf{r}}_3^{k(t)} \quad (8)$$

An approximation for the rotation matrix presented in Eq. (2) is obtained by series expansion of the trigonometric terms

$$\begin{aligned}\sin \theta &= \sum_{n=0}^{\infty} (-1)^n \frac{\theta^{2n+1}}{(2n+1)!} = \theta - \frac{\theta^3}{3!} + \frac{\theta^5}{5!} - \frac{\theta^7}{7!} + \dots \\ \cos \theta &= \sum_{n=0}^{\infty} (-1)^n \frac{\theta^{2n}}{(2n)!} = 1 - \frac{\theta^2}{2!} + \frac{\theta^4}{4!} - \frac{\theta^6}{6!} + \dots\end{aligned}\quad (9)$$

and, considering terms up to second order only, the Rodrigues formula results in the following rotation matrix:

$$\mathbf{R} = \begin{bmatrix} 1 - \frac{\theta_y^2 + \theta_z^2}{2} & -\theta_z + \frac{\theta_x \theta_y}{2} & \theta_y + \frac{\theta_x \theta_z}{2} \\ \theta_z + \frac{\theta_x \theta_y}{2} & 1 - \frac{\theta_x^2 + \theta_z^2}{2} & -\theta_x + \frac{\theta_y \theta_z}{2} \\ -\theta_y + \frac{\theta_x \theta_z}{2} & \theta_x + \frac{\theta_y \theta_z}{2} & 1 - \frac{\theta_x^2 + \theta_y^2}{2} \end{bmatrix}\quad (10)$$

Thus, substituting this second order approximation for the rotation matrix into Eq. (8), the displacement vector components of a point P , in a given layer “ k ”, is obtained as a function of the displacements and rotations of the beam cross-section, referred to the local reference system r^k , in the form:

$$\begin{aligned}u_P^k &= u^k - y\theta_z^k + z\theta_y^k + y \frac{\theta_x^k \theta_y^k}{2} + z \frac{\theta_x^k \theta_z^k}{2} \\ v_P^k &= v - z\theta_x^k - y \frac{\theta_x^k + \theta_z^k}{2} + z \frac{\theta_y^k \theta_z^k}{2} \\ w_P^k &= \underbrace{w + y\theta_x^k}_{\text{Linear}} + \underbrace{y \frac{\theta_y^k \theta_z^k}{2} - z \frac{\theta_x^k + \theta_y^k}{2}}_{\text{Nonlinear}}\end{aligned}\quad (11)$$

where: u_P^k , v_P^k and w_P^k are the displacements of point P , in the local reference system r^k of layer- k ; u^k , θ_x^k , θ_y^k and θ_z^k are the axial displacements and rotations measured at the geometric center of each layer- k ; v and w are the transverse displacements (assumed equal for all layers); and y and z are the local coordinates of point P , defined within layer- k thickness ($r_i^k \leq \sqrt{y^2 + z^2} \leq r_o^k$), with r_i^k and r_o^k being the inner and outer radius, respectively.

The Green-Lagrange strain tensor components, used in the evaluation of the element strain energy, with the Principle of Virtual Work (PVW) [24], is obtained from the displacements at a point P of any layer cross section as

$$\begin{aligned}\varepsilon_{xx} &= \frac{\partial u_P}{\partial x} + \frac{1}{2} \left(\frac{\partial u_P}{\partial x} \right)^2 + \frac{1}{2} \left(\frac{\partial v_P}{\partial x} \right)^2 + \frac{1}{2} \left(\frac{\partial w_P}{\partial x} \right)^2 \\ \gamma_{xy} &= \frac{\partial u_P}{\partial y} + \frac{\partial v_P}{\partial x} + \frac{\partial u_P}{\partial x} \frac{\partial v_P}{\partial y} + \frac{\partial v_P}{\partial x} \frac{\partial v_P}{\partial y} + \frac{\partial w_P}{\partial x} \frac{\partial w_P}{\partial y} \\ \gamma_{xz} &= \underbrace{\frac{\partial u_P}{\partial z} + \frac{\partial w_P}{\partial x}}_{\text{Linear}(e_{ij})} + \underbrace{\frac{\partial u_P}{\partial x} \frac{\partial v_P}{\partial z} + \frac{\partial v_P}{\partial x} \frac{\partial v_P}{\partial z} + \frac{\partial w_P}{\partial x} \frac{\partial w_P}{\partial z}}_{\text{Nonlinear}(\eta_{ij})}\end{aligned}\quad (12)$$

2.3.

Finite Element Formulation

The multilayered element formulation is obtained considering the strain contribution of each layer - associated to linear and nonlinear strain terms - and straining at each interface material between layers. Considering the equilibrium of one single element layer at time $(t + \Delta t)$, the PVW for the updated Lagrangian formulation, gives [24]:

$$\int_V S_{ij}^{t+\Delta t} \delta \varepsilon_{ij}^{t+\Delta t} dV = \mathfrak{R}^{t+\Delta t} \quad (13)$$

where $S_{ij}^{t+\Delta t}$ is the second Piola-Kirchoff stress tensor [25]; $\varepsilon_{ij}^{t+\Delta t}$ is the Green-Lagrange strain tensor [25]; and $\mathfrak{R}^{t+\Delta t}$ is the virtual work due to external loading (body, surface, inertia and damping forces), given by:

$$\mathfrak{R}^{t+\Delta t} = \sum_i \left(\int_V f_i^{B(t+\Delta t)} \delta u_i dV + \int_S f_i^{S(t+\Delta t)} \delta u_i dS - \int_V \rho \ddot{u}_i \delta u_i dV + \int_V \kappa \dot{u}_i \delta u_i dV \right) \quad (14)$$

with $f_i^{B(t+\Delta t)}$ and $f_i^{S(t+\Delta t)}$ being body and surface force components, respectively; ρ and κ are material mass density and damping property parameter, respectively; \ddot{u}_i and \dot{u}_i are the acceleration and velocity vector components, respectively; and δu_i are the virtual displacement vector components.

Variables in Eq. (13) are accounted from the configuration C_{ref} shown in Figure 1. The linearized incremental equation requires small displacement increments, which allows the second Piola-Kirchoff and the Green-Lagrange tensors components to be written in incremental form as

$$\begin{aligned} S_{ij}^{t+\Delta t} &= \tau_{ij}^t + \Delta \tau_{ij} \\ \varepsilon_{ij}^{t+\Delta t} &= \varepsilon_{ij}^t + \Delta \varepsilon_{ij} \end{aligned} \quad (15)$$

where τ_{ij}^t are known Cauchy stress tensor components; $\Delta \tau_{ij}$ are the incremental stress components; ε_{ij}^t are known Cauchy-Green strain tensor components; and $\Delta \varepsilon_{ij}$ are the incremental strains, which are obtained from Eq. (12) by using the incremental displacements. Thus, Eq. (13) can be rewritten as follows:

$$\int_V (\tau_{ij}^t + \Delta\tau_{ij}) \delta(\varepsilon_{ij}^t + \Delta\varepsilon_{ij}) dV = \mathfrak{R}^{t+\Delta t} \quad (16)$$

In the reference configuration the element is subjected to rigid body motions only, i.e., there is no deformation, so $\delta\varepsilon_{ij}^t = 0$. Thus, Eq. (16) becomes

$$\int_V \Delta\tau_{ij} \delta\Delta\varepsilon_{ij} dV + \int_V \tau_{ij}^t \delta\Delta\varepsilon_{ij} dV = \mathfrak{R}^{t+\Delta t} \quad (17)$$

The incremental stresses ($\Delta\tau_{ij}$) are obtained from the incremental strains ($\Delta\varepsilon_{ij}$) by using a suitable constitutive relation:

$$\Delta\tau_{ij} = C_{ijkl} \Delta\varepsilon_{kl} \quad (18)$$

where C_{ijkl} is the material constitutive tensor.

As shown in Eq. (12), the incremental strains have linear (Δe_{ij}) and nonlinear ($\Delta\eta_{ij}$) components, i.e.:

$$\Delta\varepsilon_{ij} = \Delta e_{ij} + \Delta\eta_{ij} \quad (19)$$

Assuming a linear approximation for the incremental stresses and strains, one obtains:

$$\Delta\tau_{ij} = C_{ijkl} \Delta e_{kl} \quad \text{and} \quad \delta\Delta\varepsilon_{ij} = \delta\Delta e_{ij} \quad (20)$$

Substituting Eqs. (19) and (20) into Eq. (17), one obtains the following linearized equation:

$$\underbrace{\int_V C_{ijkl} \Delta e_{kl} \delta\Delta e_{ij} dV}_{\text{Linear}} + \underbrace{\int_V \tau_{ij}^t \delta\Delta\eta_{ij} dV}_{\text{Nonlinear}} = \underbrace{\mathfrak{R}^{t+\Delta t}}_{\text{External Forces}} - \underbrace{\int_V \tau_{ij}^t \delta\Delta e_{ij} dV}_{\text{Internal Forces}} \quad (21)$$

In this equation, the left hand side leads to the linear and nonlinear stiffness matrices and the right hand side leads to the external and internal force vectors.

2.4.

Element Displacement Field Interpolation

For a given layer, displacements within the element are obtained from interpolated nodal displacements using Hermite polynomials, which represent straight beam linear solutions under constant normal, transverse shear and

torsional internal loadings, under Euler-Bernouli beam assumptions. Thus, the displacement field at layer- k is:

$$\begin{aligned}
 u^k &= \underbrace{\left(1 - \frac{\xi}{\ell}\right)u_1^k + \frac{\xi}{\ell}u_2^k}_{u_0^k} + \underbrace{\frac{6\phi_1}{\ell}y v_1 - \frac{6\phi_1}{\ell}y v_2}_{-\frac{d v_0}{d \xi} y} + \underbrace{\frac{6\phi_1}{\ell}z w_1 - \frac{6\phi_1}{\ell}z w_2}_{-\frac{d w_0}{d \xi} z} + \underbrace{\phi_2 z \theta_{y_1}^k - \phi_3 z \theta_{y_2}^k}_{\theta_z^k} + \\
 &\quad \underbrace{\left(-\phi_2 y \theta_{z_1}^k + \phi_3 y \theta_{z_2}^k\right)}_{-\theta_x^k y} + \underbrace{\left(1 - 6\phi_1\right)z \beta_1^k + \left(1 - 6\phi_1\right)y \beta_2^k}_{\beta_1^k \text{ and } \beta_2^k \text{ constants in } \xi} \\
 v^k &= \underbrace{\phi_4 v_1 + \phi_6 v_2}_{v_0} + \underbrace{\left(-\left(1 - \frac{\xi}{\ell}\right)z \theta_{x_1}^k - \frac{\xi}{\ell}z \theta_{x_2}^k\right)}_{-\theta_x^k z} + \underbrace{\phi_5 \ell \theta_{z_1}^k - \phi_1 \xi \theta_{z_2}^k}_{-\bar{v}^k} + \left(\xi - \phi_7 \ell\right) \beta_2^k \\
 w^k &= \underbrace{\phi_4 w_1 + \phi_6 w_2}_{w_0} + \underbrace{\left(1 - \frac{\xi}{\ell}\right)y \theta_{x_1}^k + \frac{\xi}{\ell}y \theta_{x_2}^k}_{\theta_x^k y} + \underbrace{\left(-\phi_5 \ell \theta_{y_1}^k + \phi_1 \xi \theta_{y_2}^k\right)}_{\bar{w}^k} + \left(\xi - \phi_7 \ell\right) \beta_1^k
 \end{aligned} \tag{22}$$

where u_0^k is the axial displacements of the element centerline at layer- k ; ℓ is the element length; ξ is the longitudinal coordinate along element ($0 < \xi < \ell$); v_0 and w_0 are transverse displacements at the element centerline; \bar{v}^k and \bar{w}^k are transverse displacements along the layer- k centerline due to the nodal rotations θ_z^k e θ_x^k , respectively; and β_1^k and β_2^k are shear strains at planes $(\xi - y)$ and $(\xi - z)$, respectively (assumed constant along element length); and ϕ_i are the standard Hermite polynomials defined as:

$$\begin{aligned}
 \phi_1(\xi) &= \xi / \ell - (\xi / \ell)^2 \\
 \phi_2(\xi) &= 1 - 4(\xi / \ell) + 3(\xi / \ell)^2 \\
 \phi_3(\xi) &= 2(\xi / \ell) - 3(\xi / \ell)^2 \\
 \phi_4(\xi) &= 1 - 3(\xi / \ell)^2 + 2(\xi / \ell)^3 \\
 \phi_5(\xi) &= \xi / \ell - 2(\xi / \ell)^2 + (\xi / \ell)^3 \\
 \phi_6(\xi) &= 3(\xi / \ell)^2 - 2(\xi / \ell)^3 \\
 \phi_7(\xi) &= \xi / \ell - 3(\xi / \ell)^2 + 2(\xi / \ell)^3
 \end{aligned} \tag{23}$$

Equations (22) can be extended to element coordinates at layer- k , in matrix form, as follows:

$$\begin{bmatrix} u^k(\xi, y, z) \\ v^k(\xi, y, z) \\ w^k(\xi, y, z) \end{bmatrix} = \mathbf{H}^k(\xi, y, z) \mathbf{u}^k \tag{24}$$

where: $u^k(\xi, y, z)$, $v^k(\xi, y, z)$ and $w^k(\xi, y, z)$ are the displacements at a point of local coordinates (ξ, y, z) , at the element layer- k . From Eq. (22), the element interpolation matrix $\mathbf{H}^k(\xi, y, z)$ results in:

$$\mathbf{H}^k(\xi, y, z) = \begin{bmatrix} 1 - \frac{\xi}{\ell} & \frac{6y}{\ell} \phi_1 & \frac{6z}{\ell} \phi_1 & 0 & z\phi_2 & -y\phi_2 & \frac{\xi}{\ell} \\ 0 & \phi_4 & 0 & -\left(1 - \frac{\xi}{\ell}\right)z & 0 & \ell\phi_5 & 0 \\ 0 & 0 & \phi_4 & \left(1 - \frac{\xi}{\ell}\right)y & -\ell\phi_5 & 0 & 0 \\ -\frac{6y}{\ell} \phi_1 & -\frac{6z}{\ell} \phi_1 & 0 & -z\phi_3 & y\phi_3 & (1-6\phi_1)z & (1-6\phi_1)y \\ \phi_6 & 0 & -\frac{\xi}{\ell}z & 0 & -\xi\phi_1 & 0 & (\xi - \ell\phi_1) \\ 0 & \phi_6 & \frac{\xi}{\ell}y & \xi\phi_1 & 0 & (\xi - \ell\phi_1) & 0 \end{bmatrix}_{3 \times 14} \quad (25)$$

and the incremental displacement vector

$$\mathbf{u}^k = [u_1^k \quad v_1^k \quad w_1^k \quad \theta_{x_1}^k \quad \theta_{y_1}^k \quad \theta_{z_1}^k \quad u_2^k \quad v_2^k \quad w_2^k \quad \theta_{x_2}^k \quad \theta_{y_2}^k \quad \theta_{z_2}^k \quad \beta_1^k \quad \beta_2^k]^T \quad (26)$$

associated to element layer- k (nodal translations and rotations).

Each linear strain component in Eq. (12), obtained from the displacements given by Eq. (22), are defined at any point of layer- k by:

$$e_{xx}^k = \frac{du^k}{d\xi} = \frac{du_0^k}{d\xi} - \frac{d^2v_0}{d\xi^2}y - \frac{d^2w_0}{d\xi^2}z + \frac{d\theta_y^k}{d\xi}z - \frac{d\theta_z^k}{d\xi}y - 6\frac{d\phi_1}{d\xi}\beta_1^kz - 6\frac{d\phi_1}{d\xi}\beta_2^ky \quad (27)$$

or

$$e_{xx}^k = -\frac{1}{\ell}u_1^k + \frac{6y}{\ell}\frac{d\phi_1}{d\xi}v_1 + \frac{6z}{\ell}\frac{d\phi_1}{d\xi}w_1 + z\frac{d\phi_2}{d\xi}\theta_{y_1}^k - y\frac{d\phi_2}{d\xi}\theta_{z_1}^k + \frac{1}{\ell}u_2^k - \frac{6y}{\ell}\frac{d\phi_1}{d\xi}v_2 - \frac{6z}{\ell}\frac{d\phi_1}{d\xi}w_2 \\ - z\frac{d\phi_3}{d\xi}\theta_{y_2}^k + y\frac{d\phi_3}{d\xi}\theta_{z_2}^k - 6z\frac{d\phi_1}{d\xi}\beta_1^k - 6y\frac{d\phi_1}{d\xi}\beta_2^k \quad (28)$$

Similarly, the shear linear strain components e_{xy}^k and e_{xz}^k are:

$$2e_{xy}^k = \frac{du^k}{dy} + \frac{dv}{d\xi} = \left(-\frac{dv_0}{d\xi} - \theta_{z_1}^k + (1-6\phi_1)\beta_2^k\right) + \left(\frac{dv_0}{d\xi} - \frac{d\theta_x^k}{d\xi}z - \frac{d\bar{v}^k}{d\xi} + \left(1 - \frac{d\phi_1}{d\xi}\ell\right)\beta_2^k\right) \quad (29)$$

or

$$2e_{xy}^k = \frac{z}{\ell}\theta_{x_1}^k + \left(\ell\frac{d\phi_5}{d\xi} - \phi_2\right)\theta_{z_1}^k - \frac{z}{\ell}\theta_{x_2}^k + \left(\phi_3 - \phi_1 - \frac{d\phi_1}{d\xi}\xi\right)\theta_{z_2}^k + \left(2 - 6\phi_1 - \frac{d\phi_1}{d\xi}\ell\right)\beta_2^k \quad (30)$$

and,

$$2e_{xz}^k = \frac{du^k}{dz} + \frac{dw}{d\xi} = \left(-\frac{dw_0}{d\xi} + \theta_{y_1}^k + (1-6\phi_1)\beta_1^k\right) + \left(\frac{dw_0}{d\xi} + \frac{d\theta_x^k}{d\xi}y + \frac{d\bar{w}^k}{d\xi} + \left(1 - \frac{d\phi_1}{d\xi}\ell\right)\beta_1^k\right) \quad (31)$$

or

$$2e_{xx}^k = -\frac{y}{\ell}\theta_{x_1}^k + \left(\phi_2 - \ell \frac{d\phi_5}{d\xi}\right)\theta_{y_1}^k + \frac{y}{\ell}\theta_{x_2}^k + \left(\phi_1 - \phi_3 + \xi \frac{d\phi_1}{d\xi}\right)\theta_{y_2}^k + \left(2 - 6\phi_1 - \ell \frac{d\phi_7}{d\xi}\right)\beta_1^k \quad (32)$$

Thus, from Equations (28), (30) e (32), linear strain components results in the following matrix form

$$\mathbf{e} = \begin{bmatrix} e_{xx}^k \\ 2e_{xy}^k \\ 2e_{xz}^k \end{bmatrix} = \mathbf{B}_L^k \mathbf{u}^k \quad \text{and} \quad \delta \mathbf{e} = \mathbf{B}_L^k \delta \mathbf{u}^k \quad (33)$$

where,

$$\mathbf{B}_L^k = \begin{bmatrix} -\frac{1}{\ell} & \frac{6y}{\ell} \frac{d\phi_1}{d\xi} & \frac{6z}{\ell} \frac{d\phi_1}{d\xi} & 0 & z \frac{d\phi_2}{d\xi} & -y \frac{d\phi_2}{d\xi} & \frac{1}{\ell} & -\frac{6y}{\ell} \frac{d\phi_1}{d\xi} & -\frac{6z}{\ell} \frac{d\phi_1}{d\xi} \\ 0 & 0 & 0 & \frac{z}{\ell} & 0 & \ell \frac{d\phi_5}{d\xi} - \phi_2 & 0 & 0 & 0 \\ 0 & 0 & 0 & -\frac{y}{\ell} & \phi_2 - \ell \frac{d\phi_5}{d\xi} & 0 & 0 & 0 & 0 \\ 0 & -z \frac{d\phi_3}{d\xi} & y \frac{d\phi_3}{d\xi} & -6z \frac{d\phi_1}{d\xi} & -6y \frac{d\phi_1}{d\xi} \\ -\frac{z}{\ell} & 0 & \phi_3 - \phi_1 - \xi \frac{d\phi_1}{d\xi} & 0 & 2 - 6\phi_1 - \ell \frac{d\phi_7}{d\xi} \\ \frac{y}{\ell} & \phi_1 - \phi_3 + \xi \frac{d\phi_1}{d\xi} & 0 & 2 - 6\phi_1 - \ell \frac{d\phi_7}{d\xi} & 0 \end{bmatrix}_{3 \times 14} \quad (34)$$

Similarly, for the nonlinear term in Eq. (21) the following matrix form is used:

$$\tau_{ij} \delta \Delta \eta_{ij} = \delta \mathbf{u}^{kT} \mathbf{B}_G^{kT} \boldsymbol{\tau} \mathbf{B}_G^k \mathbf{u}^k \quad (35)$$

where:

$$\mathbf{B}_G^k = \begin{bmatrix} -\frac{1}{\ell} & \frac{6y}{\ell} \frac{d\phi_1}{d\xi} & \frac{6z}{\ell} \frac{d\phi_1}{d\xi} & 0 & z \frac{d\phi_2}{d\xi} & -y \frac{d\phi_2}{d\xi} & \frac{1}{\ell} \\ 0 & \frac{d\phi_4}{d\xi} & 0 & \frac{z}{\ell} & 0 & \ell \frac{d\phi_5}{d\xi} & 0 \\ 0 & 0 & \frac{d\phi_4}{d\xi} & -\frac{y}{\ell} & -\ell \frac{d\phi_5}{d\xi} & 0 & 0 \\ 0 & \frac{6}{\ell} \phi_1 & 0 & 0 & 0 & -\phi_2 & 0 \\ 0 & 0 & 0 & 1 - \frac{\xi}{\ell} & 0 & 0 & 0 \\ 0 & 0 & \frac{6}{\ell} \phi_1 & 0 & \phi_2 & 0 & 0 \\ 0 & 0 & 0 & \frac{\xi}{\ell} - 1 & 0 & 0 & 0 \\ -\frac{6y}{\ell} \frac{d\phi_1}{d\xi} & -\frac{6z}{\ell} \frac{d\phi_1}{d\xi} & 0 & -z \frac{d\phi_2}{d\xi} & y \frac{d\phi_2}{d\xi} & -6z \frac{d\phi_1}{d\xi} & -6y \frac{d\phi_1}{d\xi} \\ \frac{d\phi_6}{d\xi} & 0 & -\frac{z}{\ell} & 0 & -\phi_1 - \xi \frac{d\phi_1}{d\xi} & 0 & 1 - \ell \frac{d\phi_7}{d\xi} \\ 0 & \frac{d\phi_6}{d\xi} & \frac{y}{\ell} & \phi_1 + \xi \frac{d\phi_1}{d\xi} & 0 & 1 - \ell \frac{d\phi_7}{d\xi} & 0 \\ -\frac{6}{\ell} \phi_1 & 0 & 0 & 0 & \phi_3 & 0 & 1 - 6\phi_1 \\ 0 & 0 & \frac{\xi}{\ell} & 0 & 0 & 0 & 0 \\ 0 & -\frac{6}{\ell} \phi_1 & 0 & -\phi_3 & 0 & 1 - 6\phi_1 & 0 \\ 0 & 0 & -\frac{\xi}{\ell} & 0 & 0 & 0 & 0 \end{bmatrix}_{7 \times 14} \quad (36)$$

with $y = r \cos \varphi$ and $z = r \sin \varphi$, and:

$$\boldsymbol{\tau}^k = \begin{bmatrix} \tau_{xx}^k & 0 & 0 & \tau_{xy}^k & 0 & \tau_{xz}^k & 0 \\ 0 & \tau_{xx}^k & 0 & 0 & 0 & 0 & \tau_{xz}^k \\ 0 & 0 & \tau_{xx}^k & 0 & \tau_{xy}^k & 0 & 0 \\ \tau_{xy}^k & 0 & 0 & 0 & 0 & 0 & 0 \\ 0 & 0 & \tau_{xy}^k & 0 & 0 & 0 & 0 \\ \tau_{xz}^k & 0 & 0 & 0 & 0 & 0 & 0 \\ 0 & \tau_{xz}^k & 0 & 0 & 0 & 0 & 0 \end{bmatrix}$$

Stress components, at each element layer- k , in local coordinates, are obtained from the beam internal forces, at the element nodes, as indicated below.

$$\begin{aligned} \tau_{xx}^k &= \frac{N^k}{A^k} + \frac{M_y^k}{I^k} z - \frac{M_x^k}{I^k} y \\ \tau_{xy}^k &= -\frac{M_x^k}{J^k} z + \frac{V_y^k}{A^k} \\ \tau_{xz}^k &= \frac{M_x^k}{J^k} y + \frac{V_z^k}{A^k} \end{aligned}, \text{ with: } \begin{aligned} N^k &= -F_1^k \\ V_y^k &= -F_2^k \\ V_z^k &= -F_3^k \\ M_x^k &= -F_4^k \\ M_y^k &= F_3^k \xi + F_5^k \\ M_z^k &= -F_2^k \xi + F_6^k \end{aligned} \quad (37)$$

where F_i^k are the layer- k vector of internal forces and moments components; A^k is the layer- k cross section area; I^k is the layer- k cross section moment of inertia with respect to the axis of symmetry; $J^k = 2I^k$ is the layer- k cross section polar moment of inertia with respect to the cross section geometric center; and ξ is the local coordinate along element length. Details on the derivations of the geometric compatibility matrix (\mathbf{B}_G^k) and the stress components matrix ($\boldsymbol{\tau}^k$) are presented in Bathe and Bolourchi [22].

2.5.

Element Layer Stiffness Matrices

For a given layer- k , the element linear stiffness matrix is obtained by substituting Eq. (33) in the first term of Eq. (21):

$$\mathbf{K}_L^k = \int_0^\ell \int_{r_i^k}^{r_o^k} \int_0^{2\pi} r \mathbf{B}_L^{kT} \mathbf{C}^k \mathbf{B}_L^k d\varphi dr d\xi \quad (38)$$

where \mathbf{B}_L is the linear compatibility matrix, as defined in Eq. (34), using $y = r \cos \varphi$ and $z = r \sin \varphi$, and

$$\mathbf{C}^k = \begin{bmatrix} E^k & 0 & 0 \\ 0 & G^k & 0 \\ 0 & 0 & G^k \end{bmatrix} \quad (39)$$

Layer- k geometric stiffness matrix contribution (\mathbf{K}_G^k) is obtained from Eq. (35) and the second term of Eq. (21) that results from

$$\mathbf{K}_G^k = \int_0^\ell \int_{r_i^k}^{r_o^k} \int_0^{2\pi} r \mathbf{B}_G^{kT} \boldsymbol{\tau}^k \mathbf{B}_G^k d\varphi dr d\xi \quad (40)$$

In Appendices B.1 and B.2, layer- k (\mathbf{K}_L^k) and (\mathbf{K}_G^k) matrices are presented explicitly.

2.6.

Element Layer Mass Matrix

The mass matrix associated to each element layer- k is obtained by substituting Eq. (24) into the inertia term of the external force work expression, given by Eq. (14), i.e.:

$$\int_{V^k} \rho^k \ddot{u}_i \delta u_i dV = \delta \mathbf{u} \left(\int_{V^k} \rho^k \mathbf{H}^{kT} \mathbf{H}^k dV \right) \ddot{\mathbf{u}}. \quad (41)$$

Thus,

$$\mathbf{M}^k = \int_0^\ell \int_{r_i^k}^{r_o^k} \int_0^{2\pi} r \rho^k \mathbf{H}^{kT} \mathbf{H}^k d\varphi dr d\xi \quad (42)$$

where \mathbf{M}^k is the mass matrix associated to the element layer- k ; \mathbf{H}^k is the interpolation matrix defined in Eq. (25) and ρ^k is the layer- k mass density. In Appendix B.3 layer- k mass matrix (\mathbf{M}^k) is presented in closed form.

2.7.

Element Layer Damping Matrix

The expression for the element layer damping matrix is obtained by substituting Eq. (24) in the damping term of the external forces work expression, given by Eq. (14), in the form:

$$\int_{V^k} \kappa^k \dot{u}_i \delta u_i dV = \delta u \left(\int_{V^k} \kappa^k \mathbf{H}^{kT} \mathbf{H}^k dV \right) \dot{\mathbf{u}} \quad (43)$$

Thus,

$$\mathbf{D}^k = \int_0^\ell \int_{r_i^k}^{r_o^k} \int_0^{2\pi} r \kappa^k \mathbf{H}^{kT} \mathbf{H}^k d\phi dr d\xi \quad (44)$$

where \mathbf{D}^k is the damping matrix for the element layer- k ; \mathbf{H}^k is the interpolation matrix defined in Eq. (25) and κ^k is the layer- k material damping parameter.

In practice the damping parameter (κ) is not readily available because damping properties are frequency dependent. For this reason, in this study matrix \mathbf{D}^k is not obtained from Eq. (44) and, the structure damping matrix is constructed from a linear combination of mass and stiffness matrices, as Rayleigh proportional damping [24]:

$$\mathbf{D}^k = \alpha \mathbf{M}^k + \beta \mathbf{K}^k \quad (45)$$

where α and β are constants to be determined from two given damping ratios corresponding to two vibration frequencies.

2.8.

Contact Conditions

In this section, model solutions for the interlayer contact used in the finite element formulation are derived. The longitudinal and torsional relative displacements between layers result in shear stresses at the interlayer material, as shown in Figure 4. In the model each interface is assumed to be under constant (through the thickness) shearing straining as its thickness (h) is very small when compared to other pipe cross section dimensions.

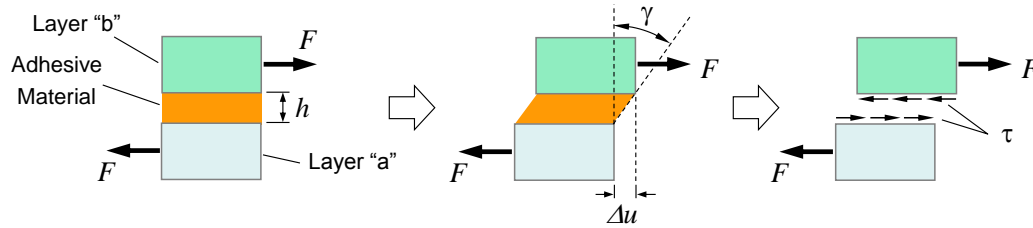


Figure 4: Details of Interface Straining In a Two-Layer Pipe Wall Segment.

Thus, shear strain and stress at interface are evaluated using the following linear approximation:

$$\gamma = \frac{\Delta u}{h} \text{ and } \tau = G\gamma = \frac{G}{h}\Delta u = k\bar{\gamma} \quad (46)$$

where G is the interface material shear modulus; $k = \frac{G}{h}$ is the overall contact stiffness; and $\bar{\gamma} = \Delta u$ is the interlayer relative displacement.

The idea here is to employ material constitutive relations that may represent the overall physical meaning of contact conditions at the interface material including certain damage conditions. These attempts are described as follows:

A. Linear Elastic Slip

In this case the interlayer material behaves according to the constitutive relation shown in Figure 5. Contact stress is proportional to the layers relative displacement. This is the constitutive relation used throughout derivations in Aguiar and Almeida [18] and is represented by the linear model solution where total strain energy in the adhesive is preserved after unloading.

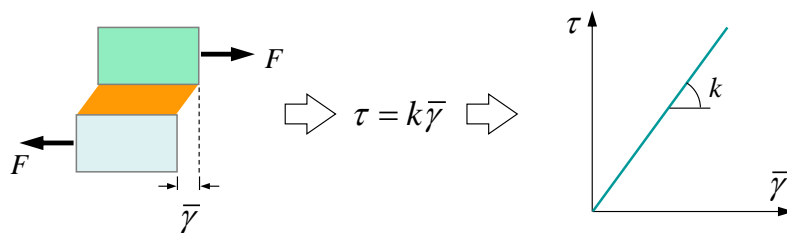


Figure 5: Linear Elastic Constitutive Relation - Slip Model Representation.

B. Slip With Static Friction

In this case rupture occurs when shear stress in adhesive material reaches a limit value τ_ℓ . Thereafter, contact condition between layers remains through friction (static) forces and the “material law” follows the bi-linear constitutive

relation shown in Figure 6. In a cycle loading process, total strain energy at interface material is not preserved.

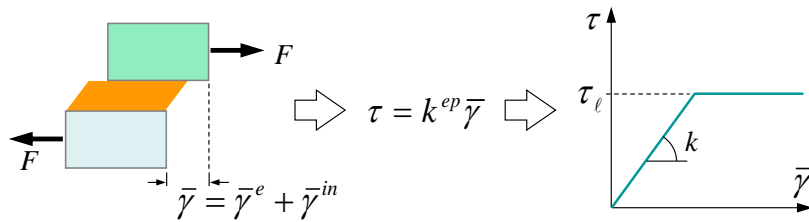


Figure 6: Layer contact with static friction.

where $\bar{\gamma}^e$ and $\bar{\gamma}^{in}$ are the elastic and inelastic terms of the relative displacement.

C. Slip With Kinetic Friction

In this case a multi-linear constitutive model is required to represent material rupture but with kinetic friction between layers. After reaching a limit value, shear stress drops to a lower value keeping it constant as in kinetic friction force fashion. Again, as in the previous case, total potential energy in the adhesive is partially preserved.

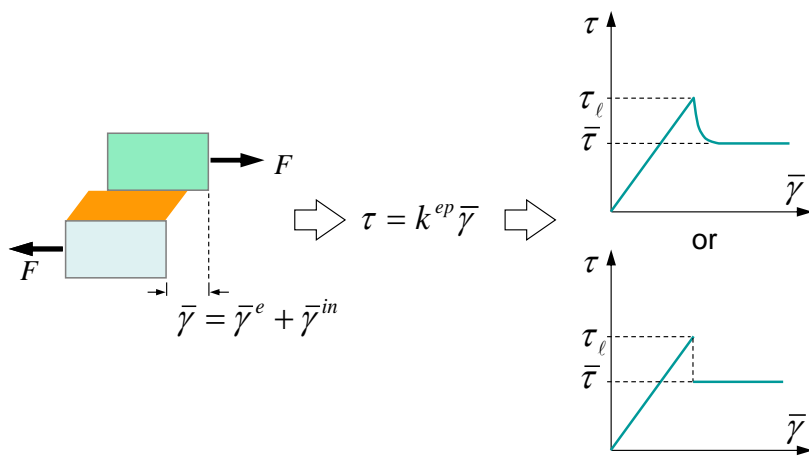


Figure 7: Layer Contact With Kinetic Friction.

D. Rupture

In this case, a multi-linear constitutive model is employed to represent material rupture with no friction between layers. Thus, after reaching a limit value, shear stress at interface vanishes. By this model, in a cycling loading process, the total strain energy stored during the interface linear behavior is completely lost.

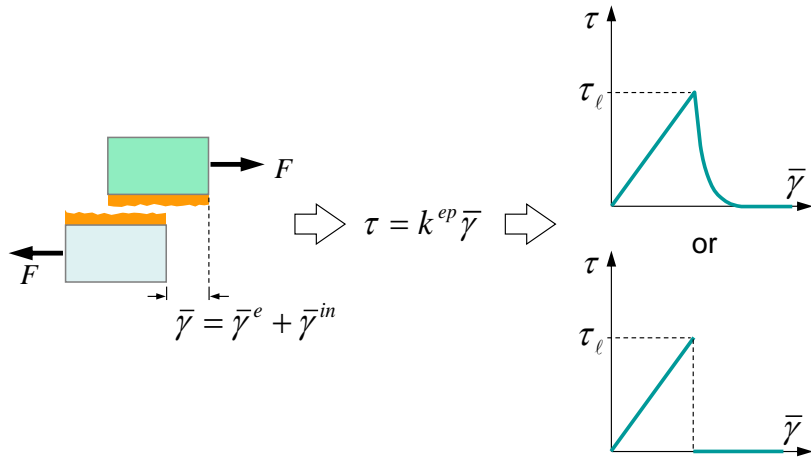


Figure 8: Rupture – Multi-Linear Elastic-Perfect Plastic Model.

2.9.

Interface Constitutive Model

In this section, the nonlinear constitutive relations shown in Figures 6 to 8 for the interface material, is presented in detail. For simplicity, the models presented above are one-dimensional. However, in a multi-layered pipe, the relative displacements can occur in the axial ($\bar{\gamma}_x$) as circumferential ($\bar{\gamma}_\varphi$) directions as shown in Figure 9.

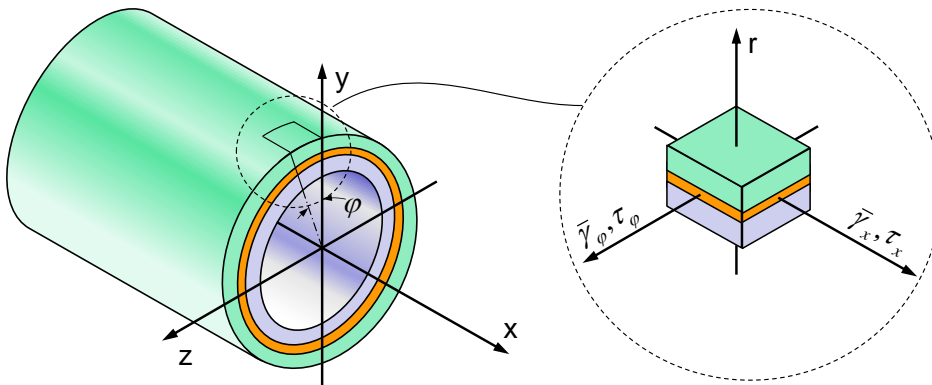


Figure 9: Directions for Relative Displacements.

For all contact conditions discussed, stress state at the interface material must remain within the following domain

$$\mathbf{D}_\tau = \{\boldsymbol{\tau} \in \mathbf{R} \mid f(\boldsymbol{\tau}, \alpha) \leq 0\} \tag{47}$$

where $f(\boldsymbol{\tau}, \alpha)$ is the associated yield-type function, expressed in terms of the contact stresses $\boldsymbol{\tau}$ and hardening parameter α , with:

$$\boldsymbol{\tau} = \begin{bmatrix} \tau_x & \tau_\phi \end{bmatrix}^T \quad (48)$$

The choice of an appropriate yield function defines the slip condition model. Table 1 presents the corresponding yield function used to represent each of the contact conditions studied in this work, as discussed in Section 2.8.

Table 1: Slip Model Conditions.

| Slip Model | Yielding Function | $H(\alpha)$ |
|--|--|--------------------------------|
| A. Linear Elastic Slip | not applicable | - |
| B. Slip in Static Friction (bi-linear) | $f(\boldsymbol{\tau}) = \boldsymbol{\tau} - \tau_\ell$ | 0 |
| C. Slip in Kinetic Friction (multi-linear) | $f(\boldsymbol{\tau}, \alpha) = \boldsymbol{\tau} - \tau_\ell(\alpha)$ | according to the hardening law |
| D. Rupture (multi-linear) | | |

where $|\boldsymbol{\tau}| = \sqrt{\tau_x^2 + \tau_\phi^2}$; with τ_x and τ_ϕ being the contact stresses in the axial and circumferential directions as shown in Figure 9; τ_ℓ is the limit contact stress; and $H(\alpha) = df/d\alpha$ is the hardening modulus.

According to Simo and Hughes [31], the nonlinear slip model can be characterized by means of the following set of equations

$$\begin{aligned} \bar{\boldsymbol{\gamma}} &= \bar{\boldsymbol{\gamma}}^e + \bar{\boldsymbol{\gamma}}^{in} \\ \boldsymbol{\tau} &= k\bar{\boldsymbol{\gamma}}^e = k(\bar{\boldsymbol{\gamma}} - \bar{\boldsymbol{\gamma}}^{in}) \\ d\bar{\boldsymbol{\gamma}}^{in} &= \lambda \mathbf{r} = \lambda \frac{d\mathbf{f}}{d\boldsymbol{\tau}} \\ d\alpha &= \lambda \end{aligned} \quad (49)$$

where $\bar{\boldsymbol{\gamma}}$, $\bar{\boldsymbol{\gamma}}^e$ and $\bar{\boldsymbol{\gamma}}^{in}$ are the vectors of total, elastic and inelastic slip measures obtained from relative longitudinal and circumferential relative displacements between layers; $\boldsymbol{\tau}$ is the vector of contact stresses; k is the elastic contact stiffness parameter; α is the hardening parameter; λ is the inelastic slip modulus increment to be determined; and \mathbf{r} a unit vector that indicates the “yield” direction given by:

$$\mathbf{r} = \frac{1}{|\boldsymbol{\tau}|} \begin{bmatrix} \tau_x \\ \tau_\phi \end{bmatrix} \quad (50)$$

Thus, the associated mathematical problem consists in: given $\{\bar{\boldsymbol{\gamma}}_n, \bar{\boldsymbol{\gamma}}_n^{in}, \boldsymbol{\tau}_n, \alpha_n\}$ and $\bar{\boldsymbol{\gamma}}_{n+1}$ as a known solution state and new relative displacements, respectively,

obtain $\bar{\gamma}_{n+1}^p$, α_{n+1} and τ_{n+1} . This problem is solved in two steps. First, an elastic increment is assumed to obtain the following trial state

$$\begin{aligned}\tau_{n+1}^* &= k(\bar{\gamma}_{n+1} - \bar{\gamma}_n^{in}) \equiv \tau_n + k\Delta\bar{\gamma}_n \\ \bar{\gamma}_{n+1}^{in*} &= \bar{\gamma}_n^{in} \\ \alpha_{n+1}^* &= \alpha_n \\ f_{n+1}^* &= |\tau_{n+1}^*| - \tau_{\ell n}\end{aligned}\quad (51)$$

From the trial state, it is possible to determine if the slip increment is elastic or inelastic according to the criterion

$$f_{n+1}^* \begin{cases} \leq 0 \rightarrow \text{elastic increment} : \lambda = 0 \\ > 0 \rightarrow \text{inelastic increment} : \lambda > 0 \end{cases} \quad (52)$$

Assuming an inelastic increment, one obtains the stress τ_{n+1} in terms of the trial stress τ_{n+1}^* and the inelastic slip modulus λ as:

$$\begin{aligned}\tau_{n+1} &= k(\bar{\gamma}_{n+1} - \bar{\gamma}_{n+1}^{in}) \\ &= k(\bar{\gamma}_{n+1} - \bar{\gamma}_n^{in}) - k(\bar{\gamma}_{n+1}^{in} - \bar{\gamma}_n^{in}) \\ &= \tau_{n+1}^* - k\lambda\mathbf{r}_{n+1}\end{aligned}\quad (53)$$

Therefore, since $\lambda > 0$, the actual state is written as

$$\begin{aligned}\tau_{n+1} &= \tau_{n+1}^* - k\lambda\mathbf{r}_{n+1} \\ \bar{\gamma}_{n+1}^{in} &= \bar{\gamma}_n^{in} + \lambda\mathbf{r}_{n+1} \\ \alpha_{n+1} &= \alpha_n + \lambda \\ f_{n+1} &= |\tau_{n+1}| - \tau_{\ell n+1} = 0\end{aligned}\quad (54)$$

Now the above problem is solved explicitly in terms of the trial elastic state by the following procedure:

$$|\tau_{n+1}| \mathbf{r}_{n+1} = |\tau_{n+1}^*| \mathbf{r}_{n+1}^* - k\lambda\mathbf{r}_{n+1} \quad (55)$$

Collecting terms in Eq. (55), one obtains

$$[|\tau_{n+1}| + k\lambda] \mathbf{r}_{n+1} = |\tau_{n+1}^*| \mathbf{r}_{n+1}^* \quad (56)$$

As $\lambda > 0$ and $k > 0$, the term within brackets in Eq. (56) is necessarily positive. Therefore it is required that

$$\mathbf{r}_{n+1} = \mathbf{r}_{n+1}^* \quad (57)$$

along with the condition

$$|\boldsymbol{\tau}_{n+1}| + k\lambda = |\boldsymbol{\tau}_{n+1}^*|. \quad (58)$$

From Eqs. (54) and (58), the yield criterion f_{n+1} is written as

$$f_{n+1} = |\boldsymbol{\tau}_{n+1}^*| - k\lambda - \tau_\ell(\alpha_n + \lambda) = 0. \quad (59)$$

Depending on the hardening law $\tau_\ell(\alpha_n + \lambda)$, Eq. (59) can be nonlinear and must be solved numerically for λ . The inelastic constitutive relation is then obtained from the consistency condition ($\lambda df = 0$), as described in Simo and Hughes [31]. If $\lambda > 0$, then

$$df(\boldsymbol{\tau}, \alpha) = \frac{df}{d\boldsymbol{\tau}} d\boldsymbol{\tau} + \frac{df}{d\alpha} d\alpha = 0 \quad (60)$$

Substituting values for $df/d\boldsymbol{\tau}$, $df/d\alpha$, $d\boldsymbol{\tau}$ and $d\alpha$, one obtains

$$\mathbf{r}^T k(d\bar{\boldsymbol{\gamma}} - \lambda \mathbf{r}) - \lambda H = 0 \quad (61)$$

where $H = df/d\alpha$ is set for each hardening law, as shown in Table 1.

Solving Eq. (61) for λ , one obtains

$$\lambda = \frac{k\mathbf{r}}{k+H} d\bar{\boldsymbol{\gamma}} \quad (62)$$

that substituted into Eq. (49), leads to the contact stress increment

$$d\boldsymbol{\tau} = \frac{kH}{k+H} d\bar{\boldsymbol{\gamma}} \quad (63)$$

Therefore,

$$d\boldsymbol{\tau} = k^{ep} d\bar{\boldsymbol{\gamma}} \quad (64)$$

where

$$k^{ep} = \begin{cases} k & \text{if } \lambda = 0 \\ \frac{kH}{k+H} & \text{if } \lambda > 0 \end{cases} \quad (65)$$

2.10.

Interface Stiffness Matrix

At the interface, adhesive material is assumed under constant pure shear deformation, throughout the cross-section thickness. Interface contribution to the element stiffness matrix is obtained by considering the strain energy associated to the interface material, due to adjoining layers relative displacements ($\bar{\gamma}_i$ denotes equivalent shear strains). These are due to axial and torsional displacements between layers (say layers k and $k+1$) and an equivalent strain vector is defined with two components:

$$\bar{\gamma}_i^k = \begin{bmatrix} \bar{\gamma}_x^k & \bar{\gamma}_\varphi^k \end{bmatrix}^T \quad (66)$$

with

$$\begin{aligned} \bar{\gamma}_x^k(\varphi) &= (u^{k+1}(\varphi) - u^k(\varphi)) \\ \bar{\gamma}_\varphi^k &= r(\theta_x^{k+1} - \theta_x^k) \end{aligned} \quad (67)$$

where $u^k(\varphi)$ and θ_x^k are the longitudinal displacement and torsional rotation of layer- k cross section, respectively; and φ is the angular coordinate at the interface cross section, as shown in Figure 10.

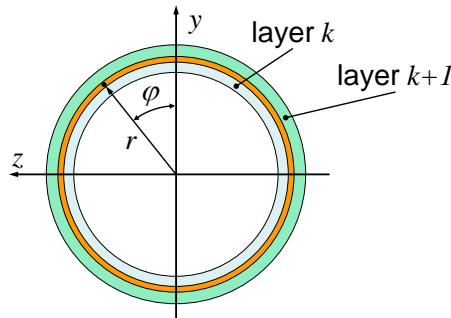


Figure 10: Angular Coordinate φ at the Interface.

For a linearly elastic model, the constitutive relation at the interface material above layer- k results in

$$\boldsymbol{\tau}_i^k = \begin{bmatrix} \tau_x^k \\ \tau_\varphi^k \end{bmatrix} = \begin{bmatrix} k_c^k & 0 \\ 0 & k_c^k \end{bmatrix} \begin{bmatrix} \bar{\gamma}_x^k \\ \bar{\gamma}_\varphi^k \end{bmatrix} = k_c^k \mathbf{I} \begin{bmatrix} \bar{\gamma}_x^k \\ \bar{\gamma}_\varphi^k \end{bmatrix} \quad (68)$$

where k_c^k is associated to contact stiffness between layers k and $k+1$; and τ_x^k and τ_ϕ^k are contact stress components along the longitudinal and circumferential directions, respectively.

Slip condition between layers is modeled by imposing a limit value on the shear stress (τ_i) at the interface material, as described in section 2.8. This is obtained by using a suitable constitutive model, according to one of the yield-type functions presented in Table 1, in section 2.9. Thus, the constitutive relation for interface k results in

$$\boldsymbol{\tau}_i^k = k_c^{ep} \mathbf{I} \bar{\boldsymbol{\gamma}}_i^k \quad (69)$$

where $\boldsymbol{\tau}_i^k$ and $\bar{\boldsymbol{\gamma}}_i^k$ are as in Eqs. (68) and (66), respectively; and the nonlinear slip modulus (k_c^{ep}) is obtained from Eq. (65).

Thus, considering the strain energy due to shearing at the interface material, one obtains

$$\pi_{\tau_i}^k = \frac{1}{2} \int_S \boldsymbol{\tau}_i^{kT} \bar{\boldsymbol{\gamma}}_i^k dS \quad (70)$$

Substitution of the expressions for $\boldsymbol{\tau}_i^k$ and $\bar{\boldsymbol{\gamma}}_i^k$ leads to

$$\pi_{\tau_i}^k = \frac{1}{2} \int_0^\ell \int_0^{2\pi} k_c^{ep} r \left((u^{k+1} - u^k)^2 + r^2 (\theta_x^{k+1} - \theta_x^k)^2 \right) d\phi d\xi \quad (71)$$

The variation of the interface strain energy is:

$$\delta\pi_{\tau_i}^k = \int_0^\ell \int_0^{2\pi} k_c^{ep} r \left((u^{k+1} - u^k) \delta(u^{k+1} - u^k) + r^2 (\theta_x^{k+1} - \theta_x^k) \delta(\theta_x^{k+1} - \theta_x^k) \right) d\phi d\xi, \quad (72)$$

which can be rewritten in the following compact matrix form

$$\delta\pi_{\tau_i}^k = \delta\mathbf{u} \left(\int_0^\ell \int_0^{2\pi} r \mathbf{B}_i^{kT} k_c^{ep} \mathbf{B}_i^k d\phi d\xi \right) \mathbf{u} \quad (73)$$

The stiffness matrix associated to each interface material between layers is

$$\mathbf{K}_i^k = \int_0^\ell \int_0^{2\pi} r \mathbf{B}_i^{kT} k_c^{ep} \mathbf{B}_i^k d\phi d\xi \quad (74)$$

with

$$\mathbf{B}_i^k = \begin{bmatrix} \frac{\xi}{\ell} - 1 & 0 & -z\phi_2 & y\phi_2 & -\frac{\xi}{\ell} & 0 & z\phi_3 & -y\phi_3 \\ 0 & r\left(\frac{\xi}{\ell} - 1\right) & 0 & 0 & 0 & -r\frac{\xi}{\ell} & 0 & 0 \\ \\ 1 - \frac{\xi}{\ell} & 0 & z\phi_2 & -y\phi_2 & \frac{\xi}{\ell} & 0 & -z\phi_3 & y\phi_3 \\ 0 & r\left(1 - \frac{\xi}{\ell}\right) & 0 & 0 & 0 & r\frac{\xi}{\ell} & 0 & 0 \\ \\ (6\phi_1 - 1)z & (6\phi_1 - 1)y & (1 - 6\phi_1)z & (1 - 6\phi_1)y \\ 0 & 0 & 0 & 0 \end{bmatrix}_{2 \times 20} \quad (75)$$

where ϕ_i are the Hermitian polynomials given in Eq. (23). The incremental displacement vector, for element interface k , in the local element system is given by

$$\mathbf{u}^{kT} = \begin{bmatrix} u_1^k & \theta_{x_1}^k & \theta_{y_1}^k & \theta_{z_1}^k & u_2^k & \theta_{x_2}^k & \theta_{y_2}^k & \theta_{z_2}^k \\ \\ u_1^{k+1} & \theta_{x_1}^{k+1} & \theta_{y_1}^{k+1} & \theta_{z_1}^{k+1} & u_2^{k+1} & \theta_{x_2}^{k+1} & \theta_{y_2}^{k+1} & \theta_{z_2}^{k+1} \\ \\ \beta_1^k & \beta_2^k & \beta_1^{k+1} & \beta_2^{k+1} \end{bmatrix} \quad (76)$$

In a linear-elastic slip model, with no damage in the interface material, the stiffness matrix is obtained analytically, as shown in Appendix B.4. However, in models with slip condition between layers, the stiffness matrix is obtained from the integral form in Eq. (74), which must be solved numerically.

2.11.

Transverse Displacement Compatibility

At any spatial configuration, all element layers share the same axis, allowing slip between layers in axial and circumferential directions only, but requiring compatible transverse displacements. In the present work, this constraint condition is applied by using the penalty method for simplicity, considering equality constraints. By this method, two degrees-of-freedom are physically linked through an elastic member, with the constraint condition being imposed numerically. The choice of the appropriate value for the elastic constant relies on a numerical trial procedure. Thus, if any two degrees-of-freedom (u_i and u_j) are

linked by a spring of stiffness k^p , the strain energy due to the relative displacement, to be added to the problem variational indicator, is given by

$$\pi^* = \frac{1}{2} \int_u k^p (u_j - u_i)^2 du \quad (77)$$

For a “large” penalty parameter k^p , the constraint condition is “numerically” imposed as $\delta\pi^*$ approaches to zero. A penalty matrix is then obtained, by means of the Principle of Virtual Work, from

$$\delta\pi^* = \int_u k^p (u_j - u_i) \delta(u_j - u_i) du \quad (78)$$

that results in the following penalty matrix (\mathbf{k}^p) associated to the vector (\mathbf{u}_p):

$$\mathbf{k}^p = \begin{bmatrix} k^p & -k^p \\ -k^p & k^p \end{bmatrix} \quad \text{and} \quad \mathbf{u}_p = \begin{bmatrix} u_i \\ u_j \end{bmatrix} \quad (79)$$

The choice of the penalty parameter k^p is generally left to numerical investigation. In the present study, this parameter has been taken to be equal to the largest numerical value amongst all terms in the element stiffness matrix.

For the multilayer pipe beam element, the transverse degrees-of-freedom constraints between any layer (k) and the reference layer ($k = 1$) are obtained by using the following penalty matrix

$$\mathbf{K}_p^k = \begin{bmatrix} k^p & 0 & -k^p & 0 & 0 & 0 & 0 & 0 \\ 0 & k^p & 0 & -k^p & 0 & 0 & 0 & 0 \\ -k^p & 0 & k^p & 0 & 0 & 0 & 0 & 0 \\ 0 & -k^p & 0 & k^p & 0 & 0 & 0 & 0 \\ 0 & 0 & 0 & 0 & k^p & 0 & -k^p & 0 \\ 0 & 0 & 0 & 0 & 0 & k^p & 0 & -k^p \\ 0 & 0 & 0 & 0 & -k^p & 0 & k^p & 0 \\ 0 & 0 & 0 & 0 & 0 & -k^p & 0 & k^p \end{bmatrix} \quad (80)$$

which is associated to the following nodal incremental displacement vector:

$$\mathbf{u}_p^{kT} = [v_1^1 \quad w_1^1 \quad v_1^k \quad w_1^k \quad v_2^1 \quad w_2^1 \quad v_2^k \quad w_2^k] \quad (81)$$

Special attention must be given to the transformations applied to the penalty matrix, as it must be computed in the nodal reference system. As shown in Figure 11, for two initially aligned elements, in the element system, the penalty stiffness

at the adjoining node of adjacent elements “1” and “2” are applied in different directions. To overcome this difficulty nodal reference system is used and, in this case, stiffness contributions from both elements are applied in a unique direction.

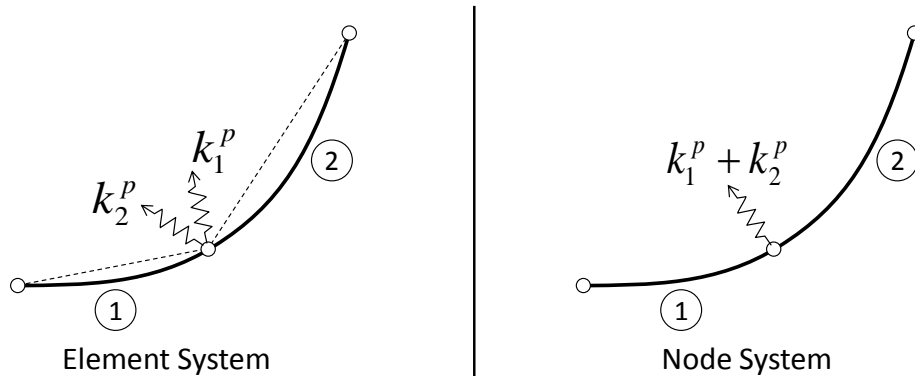


Figure 11: Reference Systems for Penalty Method.

2.12.

Element Stiffness Matrix

The multilayered pipe beam element can be considered as “fully bonded” or “unbonded”, depending on the type of interaction between layers. In the unbonded element, the stiffness matrix (\mathbf{K}_e) is obtained by using regular FEM assemblage process, accounting for the influence of each layer and interface. The element penalty matrix (\mathbf{K}_p) is referred to each node reference system and is obtained by using the same procedure. After the assembly process, the element stiffness matrix (\mathbf{K}_e) is of order $14n_{layers} \times 14n_{layers}$. In the fully bonded condition, there is no contribution of interface and penalty matrices, and the element matrix is obtained by simply adding all layer matrices. In this case the element matrix dimension is 14×14 . Eq. (82) shows both processes.

$$\left. \begin{aligned}
 \mathbf{K}_{lay} &= \mathbf{A} \sum_{k=1}^{n_{layers}} (\mathbf{K}_L^k + \mathbf{K}_G^k) \\
 \mathbf{K}_{int} &= \mathbf{A} \sum_{k=1}^{n_{layers}-1} (\mathbf{K}_i^k) \\
 \mathbf{K}_e &= \mathbf{K}_{lay} + \mathbf{K}_{int}; \quad \text{element reference system} \\
 \mathbf{K}_p &= \mathbf{A} \sum_{k=2}^{n_{layers}} (\mathbf{K}_p^k); \quad \text{nodal reference system} \\
 \mathbf{K}_e &= \sum_{k=1}^{n_{layers}} (\mathbf{K}_L^k + \mathbf{K}_G^k)
 \end{aligned} \right\} \begin{array}{l} \rightarrow \text{unbonded} \\ \rightarrow \text{fully bonded} \end{array} \quad (82)$$

where \mathbf{K}_{lay} is the element layers stiffness matrix; \mathbf{K}_{int} is the element interfaces stiffness matrix; \mathbf{K}_e is the element stiffness matrix including all layers and interfaces; \mathbf{K}_p is the element penalty matrix; \mathbf{A} stands for the assembly process.

In both cases, static condensation on the generalized degrees-of-freedom for shear strains is used to reduce matrix dimension. In this way, \mathbf{K}_e matrix is partitioned as

$$\mathbf{K}_e = \begin{bmatrix} \mathbf{K}_{uu} & \mathbf{K}_{u\beta} \\ \mathbf{K}_{\beta u} & \mathbf{K}_{\beta\beta} \end{bmatrix} \quad (83)$$

and, by applying static condensation, the element stiffness matrix becomes

$$\mathbf{K}_e = \mathbf{K}_e^u - \mathbf{K}_e^\beta \quad (84)$$

where

$$\mathbf{K}_e^u = \mathbf{K}_{uu} \quad \text{and} \quad \mathbf{K}_e^\beta = \mathbf{K}_{u\beta} \mathbf{K}_{\beta\beta}^{-1} \mathbf{K}_{\beta u}. \quad (85)$$

3. Fluid Loads

In a submerged pipeline various types of loadings due to internal and external fluid flows may occur, such as, internal fluid induced vibrations due to slugging flow and vortex induced vibrations, respectively. However, in this work only the internal fluid weight and hydrostatic (buoyancy) and hydrodynamic (drag forces) loads due to the external fluid are considered in the multilayered element formulation. Figure 12 shows the equivalent nodal forces in four possible relative positions of a two node pipe beam element in contact with the external fluid: (a) totally dry; (b) partially submerged with first node inside the fluid; (c) partially submerged with last node inside the fluid; and (d) totally submerged. Additionally, the following conditions may occur: open pipe, closed pipe with internal fluid and closed empty pipe.

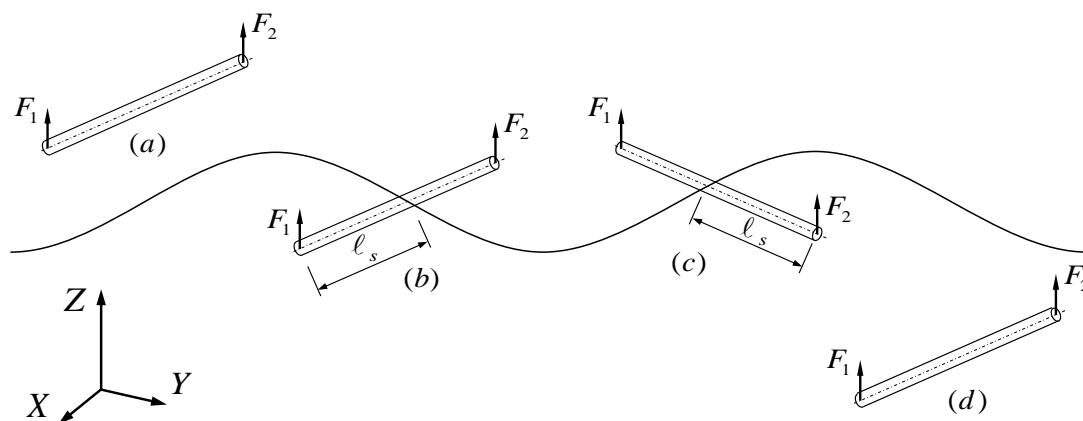


Figure 12: Fluid Load on a Beam Element.

3.1. Fluid Weight and Buoyancy Forces

From equilibrium conditions, the equivalent nodal forces due to internal fluid weight and external fluid buoyancy are obtained. Equations (86) and (87)

present these equivalent nodal forces associated to each element layer for the open and closed pipe conditions, respectively.

$$F_1^k = \gamma_e A^k \ell \alpha_1 \quad \text{and} \quad F_2^k = \gamma_e A^k \ell \alpha_2 \quad (86)$$

$$\begin{aligned} F_1^1 &= -\frac{\gamma_i A_i \ell}{2}; \quad F_1^k = 0 \quad (1 < k < N_{\text{layers}}); \quad F_1^{N_{\text{layers}}} = \gamma_e A_e \ell \alpha_1 \\ F_2^1 &= -\frac{\gamma_i A_i \ell}{2}; \quad F_2^k = 0 \quad (1 < k < N_{\text{layers}}); \quad F_2^{N_{\text{layers}}} = \gamma_e A_e \ell \alpha_2 \end{aligned} \quad (87)$$

where F_1^k, F_2^k are the layer- k equivalent nodal forces; γ_i, γ_e are the internal and external fluid densities, respectively; A_i, A_e are the internal and external areas, respectively; A^k is the layer- k cross section area; ℓ is the element length; and α_1, α_2 are coefficients to transfer the uniform distributed loads to element nodes, as given in Table 2.

Table 2: Distributed Loads Proportional Coefficients.

| Element relative position | α_1 | α_2 |
|--|---|---|
| (a) Totally dry | 0 | 0 |
| (b) Partially submerged (node 1 inside fluid) | $\frac{\ell_s}{\ell} \left(1 - \frac{\ell_s}{2\ell}\right)$ | $\frac{1}{2} \left(\frac{\ell_s}{\ell}\right)^2$ |
| (c) Partially submerged (node 2 inside fluid) | $\frac{1}{2} \left(\frac{\ell_s}{\ell}\right)^2$ | $\frac{\ell_s}{\ell} \left(1 - \frac{\ell_s}{2\ell}\right)$ |
| (d) Totally submerged | $\frac{1}{2}$ | $\frac{1}{2}$ |

Where ℓ_s is the submerged length as shown in Figure 12.

3.2.

Hydrodynamic Loads

Fluid-structure interaction is generally characterized by drag and inertia (added mass) forces, obtained by using Morison's equation (Morison et al., [39]), which is a semi-empirical equation for the hydrodynamic forces on a cylinder in oscillatory flow. This equation can be used with confidence in structural analysis of risers, provided the pipe diameter is at least one order of magnitude smaller

compared to the wavelength of the oscillatory flow. For a moving pipe in an oscillatory flow, Morison's equation is represented by three components as follows:

(1) Transverse drag forces:

$$\mathbf{f}_{Dn} = \frac{1}{2} \rho_f D C_{Dn} |\dot{\mathbf{u}}_{fn} - \dot{\mathbf{u}}_n| (\dot{\mathbf{u}}_{fn} - \dot{\mathbf{u}}_n) \quad (88)$$

(2) Tangential drag forces:

$$\mathbf{f}_{Dt} = \frac{1}{2} \rho_f D C_{Dt} |\dot{\mathbf{u}}_{ft} - \dot{\mathbf{u}}_t| (\dot{\mathbf{u}}_{ft} - \dot{\mathbf{u}}_t) \quad (89)$$

(3) Transverse inertia forces:

$$\mathbf{f}_I = \rho_f \frac{\pi D^2}{4} C_M \ddot{\mathbf{u}}_{fn} - \rho_f \frac{\pi D^2}{4} (C_M - 1) \ddot{\mathbf{u}}_n \quad (90)$$

where ρ_f is the fluid mass density; D is the hydrodynamic diameter of the pipe; C_{Dn} and C_{Dt} are the normal and tangential drag coefficients, respectively, which depend on the pipe cross section geometry and roughness (for a bare cylinder: $C_{Dn} = 1.0$ and $C_{Dt} = 0.0$); C_M is the transverse inertia coefficient; $\dot{\mathbf{u}}_{fn}$ and $\dot{\mathbf{u}}_n$ are the fluid and structure velocity vectors, respectively, both normal to the pipe; $\dot{\mathbf{u}}_{ft}$ and $\dot{\mathbf{u}}_t$ are the fluid and structure velocity vectors, respectively, in the pipe tangential direction; $\ddot{\mathbf{u}}_{fn}$ and $\ddot{\mathbf{u}}_n$ are the fluid and structure acceleration vectors, respectively, both normal to the pipe centerline.

The total hydrodynamic load per unit length is the vector sum of Eqs. (88) to (90). In the multilayered element formulation, the nodal equivalent hydrodynamic forces are obtained assuming a linear variation along the length, i.e.:

$$\mathbf{f}_h(\xi) = \left(1 - \frac{\xi}{\ell}\right) \mathbf{f}_h^1 + \left(\frac{\xi}{\ell}\right) \mathbf{f}_h^2 \quad (91)$$

where \mathbf{f}_h^1 and \mathbf{f}_h^2 are the hydrodynamic load per unit length at nodes 1 and 2, respectively, obtained from Eqs. (88) to (90); ξ is the local coordinate along element axis; and ℓ is the element length.

The distributed loading in Eq. (91) is then transferred to the nodes in the external layer degrees-of-freedom, by using the element interpolation matrix, i.e.:

$$\mathbf{F}_h = \int_0^\ell \mathbf{H}^T \mathbf{f}_h d\xi \quad (92)$$

where \mathbf{F}_h is the nodal vector of hydrodynamic loads applied to the external layer.

4.

Implementation of the Three-Dimensional Multilayer Pipe Beam Element

The three-dimensional multilayered element formulation has been implemented in a C++ code using object-oriented techniques, such as proposed by Lages et al. [33]. The program uses some of the algorithms presented by Leon et al. [34], together with the HHT time integration algorithm (Hilber et al. [35]), to solve the nonlinear dynamic equilibrium equations. Details of this implementation are presented in the following sections.

4.1.

Global Equilibrium Equation

The present formulation includes large displacements and nonlinear constitutive relations within the interface material. Numerical solutions are obtained using an incremental procedure for equilibrium. The global dynamic equilibrium equation is presented in the following matrix form:

$${}^{t+\Delta t}\mathbf{M} {}^{t+\Delta t}\ddot{\mathbf{U}} + {}^{t+\Delta t}\mathbf{D} {}^{t+\Delta t}\dot{\mathbf{U}} + {}^{t+\Delta t}\mathbf{K} \Delta\mathbf{U} = {}^{t+\Delta t}\mathbf{R} - {}^t\mathbf{F} \quad (93)$$

where \mathbf{M} , \mathbf{D} and \mathbf{K} are the structure global mass, damping and stiffness matrices at time $t + \Delta t$, respectively, obtained from the element matrices through an assemblage process; $\ddot{\mathbf{U}}$ and $\dot{\mathbf{U}}$ are the global nodal acceleration and velocities vectors; $\Delta\mathbf{U}$ is the global incremental displacements vector; \mathbf{R} is the global external loading vector; and \mathbf{F} is the structure global internal forces vector.

A step-by-step procedure has been implemented considering

$$\begin{aligned}
{}^{t+\Delta t}\ddot{\mathbf{U}} &= \frac{1}{\beta\Delta t^2}\Delta\mathbf{U} - \frac{1}{\beta\Delta t}{}^t\dot{\mathbf{U}} - \left(\frac{1}{2\beta} - 1\right){}^t\ddot{\mathbf{U}} \\
{}^{t+\Delta t}\dot{\mathbf{U}} &= {}^t\dot{\mathbf{U}} + (1-\gamma)\Delta t{}^t\ddot{\mathbf{U}} + \gamma\Delta t{}^{t+\Delta t}\ddot{\mathbf{U}} \\
{}^{t+\Delta t}\mathbf{U} &= {}^t\mathbf{U} + \Delta\mathbf{U}
\end{aligned} \tag{94}$$

where Δt is the time increment; ${}^t\mathbf{U}$ is a known solution at time t ; β and γ are constants that define the time integration algorithm. In the case of HHT algorithm, we have:

$$\begin{aligned}
\beta &= \frac{1}{4}(1-\alpha)^2 \\
\gamma &= \frac{1}{2} - \alpha
\end{aligned} \tag{95}$$

with $-1/3 \leq \alpha \leq 0$.

4.2.

Element Updating Procedure

The nonlinear equilibrium equation, shown in Eq. (93), is solved by using an iterative and incremental algorithm. Thus, at each equilibrium iteration all stiffness matrices and internal force vectors, for each element, must be updated. In the following sections, the formulation for large displacements and rotations is presented. An updating procedure applied to all multilayered pipe beam element matrices is also detailed. It uses the element incremental displacements and rotations, obtained in the solution process at each iteration- i , to update all element reference systems. The procedure is performed according to the following steps:

Step 1. Nodal positions and direction cosines of the element (straight axis direction) are updated from the incremental displacements ($\Delta\mathbf{u}^i$) obtained in the previous iteration;

Step 2. Element and nodal transformation matrices are updated:

Step 2.1. Nodal rotation matrices ($\mathbf{R}_{n1}^{k(i)}$ and $\mathbf{R}_{n2}^{k(i)}$), for each layer, are updated from incremental rotations at each node: nodal incremental rotation matrices ($\mathbf{R}_{inc1}^{k(i)}$ and $\mathbf{R}_{inc2}^{k(i)}$) are obtained from the rotation increments

using Eq. (2). Previous nodal rotation matrices are pre-multiplied by each of these matrices, i.e.,

$$\mathbf{R}_{n1}^{k(i)} = \mathbf{R}_{incl}^{k(i)} \mathbf{R}_{n1}^{k(i-1)} \quad \text{and} \quad \mathbf{R}_{n2}^{k(i)} = \mathbf{R}_{inc2}^{k(i)} \mathbf{R}_{n2}^{k(i-1)} \quad (96)$$

Step 2.2. The element transformation matrix (\mathbf{R}_e^i) is obtained from the straight element axis (defined by current nodal point positions) and from nodal rotation matrices: the first row in the element rotation matrix (\mathbf{R}_e^i) is given by the updated direction cosines of the element (vector \mathbf{X}); the second row (vector \mathbf{Y}) is given by averaging the second rows of the reference layer nodal matrices $\mathbf{R}_{n1}^{1(i)}$ (vector \mathbf{y}_1^1) and $\mathbf{R}_{n2}^{1(i)}$ (vector \mathbf{y}_2^1); and the third row (vector \mathbf{Z}) is obtained from the cross product between the first and second row ($\mathbf{Z} = \mathbf{X} \times \mathbf{Y}$);

Step 3. Relative displacements vectors (\mathbf{u}_r^i and \mathbf{u}_p^i), in the local element and nodal reference systems, respectively, are then calculated.

Step 3.1. Relative displacements between layers are obtained as follows:

Step 3.1.1. First, the relative axial displacement of the reference layer (innermost layer) is computed subtracting its updated deformed length (ℓ^i) from element initial, non-deformed, length (ℓ_0):

$$\Delta \ell^i = \ell^i - \ell_0 \quad (97)$$

Step 3.1.2. Then, nodal relative displacements between each layer (k) and the reference layer ($k = 1$) are computed in the global reference system. This operation must be done individually, for each node:

$$\Delta \mathbf{u}_1^k = \mathbf{u}_1^k - \mathbf{u}_1^1 \quad \text{and} \quad \Delta \mathbf{u}_2^k = \mathbf{u}_2^k - \mathbf{u}_2^1, \quad k = 2 \text{ to } N_{layers} \quad (98)$$

Step 3.1.3. The nodal relative displacements for each layer are transferred to local element system and also to the nodal reference systems:

$$\begin{cases} \Delta \mathbf{u}_{e1}^k = \mathbf{R}_e^{(i)T} \Delta \mathbf{u}_1^k & \text{and} & \Delta \mathbf{u}_{e2}^k = \mathbf{R}_e^{(i)T} \Delta \mathbf{u}_2^k \\ \Delta \mathbf{u}_{n1}^k = \mathbf{R}_{n1}^{(i)T} \Delta \mathbf{u}_1^k & \text{and} & \Delta \mathbf{u}_{n2}^k = \mathbf{R}_{n2}^{(i)T} \Delta \mathbf{u}_2^k \end{cases} \quad k = 2 \text{ to } N_{layers} \quad (99)$$

Step 3.2. Nodal relative rotation between each layer and the element straight axis are obtained from the nodal transformation matrices of each layer and from the element transformation matrix in the reference

configuration. According to Crisfield [21], these rotation angles can be obtained from the following expressions

$$\begin{aligned} 2 \sin(\Delta\theta_{1x}^k) &= -\mathbf{z}_1^k \mathbf{Y} + \mathbf{y}_1^k \mathbf{Z} & 2 \sin(\Delta\theta_{2x}^k) &= -\mathbf{z}_2^k \mathbf{Y} + \mathbf{y}_2^k \mathbf{Z} \\ 2 \sin(\Delta\theta_{1y}^k) &= -\mathbf{x}_1^k \mathbf{Z} + \mathbf{z}_1^k \mathbf{X} & \text{and} & & 2 \sin(\Delta\theta_{2y}^k) &= -\mathbf{x}_2^k \mathbf{Z} + \mathbf{z}_2^k \mathbf{X} \\ 2 \sin(\Delta\theta_{1z}^k) &= -\mathbf{y}_1^k \mathbf{X} + \mathbf{x}_1^k \mathbf{Y} & 2 \sin(\Delta\theta_{2z}^k) &= -\mathbf{y}_2^k \mathbf{X} + \mathbf{x}_2^k \mathbf{Y} \end{aligned} \quad (100)$$

Step 3.3. The vector of relative displacements (\mathbf{u}_r^i) is assembled on the local system of the element from the nodal relative displacements ($\Delta\mathbf{u}_{e1}^k$ and $\Delta\mathbf{u}_{e2}^k$) and rotation vectors ($\Delta\theta_1^k$ e $\Delta\theta_2^k$) of each layer. For a given layer- k , vector \mathbf{u}_r^k is obtained as:

$$\begin{aligned} \mathbf{u}_{r(j)}^k &= \Delta\mathbf{u}_{e1(j)}^k, & j &= 1 \text{ to } 3 \\ \mathbf{u}_{r(j+3)}^k &= \Delta\theta_{1(j)}^k, & j &= 1 \text{ to } 3 \\ \mathbf{u}_{r(7)}^k &= \Delta\mathbf{u}_{e2(1)}^k + \Delta\ell^i \\ \mathbf{u}_{r(j+6)}^k &= \Delta\mathbf{u}_{e2(j)}^k, & j &= 2 \text{ to } 3 \\ \mathbf{u}_{r(j+9)}^k &= \Delta\theta_{2(j)}^k, & j &= 1 \text{ to } 3 \end{aligned} \quad (101)$$

Step 3.4. The vector of relative displacements (\mathbf{u}_p^i), used in the calculation of penalty internal forces, is assembled. This vector refers to relative displacements in two different reference systems, one for each node, and is assembled from the nodal displacements vectors of each layer ($\Delta\mathbf{u}_{n1}^k$ and $\Delta\mathbf{u}_{n2}^k$). The vector \mathbf{u}_p^k , for layer- k , is obtained as follows:

$$\begin{aligned} \mathbf{u}_{p(j)}^k &= \Delta\mathbf{u}_{n1(j)}^k, & j &= 1 \text{ to } 3 \\ \mathbf{u}_{p(j+6)}^k &= \Delta\mathbf{u}_{n2(1)}^k, & j &= 1 \text{ to } 3 \end{aligned} \quad (102)$$

Step 4. Internal force vector contributions are calculated in their corresponding reference systems and then transferred to global coordinate system as follows:

$$\begin{aligned} \mathbf{f}_{lay}^i &= \mathbf{K}_{lay} \mathbf{u}_r^i \\ \mathbf{f}_{int}^i &= \mathbf{K}_{int} \mathbf{u}_r^i \\ \mathbf{f}_p^i &= \mathbf{K}_p \mathbf{u}_p^i \end{aligned} \quad (103)$$

Step 4.1. Total internal force vector, in the global reference system, is thus obtained

$$\mathbf{f}_g^i = \overline{\mathbf{R}}_e^{(i)}(\mathbf{f}_{lay}^i + \mathbf{f}_{int}^i) + \overline{\mathbf{R}}_n^{(i)}\mathbf{f}_p^i \quad (104)$$

where \mathbf{f}_{lay}^i is the element internal forces vector due to deformation at layers; \mathbf{f}_{int}^i is the element internal forces vector due to deformation at interfaces; \mathbf{f}_p^i is the element internal forces vector due to penalty method; and $\overline{\mathbf{R}}_e^{(i)}$ and $\overline{\mathbf{R}}_n^{(i)}$ are transformation matrices (with same dimension as the element total number of degrees-of-freedom)

$$\overline{\mathbf{R}}_e^i = \begin{bmatrix} \mathbf{R}_e^i & 0 & 0 & 0 & 0 \\ 0 & \mathbf{R}_e^i & 0 & 0 & 0 \\ 0 & 0 & \mathbf{R}_e^i & 0 & 0 \\ 0 & 0 & 0 & \ddots & 0 \\ 0 & 0 & 0 & 0 & \mathbf{R}_e^i \end{bmatrix} \quad \text{and} \quad \overline{\mathbf{R}}_n^i = \begin{bmatrix} \mathbf{R}_{n1}^i & 0 & 0 & 0 & 0 \\ 0 & \mathbf{R}_{n1}^i & 0 & 0 & 0 \\ 0 & 0 & \ddots & 0 & 0 \\ 0 & 0 & 0 & \mathbf{R}_{n2}^i & 0 \\ 0 & 0 & 0 & 0 & \mathbf{R}_{n2}^i \end{bmatrix} \quad (105)$$

where \mathbf{R}_e^i and \mathbf{R}_n^i are as defined in steps 2.1 and 2.2.

Step 5. The element stiffness matrix (\mathbf{K}_e^i) and penalty matrix (\mathbf{K}_p^i) are then assembled in their respective local coordinate systems, from the matrices of each layer and interface, and then transferred to the global system to obtain (\mathbf{K}_g^i), as follows:

$$\mathbf{K}_g^i = \overline{\mathbf{R}}_e^{(i)T} \mathbf{K}_e^i \overline{\mathbf{R}}_e^{(i)} + \overline{\mathbf{R}}_n^{(i)T} \mathbf{K}_p^i \overline{\mathbf{R}}_n^{(i)} \quad (106)$$

The mass and damping matrices are also assembled in the element reference system from each layer contribution and then transferred to the global reference system, as follows:

$$\begin{aligned} \mathbf{M}_g^i &= \overline{\mathbf{R}}_e^{(i)T} \mathbf{M}_e^i \overline{\mathbf{R}}_e^{(i)} \\ \mathbf{D}_g^i &= \overline{\mathbf{R}}_e^{(i)T} \mathbf{D}_e^i \overline{\mathbf{R}}_e^{(i)} \end{aligned} \quad (107)$$

5. Pipe-Soil Interaction

In practical riser analysis, since part of the riser lies on the seabed, an appropriate representation of riser-soil interaction is very important. The exact representation of this problem is not an easy task due to the number of variables and uncertainties involved in the problem definition. These are related to soil non-linear stiffness, trench formation and soil resistance during cyclic loading. In the context of the Finite Element Method, a simple and efficient approach is to assume the pipeline lying on a “mattress of independent nonlinear springs”, acting on the element nodes, as shown in Figure 13. The characteristics of these springs depend on several factors, such as the type of soil considered, diameter of the riser, and level of pipe embedment in soil.

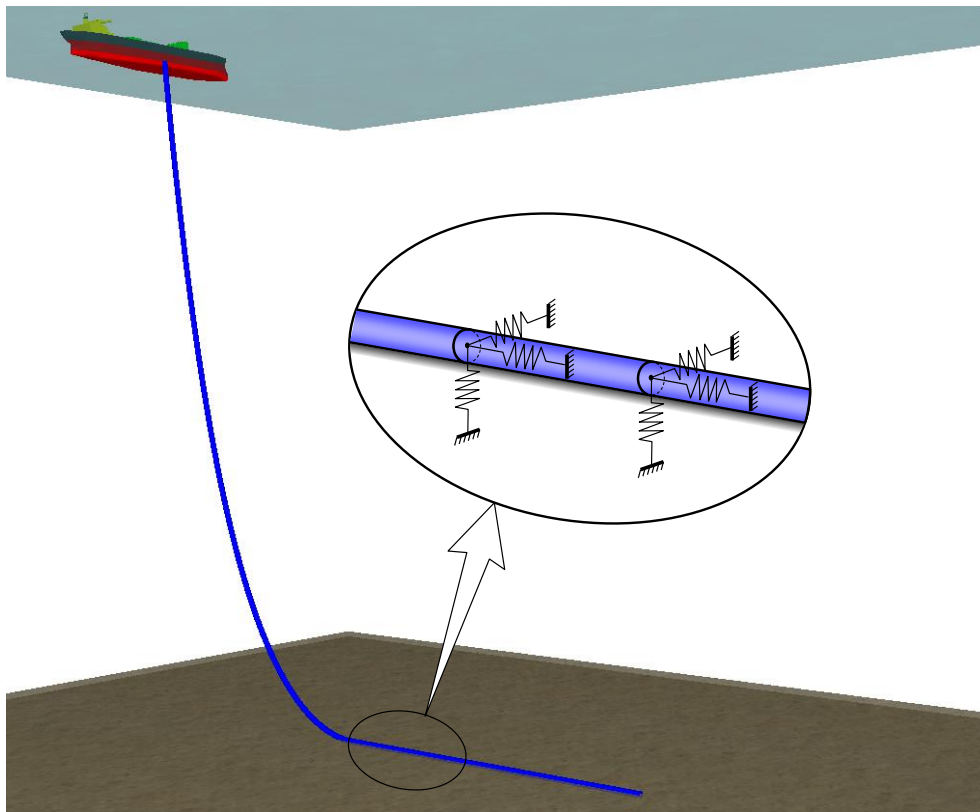


Figure 13: Soil Springs.

5.1.

Normal Reaction

In the present work, the soil reference system is defined with the z -axis normal to the soil surface at the contact point. The x -axis lies on the plane defined by the normal and the element axis and the y -axis in the lateral direction. The contact conditions are characterized by the relative displacements in the normal (u_z), longitudinal (u_x) and lateral (u_y) directions, as shown in Figure 14.

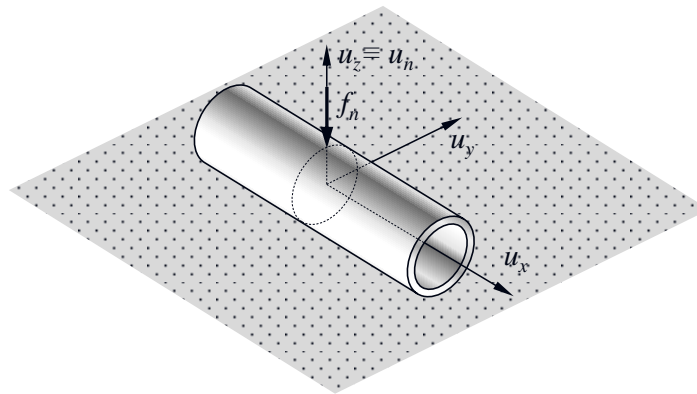


Figure 14: Pipe-Soil Relative Displacements.

A bilinear model is used to represent the normal contact force (f_n) between soil and pipe, as shown in Figure 15.

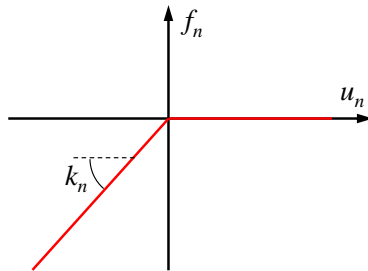


Figure 15: Normal Contact Model.

The normal contact force is obtained from:

$$f_n = \begin{cases} k_n u_n, & \text{if } u_n < 0 \\ 0 & \text{if } u_n \geq 0 \end{cases} \quad (108)$$

where f_n is the normal contact force; k_n is the normal soil stiffness; u_n is the relative displacement between the soil surface and the pipe in the normal direction (a negative value means penetration of pipe in soil).

5.2.

Longitudinal and Lateral Reactions

As shown in Figure 16, longitudinal and lateral contact conditions are driven by two different phenomena: when a pipe moves in the lateral direction, tangent to the soil surface, the soil cohesion may brake and a portion of soil is dragged by the pipe wall. On the other hand, for relative movement in the longitudinal direction distributed friction forces arise due to contact between the soil and external pipe wall. The exact interaction between these two phenomena is difficult to formulate. In this work, the problem is solved by assuming two simplified models: 1) full interaction (coupled model); and 2) independent friction model for each direction (uncoupled model), as described in the following sections.

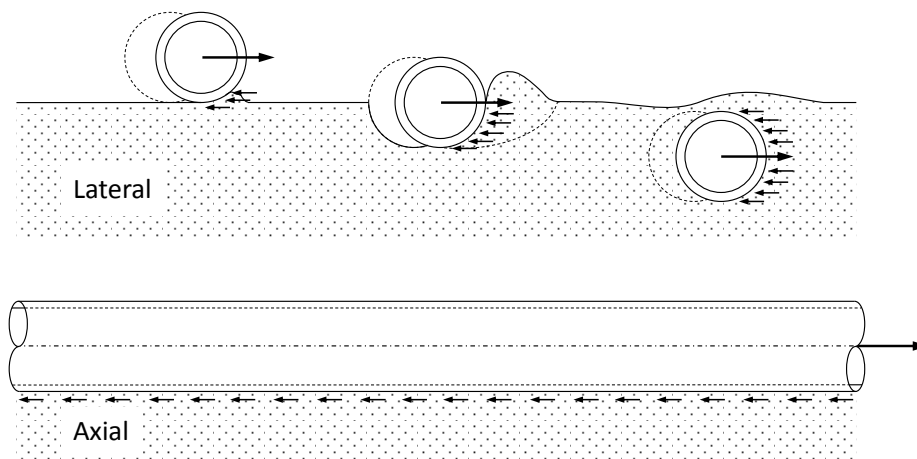


Figure 16: Lateral and Longitudinal Contact.

5.2.1.

Coupled Friction

This model assumes full interaction between friction forces in the longitudinal and lateral directions by considering an “equivalent” force that follows the model:

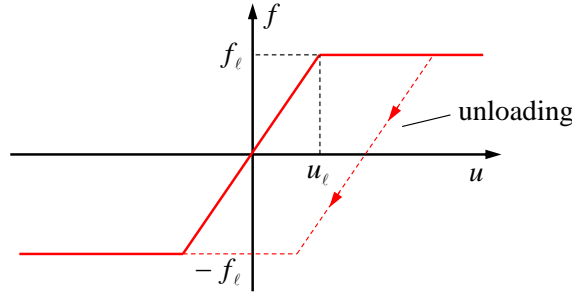


Figure 17: Pipe-Soil Friction Model.

where $f_\ell = \mu|f_n|$ and u_ℓ are the limit force and displacement that defines the elastic regime, respectively; μ is the friction coefficient; f_n is the normal contact force defined in Eq. (108);

Thus, within the elastic regime, friction forces are given by:

$$\mathbf{f} = \mathbf{k}\mathbf{u} \quad (109)$$

where \mathbf{f} is the vector of friction forces; \mathbf{u} is the vector of relative displacements between pipe and soil:

$$\mathbf{u} = \begin{bmatrix} u_x \\ u_y \end{bmatrix} \quad (110)$$

and \mathbf{k} is the frictional stiffness matrix, given by:

$$\mathbf{k} = \begin{bmatrix} k_x & 0 \\ 0 & k_y \end{bmatrix} \quad (111)$$

with k_x and k_y being the contact stiffness in the longitudinal and lateral directions, respectively, defined as:

$$k_x = \frac{f_{\ell_x}}{u_{\ell_x}} \quad \text{and} \quad k_y = \frac{f_{\ell_y}}{u_{\ell_y}} \quad (112)$$

Within the inelastic regime, friction forces are determined by using the following yielding-type function:

$$\phi(\mathbf{f}) = \|\mathbf{f}\| - \|\mathbf{f}_\ell\| = 0 \quad (113)$$

where $\|\mathbf{f}\| = \sqrt{f_x^2 + f_y^2}$ with f_x and f_y being the friction forces in the longitudinal and lateral direction, respectively.

According to Simo and Hughes [31], this type of nonlinear problem can be characterized by means of the following set of equations:

$$\begin{aligned}\mathbf{u} &= \mathbf{u}^e + \mathbf{u}^{in} \\ \mathbf{f} &= \mathbf{k}\mathbf{u}^e = \mathbf{k}(\mathbf{u} - \mathbf{u}^{in}) \\ \Delta\mathbf{u}^{in} &= \lambda\hat{\mathbf{r}}(\mathbf{f}) = \lambda \frac{d\phi}{d\mathbf{f}}, \quad \lambda \geq 0\end{aligned}\quad (114)$$

where \mathbf{u} , \mathbf{u}^e and \mathbf{u}^{in} are the vectors of total, elastic and inelastic displacements; \mathbf{f} is the vector of friction forces; $\Delta\mathbf{u}^{in}$ is the vector of inelastic displacement increments; λ is the inelastic displacement increment parameter to be determined; $\hat{\mathbf{r}}(\mathbf{f})$ is a unit vector that indicates the “yield” direction and is given by:

$$\hat{\mathbf{r}}(\mathbf{f}) = \frac{1}{\|\mathbf{f}\|} \begin{bmatrix} f_x \\ f_y \end{bmatrix} \quad (115)$$

The loading or unloading condition is expressed by the following conditions:

$$\begin{aligned}\phi &\leq 0 \\ \lambda &\geq 0 \\ \phi\lambda &= 0\end{aligned}\quad (116)$$

An additional condition, referred to as consistency condition, is necessary to make sure that the friction forces are confined to the yield criteria (113) throughout loading, i.e.:

$$\dot{\phi}\lambda = 0 \quad (117)$$

Thus, the associated mathematical problem consists in: given $\{\mathbf{u}_n, \mathbf{u}_n^{in}, \mathbf{f}_n\}$ and \mathbf{u}_{n+1} , obtain \mathbf{u}_{n+1}^{in} and \mathbf{f}_{n+1} . The solution for this problem is obtained by using a backward Euler scheme. Thus, Eqs. (114) can be rewritten in the following discrete form:

$$\begin{aligned}\mathbf{u}_{n+1} &= \mathbf{u}_n + \Delta\mathbf{u} \\ \mathbf{u}_{n+1}^{in} &= \mathbf{u}_n^{in} + \Delta\mathbf{u}^{in} \\ \mathbf{f}_{n+1} &= \mathbf{f}_n + \mathbf{k}(\Delta\mathbf{u} - \Delta\mathbf{u}^{in}) = \mathbf{f}_n + \Delta\mathbf{f} \\ \Delta\mathbf{u}^{in} &= \lambda\hat{\mathbf{r}}_{n+1}\end{aligned}\quad (118)$$

This problem is solved in two steps. First, an elastic displacement increment is assumed to obtain the following trial state:

$$\begin{aligned}
\mathbf{f}_{n+1}^* &= \mathbf{k}(\mathbf{u}_{n+1} - \mathbf{u}_n^{in}) \equiv \mathbf{f}_n + \mathbf{k}\Delta\mathbf{u}_n \\
\mathbf{u}_{n+1}^{in*} &= \mathbf{u}_n^{in} \\
\phi_{n+1}^* &= \|\mathbf{f}_{n+1}^*\| - \|\mathbf{f}_\ell\|
\end{aligned} \tag{119}$$

The trial state positiveness indicates if the displacement increment is in the elastic or inelastic regimen, according to the following criterion

$$\phi_{n+1}^* \begin{cases} \leq 0 \Rightarrow \text{elastic increment} : \lambda = 0 \\ > 0 \Rightarrow \text{inelastic increment} : \lambda > 0 \end{cases} \tag{120}$$

Under inelastic increments, evolution equations are expressed in terms of the trial state and the inelastic displacement increment modulus (λ), in the form:

$$\begin{aligned}
\mathbf{f}_{n+1} &= \mathbf{f}_{n+1}^* - \lambda \mathbf{k} \hat{\mathbf{r}}_{n+1} \\
\mathbf{u}_{n+1}^{in} &= \mathbf{u}_n^{in} + \lambda \hat{\mathbf{r}}_{n+1}
\end{aligned} \tag{121}$$

Considering the consistency condition (117), and according to Eq. (120), i.e. $\lambda > 0$, one gives

$$\dot{\phi} = \left(\frac{d\phi}{d\mathbf{f}} \right)^T \dot{\mathbf{f}} = \hat{\mathbf{r}}_{n+1}^T \dot{\mathbf{f}} = 0 \tag{122}$$

which can be rewritten in the form

$$\Delta\phi = \hat{\mathbf{r}}_{n+1}^T \Delta\mathbf{f} = 0 \tag{123}$$

Combining the third and fourth Eqs. (118) and (123), one obtains:

$$\hat{\mathbf{r}}_{n+1}^T \mathbf{k}(\Delta\mathbf{u} - \lambda \hat{\mathbf{r}}_{n+1}) = 0 \tag{124}$$

Solving for λ , results in:

$$\lambda = \frac{\hat{\mathbf{r}}_{n+1}^T \mathbf{k} \Delta\mathbf{u}}{\hat{\mathbf{r}}_{n+1}^T \mathbf{k} \hat{\mathbf{r}}_{n+1}} \tag{125}$$

The solution procedure is geometrically represented in Figure 18. Consider the yield surface at the elastic trial state. The elastic trial contact forces lies outside the admissible domain (i.e. outside the elastic domain). Once the parameter λ is determined, Eq. (121) is used to bring the soil state back to the admissible domain, i.e. lying on the yield surface. This procedure is called *radial return mapping algorithm* (Wilkins [32]).

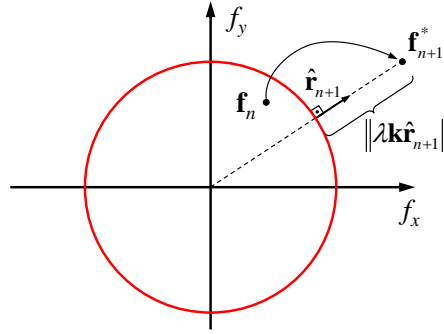


Figure18: Radial Return Mapping.

5.2.2.

Uncoupled Friction

In this proposed model, friction forces components are independently calculated, assuming the one-dimensional nonlinear model shown in Figure 17. Thus, within the elastic regime, friction forces are given by:

$$f = ku \quad (126)$$

where k is the lateral or longitudinal contact stiffness, given by:

$$k = \frac{f_\ell}{u_\ell} \quad (127)$$

Within the inelastic regime, friction forces are assumed to follow yield-type function:

$$\phi(f) = |f| - f_\ell = 0 \quad (128)$$

Using the same approach employed in the coupled model, Eqs. (114) are rewritten for the one-dimensional case in the form:

$$\begin{aligned} u &= u^e + u^{in} \\ f &= ku^e = k(u - u^{in}) \\ \Delta u^{in} &= \lambda \frac{d\phi}{df} = \lambda \text{sign}(f), \quad \lambda \geq 0 \end{aligned} \quad (129)$$

where u , u^e and u^{in} are the total, elastic and inelastic displacements in the friction force direction; f is the friction force; k is the elastic contact stiffness; and λ is the inelastic displacement increment parameter to be determined;

From Eq. (129), the trial elastic state is obtained by assuming an elastic displacement increment:

$$\begin{aligned}
f_{n+1}^* &= k(u_{n+1} - u_n^{in}) \equiv f_n + k\Delta u_n \\
u_{n+1}^{in*} &= u_n^{in} \\
\phi_{n+1}^* &= |f_{n+1}^*| - f_\ell
\end{aligned} \tag{130}$$

In the inelastic regime, the contact force f_{n+1} is expressed in terms of the trial force f_{n+1}^* and the inelastic displacement increment λ as follows:

$$\begin{aligned}
f_{n+1} &= k(u_{n+1} - u_{n+1}^{in}) \\
&= k(u_{n+1} - u_n^{in}) - k(u_{n+1}^{in} - u_n^{in}) \\
&= f_{n+1}^* - k\lambda \text{sign}(f_{n+1})
\end{aligned} \tag{131}$$

Therefore, since $\lambda > 0$, the actual state is written, in view of Eq. (131), as

$$\begin{aligned}
f_{n+1} &= f_{n+1}^* - k\lambda \text{sign}(f_{n+1}) \\
u_{n+1}^{in} &= u_n^{in} + \lambda \text{sign}(f_{n+1}) \\
\phi_{n+1} &= |f_{n+1}| - f_\ell = 0
\end{aligned} \tag{132}$$

Now the above problem is solved explicitly in terms of the trial elastic state by the following procedure. From first Eq. (132) and the identity $f = |f| \text{sign}(f)$, the following expression is obtained:

$$|f_{n+1}| \text{sign}(f_{n+1}) = |f_{n+1}^*| \text{sign}(f_{n+1}^*) - k\lambda \text{sign}(f_{n+1}) \tag{133}$$

Collecting terms, Eq. (133) results:

$$[|f_{n+1}| + k\lambda] \text{sign}(f_{n+1}) = |f_{n+1}^*| \text{sign}(f_{n+1}^*) \tag{134}$$

Since $\lambda > 0$ and $k > 0$, the term in brackets is necessarily positive, what requires that

$$\text{sign}(f_{n+1}) = \text{sign}(f_{n+1}^*) \tag{135}$$

and

$$|f_{n+1}| + k\lambda = |f_{n+1}^*| \tag{136}$$

From Eqs. (132) and (136) the yield criterion ϕ_{n+1} is written as

$$\phi_{n+1} = |f_{n+1}^*| - k\lambda - f_\ell = \phi_{n+1}^* - k\lambda = 0 \tag{137}$$

which solved for λ results in

$$\lambda = \frac{\phi_{n+1}^*}{k}. \quad (138)$$

The parameter λ is then used in the first two Eqs. (132) to update the soil state.

5.3.

Soil Transformation Matrix

In a Finite Element Analysis of pipelines, soil influence is considered in the formulation by adding the soil stiffness matrix and reaction force vectors to the element stiffness matrix and force vectors. These terms are numerically obtained in the soil local reference system and then, transferred to the global coordinate system by using the soil transformation matrix. This matrix is obtained by considering the unit vectors (\mathbf{x}_s , \mathbf{y}_s and \mathbf{z}_s) that defines the soil local reference system in a certain contact point, as shown in Figure 19, for a general case representing an irregular seabed.

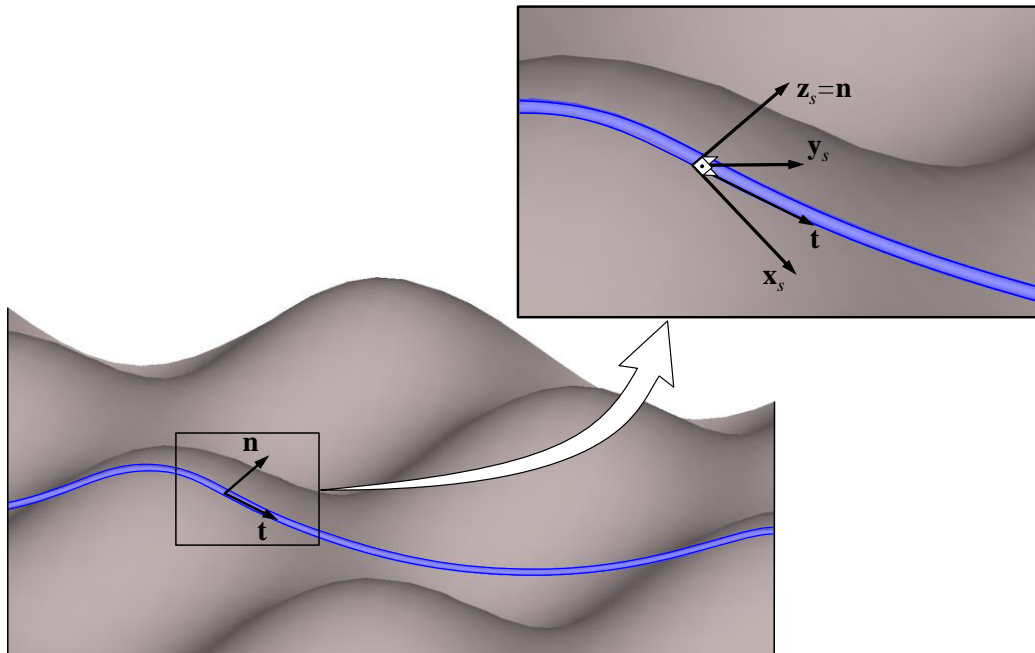


Figure 19: Soil Reference System.

The soil reference system is obtained from the unit vector (\mathbf{n}), normal to the soil in the contact point, and from the unit vector (\mathbf{t}), tangent to the deformed pipe, as shown in Eq. (139). Thus, the following vector definitions are obtained

$$\mathbf{y}_s = \frac{\mathbf{n} \times \mathbf{t}}{|\mathbf{n} \times \mathbf{t}|}, \quad \mathbf{z}_s = \mathbf{n} \quad \text{and} \quad \mathbf{x}_s = \mathbf{y}_s \times \mathbf{z}_s \quad (139)$$

where \mathbf{x}_s , \mathbf{y}_s and \mathbf{z}_s are the unit vectors of the soil reference system.

5.4. Numerical Implementation

In a riser analysis with the Finite Element Method, the equilibrium equation is solved using an iterative and incremental algorithm, due to the nonlinear characteristics of the problem. Thus, at each iteration the soil state at each element node must be updated. The procedure to calculate the soil stiffness matrix and reaction forces vector is presented as follows:

Step 1. Get the current nodal position (x_n, y_n, z_n) ;

Step 2. Get the seabed elevation (z_s) and normal vector (\mathbf{n}) at current node position:

$$z_s = Z_s(x_n, y_n) \quad \text{and} \quad \mathbf{n} = \mathbf{n}_s(x_n, y_n) \quad (140)$$

where $Z_s(x, y)$ is a function that defines the seabed geometry; $\mathbf{n}_s(x, y)$ is the unit vector normal to the surface defined by $Z_s(x, y)$.

Step 3. Check if the pipe element node is in contact with the soil:

Step 3.1. Obtain the penetration

$$u_n = (z_s - z_n)n_z$$

Step 3.2. If $(u_n > 0)$ then proceed to step 4 - contact is achieved.

Step 3.3. Else, no contact condition

$$\mathbf{k}_s = \mathbf{0}$$

$$\mathbf{f}_s = \mathbf{0}$$

where \mathbf{k}_s is the soil stiffness matrix; \mathbf{f}_s is the soil reaction forces vector; and u_n is the element node penetration in soil.

Step 4. Obtain the soil transformation matrix (\mathbf{R}_s) using Eq. (139). The first row of \mathbf{R}_s is the vector \mathbf{x}_s , the second row is the vector \mathbf{y}_s , and the third is \mathbf{z}_s ;

Step 5. Calculate the normal contact stiffness (k_n) and force (f_n):

$$k_n = \bar{k}_n \ell_c \quad \text{and} \quad f_n = k_n u_n \quad (141)$$

where \bar{k}_n is the normal soil stiffness per unit length; ℓ_c is the length of the element that is in contact with the soil.

Step 6. Calculate longitudinal and lateral forces and stiffness:

Step 6.1. From nodal displacements in global system ($\Delta \mathbf{u}$) obtain it in local coordinate system ($\Delta \mathbf{u}_s$):

$$\Delta \mathbf{u}_s = \mathbf{R}_s \Delta \mathbf{u} \quad (142)$$

Step 6.2. Calculate the elastic limit force (f_ℓ) and stiffness in each direction:

$$f_{\ell x} = \mu_x |f_n|, \quad f_{\ell y} = \mu_y |f_n|, \quad k_x = \frac{f_{\ell x}}{u_{\ell x}} \quad \text{and} \quad k_y = \frac{f_{\ell y}}{u_{\ell y}} \quad (143)$$

where $f_{\ell x}$ and $f_{\ell y}$ are the limit forces in the longitudinal and lateral directions, respectively; k_x and k_y are the contact stiffness in the longitudinal and lateral directions, respectively.

Step 6.3. Calculate the friction forces (f_x and f_y) in each direction using first Eq. (132);

Step 7. Assembly soil stiffness matrix and forces vector in the local system:

$$\mathbf{k}_{s\ell} = \begin{bmatrix} k_x & 0 & 0 \\ 0 & k_y & 0 \\ 0 & 0 & k_n \end{bmatrix} \quad \text{and} \quad \mathbf{f}_{s\ell} = \begin{bmatrix} f_x \\ f_y \\ f_n \end{bmatrix} \quad (144)$$

Step 8. Obtain stiffness matrix and forces vector in the global system by transferring them from local coordinate system:

$$\mathbf{k}_s = \mathbf{R}_s \mathbf{k}_{s\ell} \mathbf{R}_s^T \quad \text{and} \quad \mathbf{f}_s = \mathbf{R}_s^T \mathbf{f}_{s\ell} \quad (145)$$

6.

Numerical Tests

The multilayer pipe beam element formulation has been implemented in a computer program and a number of analyses were carried out to verify the element's performance in representing the behavior of risers in statics as well as in dynamics. Sample solutions considered were classified in three categories:

- a) Models with a single layer: for verification purpose only;
- b) Models with multiple layers: to provide insights into model capabilities, especially when considering simple examples;
- c) Applications of multilayer element simulations to actual riser structures, which provides some numerical comparisons to conventional solutions.

6.1.

Single Layer Models

6.1.1.

Cantilever Beam Subjected to Pure Bending

This example has been used by several authors [20 - 22, 36] to verify the numerical behavior of three-dimension beam elements, under severe geometric nonlinearities involving large displacements and rotations. A cantilever beam, initially straight under constant in-plane bending is considered in this example, as shown in Figure 20.

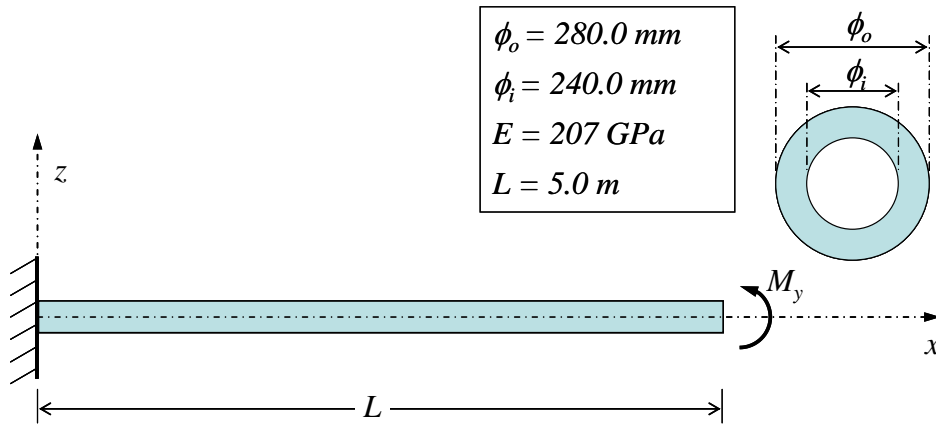


Figure 20: Cantilever Beam Under Pure Bending.

Analytical solutions as function of the applied load M_y and beam geometric and material parameters for rotation (θ), horizontal (u) and vertical (v) displacements, at the tip of the beam, is given as (Almeida et al. [36]):

$$\begin{aligned}\theta &= \frac{ML}{EI} \\ u &= L \left(\frac{\sin(\theta)}{\theta} - 1 \right) \\ w &= \frac{L}{\theta} (1 - \cos(\theta))\end{aligned}\tag{146}$$

Also, an analytical expression for the applied bending moment that curls the beam into a full circle is given by $M^* = \frac{2\pi EI}{L}$. In this analysis, the load is applied in ten equal increments with numerical convergence being achieved in up to eight iterations per increment. The beam is modeled considering a uniform mesh with five elements. Figure 21 shows some deformed configurations for the beam, at various load intensities.

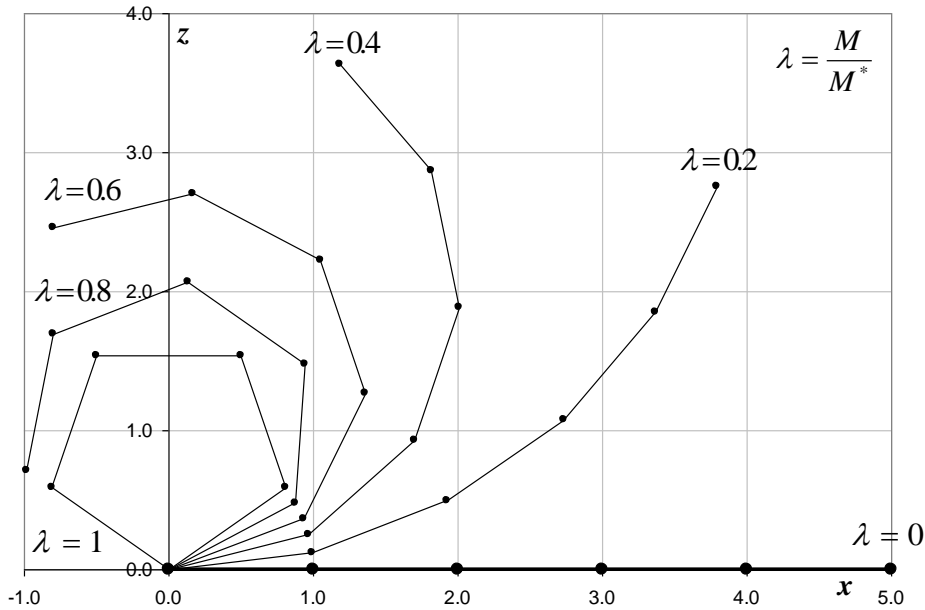


Figure 21: Cantilever Beam: Deformed Configurations.

Figure 22 presents a comparison of tip displacements numerically obtained results to the analytical solution provided in Eqs. (146). A good agreement between these in-plane results is reported.

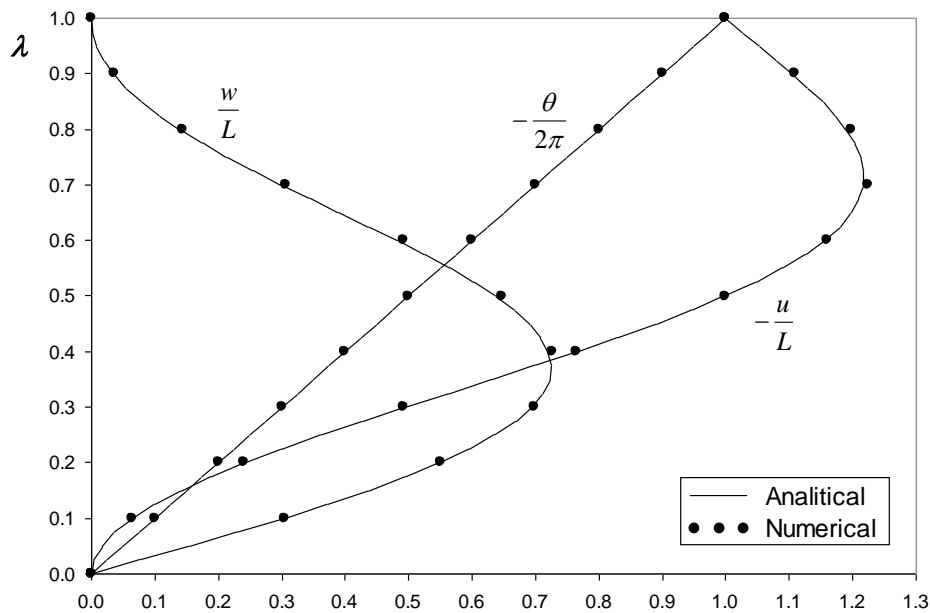


Figure 22: Normalized Displacements at Beam Tip.

6.1.2.

Composite Column Subjected to Eccentric Axial Loading

This example considers solutions for the buckling of a column in two eccentric segments, subjected to an axial eccentric load. Connection between the

two segments and the eccentric load are modeled using beam elements with high rigidity parameters. The objective of this analysis is to compare solutions for tip displacements and column configurations for various load intensities. The composite column was modeled using 22 finite elements, two representing the rigid connections at the middle and top of the column, and 10 equal beam elements for each segment. Column geometric and material details are shown in Figure 23 and the obtained numerical results for this model are presented in Figures 24 to 26. Compression loading was applied in 100 equal increments. Figure 24 presents deformed configurations of the column for different loading levels. From these results, bending moment distribution along the column was evaluated and compared to numerically obtained results for $P=0.2\text{kN}$, as shown in Figure 25. Figure 26 shows normalized displacements measured at applied load node. The results are in good agreement with the solutions presented by Nunes et al. [27] and Albino [28].

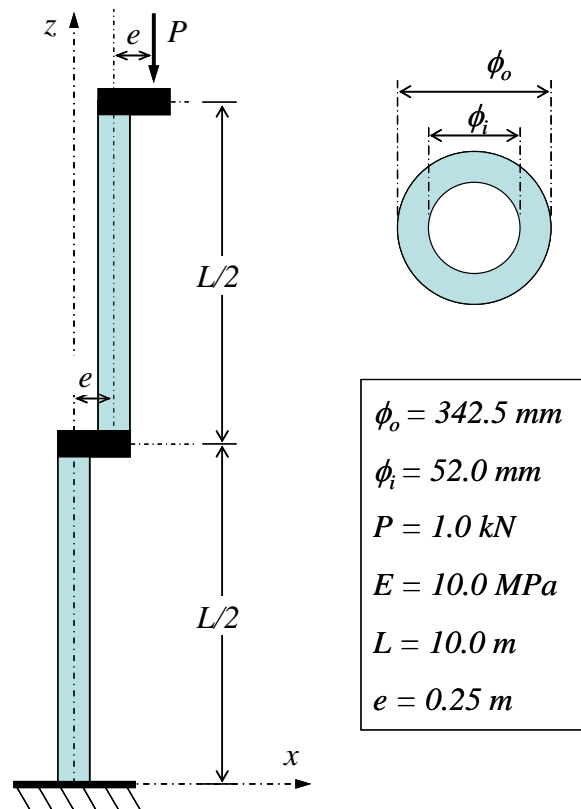


Figure 23: Composite Column Under to Eccentric Axial Load.

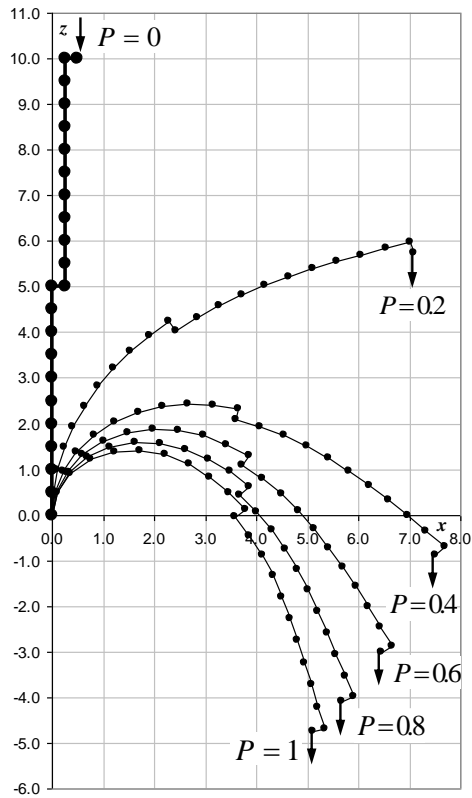


Figure 24: Composite Column: Deformed Configurations.

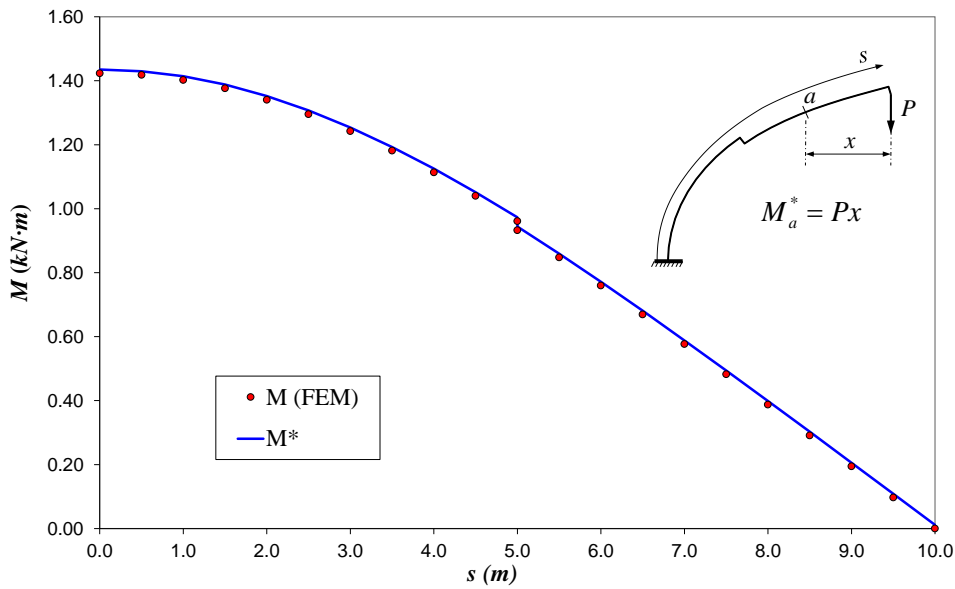


Figure 25: Bending Moment Along the Composite Column, for P=0.2 kN.

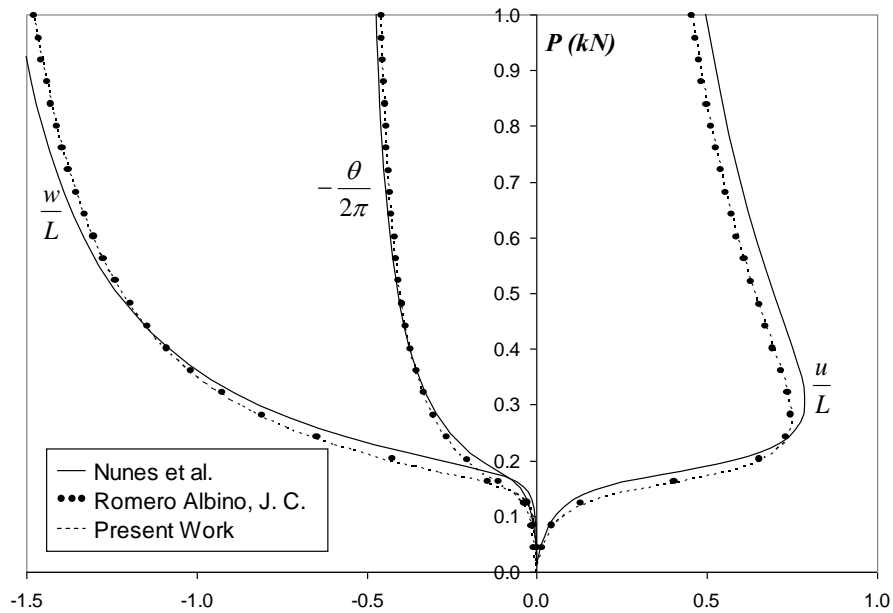


Figure 26: Normalized Displacement at the Top of the Composite Column.

6.1.3.

Out-of-Plane Loading to a Circular Cantilever Beam

This example has been considered by many authors such as Crisfield [21], Bathe and Bolourchi [22], Simo and Vu-Quoc [29] and Cardona and Geradin [30] in the evaluation of 3D general beams. It presents a useful testing to full 3D non-linear behavior of beam elements, including bending, torsion and transverse shear. The analysis consists of considering a curved pipe beam over 45 degrees, with 100in constant radius and under transverse loading, as shown in Figure 27. The beam is modeled using 8 equally spaced elements. In the analysis, the load factor (λ) considered varied from 0 to 7.2, in 20 equal increments.

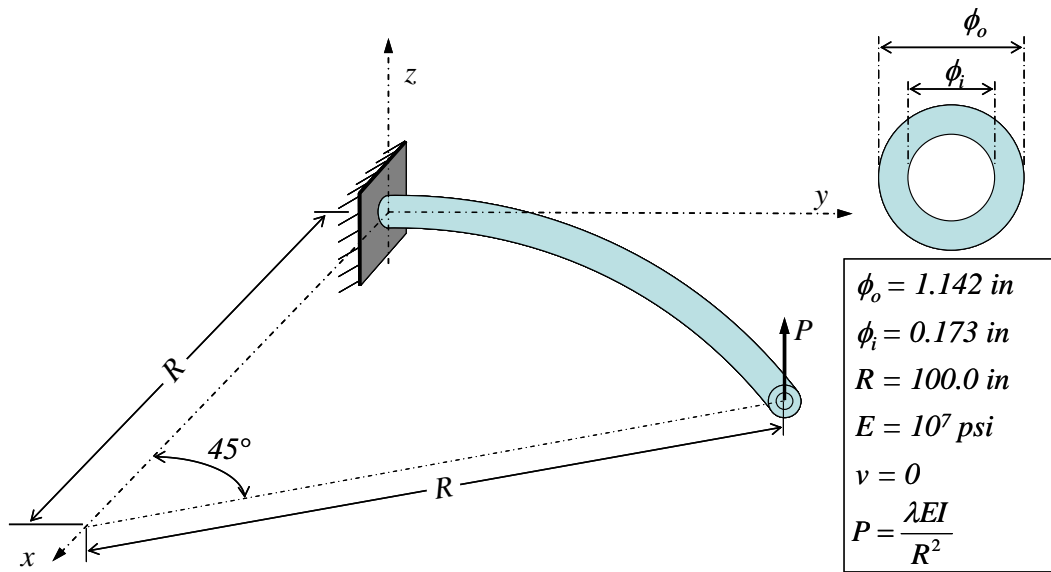


Figure 27: Circular Cantilever Beam Under Transverse Loading.

Numerical results for this analysis are shown in Figures 28 and 29. Figure 28 presents deformed configurations for three different loading levels, and Figure 29 shows displacements at the tip of the beam, which are compared to some other available results.

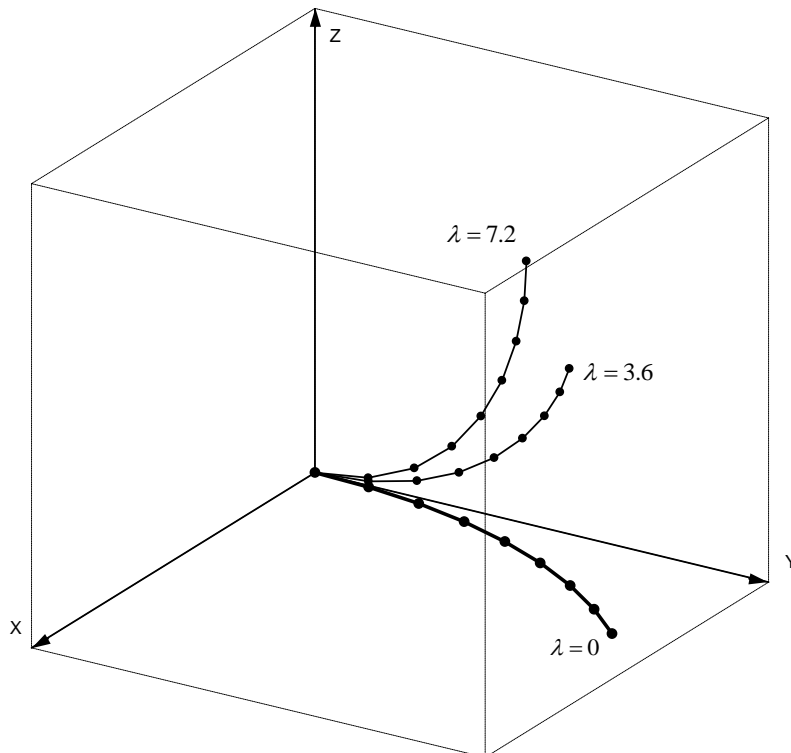


Figure 28: Circular Cantilever Beam: Deformed Configurations.

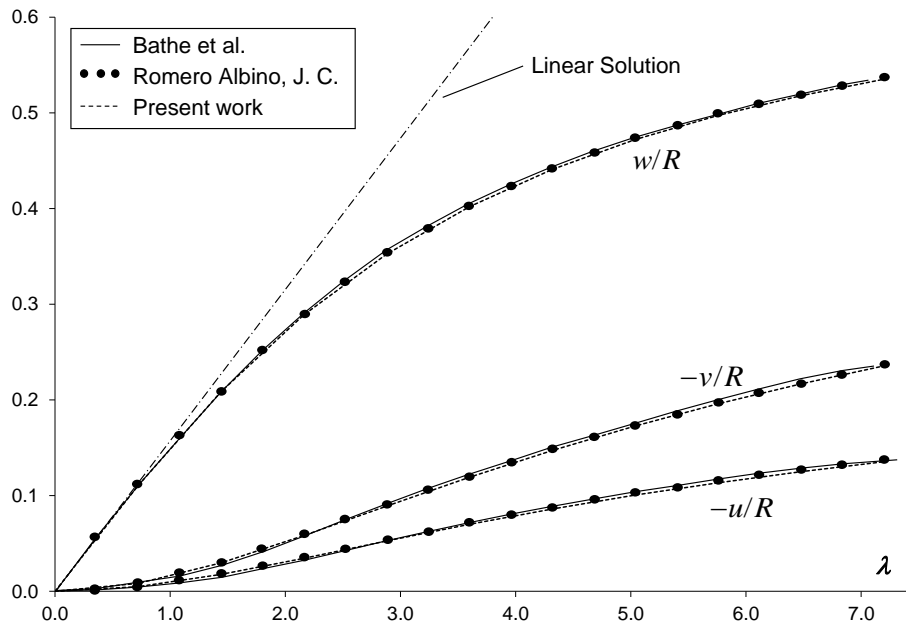


Figure 29: Normalized Displacements for the Circular Cantilever Beam.

Following Crisfield [21], we present a comparison of displacements at the free end of the beam in Table 3, including solutions from Albino et al. [36] and those obtained in this work. Small differences, lower than 2% in the numerical results, are observed.

Table 3: Comparison of Displacements at the Free End of the Beam.

| Author(s) | Tip position for each load level (initially at: 29.9, 70.71, 0.00) | | | | | | | | |
|--------------------------|--|-------|-------|-----------------|-------|-------|-----------------|-------|-------|
| | $\lambda = 3.6$ | | | $\lambda = 5.4$ | | | $\lambda = 7.2$ | | |
| | X | Y | Z | X | Y | Z | X | Y | Z |
| Present Work | 22.29 | 58.79 | 40.20 | 18.57 | 52.25 | 48.54 | 15.76 | 47.15 | 53.53 |
| Albino et al. [36] | 22.20 | 58.80 | 40.20 | - | - | - | 15.60 | 47.10 | 53.60 |
| Crisfield [21] | 22.16 | 58.53 | 40.53 | 18.43 | 51.93 | 48.79 | 15.61 | 46.84 | 53.71 |
| Bathe and Bolourchi [22] | 22.50 | 59.20 | 39.50 | - | - | - | 15.90 | 47.20 | 53.40 |
| Simo and Vu-Quoc [29] | 22.33 | 58.84 | 40.08 | 18.62 | 52.32 | 48.39 | 15.79 | 47.23 | 53.37 |
| Cardona and Geradin [30] | 22.14 | 58.64 | 40.35 | 18.38 | 52.11 | 48.59 | 15.55 | 47.04 | 53.50 |

6.1.4.

Towing of a Pipeline in Contact With the Seabed

The objective of this example is to verify the capabilities of the pipe-soil interaction models presented in section 5. The model consists of a 350m long pipeline being towed 300m, in the lateral direction, in contact with an irregular seabed, as shown in Fig. 30. The pipeline is attached to two towing boats with two cables with varying length (80m to 128m), so that the pipe can be lowered to get in contact with the seabed during the simulation.

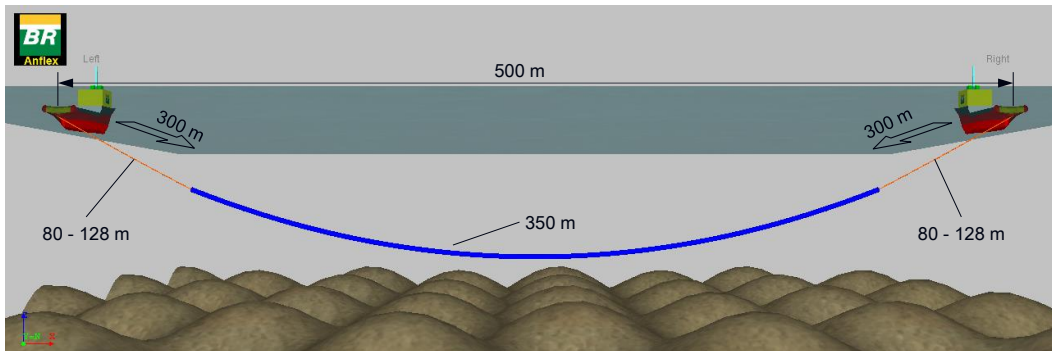


Figure 30: Towing of a Pipeline.

The pipe was modeled with a uniform mesh of 100 elements with the geometrical and material properties presented in Table 4. The soil properties used to represent the contact between the pipeline and the seabed is presented in Table 5.

Table 4: Towed pipeline properties.

| | |
|--------------------------------------|----------|
| External diameter (m) | 0.26 |
| Internal diameter (m) | 0.20 |
| Young modulus (kN/m ²) | 1.44E+05 |
| Specific weight (kN/m ³) | 26.86 |

Table 5: Soil properties for towed pipeline.

| | |
|---|-----------|
| Longitudinal friction coef. - μ_x | 0.3 |
| Lateral friction coef. de - μ_y | 0.5 |
| Longit. elastic limit - u_{lx} (m) | 0.03 |
| Lateral elastic limit - u_{ly} (m) | 0.26 |
| Normal stiffness - k_n (kN/m ²) | 100 |
| Friction model | uncoupled |

The analysis considers an irregular seabed with the geometry defined by Eq. (147).

$$z(x, y) = a(\sin(bx + cy) + \cos(cx - by)), \text{ with } a = 8m \text{ and } b = c = 0.04m \quad (147)$$

The towing process was simulated in an incremental static analysis with 110 steps. The first 10 increments were used to lay down the pipeline on the irregular seabed. The displacements of the towing boats were applied in the following 100 increments. Figure 31 shows a sequence of snapshots of the deformed

configuration of the pipeline during the towing simulation. It is possible to observe that the pipeline accommodates to the seabed geometry. This shows the robustness of this simple model to represent such a complex problem.

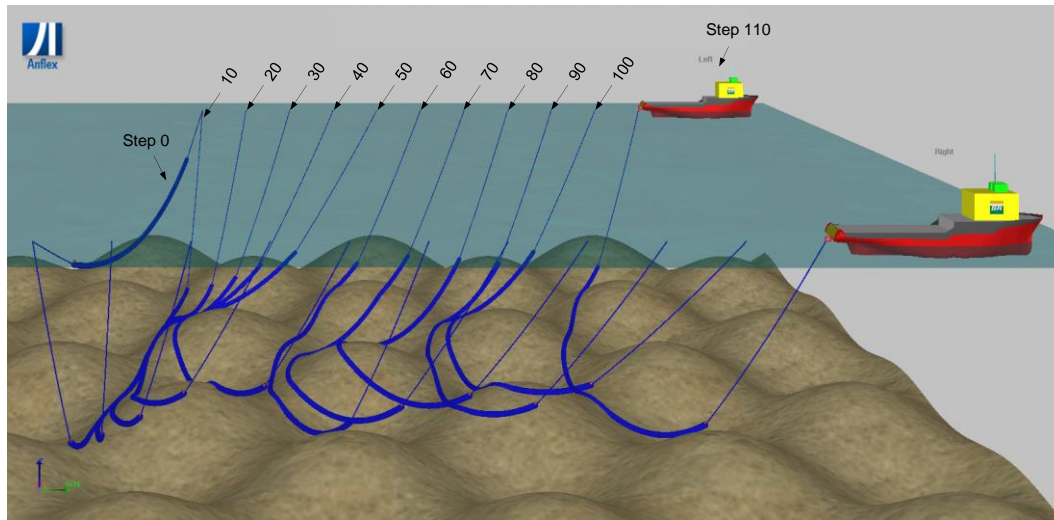


Figure 31: Deformed Configuration of the Towed Pipeline.

6.2.

Multilayered Beam Models

6.2.1.

Two Layer Pipe Beam Subjected to Axial Loading

A two layer straight beam, restrained at one end at inner layer is loaded by an axial force F , applied at the free end of outer layer was considered in this example. The beam was modeled with a finite element mesh containing 15 uniform elements, using the material and cross section geometrical properties presented in Figure 32. The Young modulus for each layer is set so that both layers would have the same axial stiffness, i.e. $E_{int}A_{int} = E_oA_o$. Thus, the interlayer shear stress distributions along the beam are symmetric with respect to the beam mid-section.

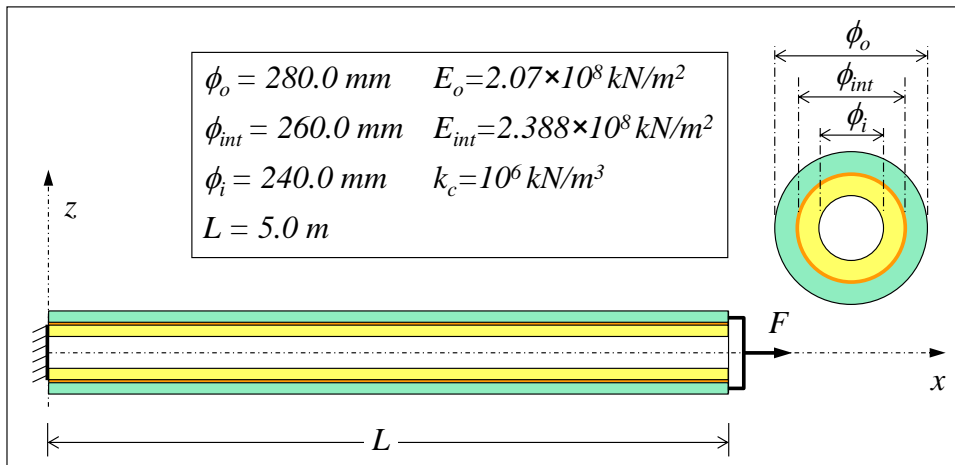


Figure 32: Two Layer Pipe Beam Under Axial Loading

Linear Elastic Slip:

In this analysis a linear elastic slip model is considered and an axial force $F = 1000 \text{ kN}$ is applied. Figures 33 and 34 show obtained numerical results for the axial displacements and contact stresses at the interface between layers, respectively, as compared to analytical solution proposed by Aguiar and Almeida [18] which is presented in Appendix A.1. A good agreement between numerical and analytical solution results is observed.

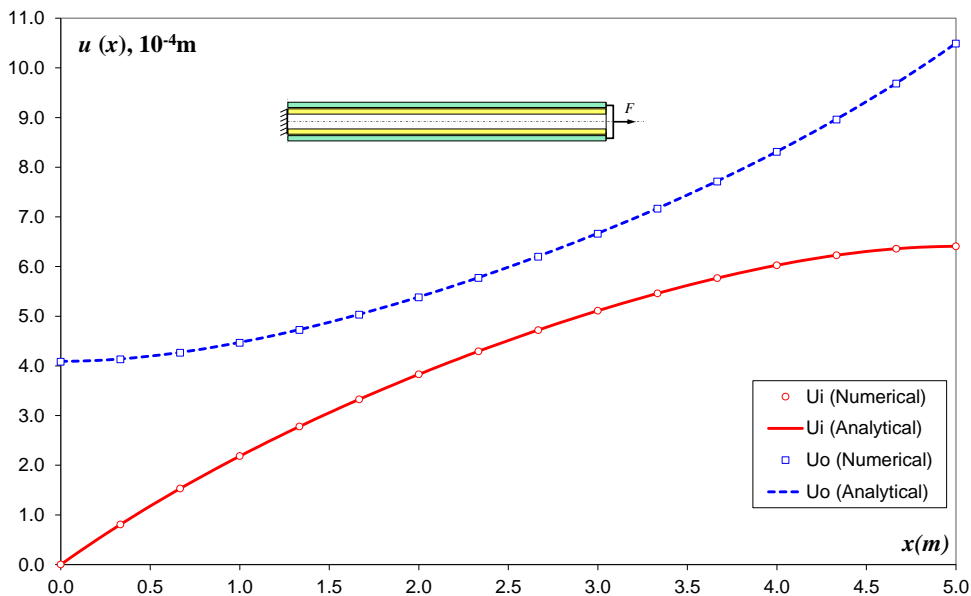


Figure 33: Axial displacements – Linear Elastic Slip.

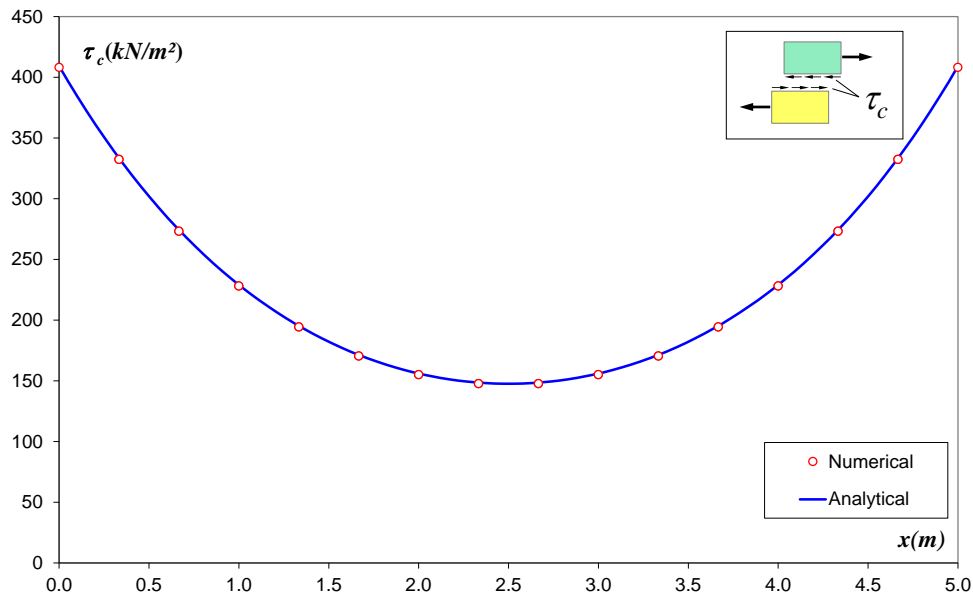


Figure 34: Longitudinal Contact Stresses at the Interface – Linear Elastic Slip.

Slip With Static Friction:

In this analysis a slip model with contact stiffness $k_c = 10^6 \text{ kN/m}^3$ and limit contact stress $\tau_\ell = 200.0 \text{ kN/m}^2$, using a bi-linear slip model, is considered. The objective of this analysis is to compare the numerical results with the corresponding theoretical limit value for axial load which is given by $F_\ell = 2\pi r_{int} L \tau_\ell = 879.65 \text{ kN}$. The total loading was applied in 45 equal steps, starting at 490.0 kN , which corresponds to the elastic slip limit, approximately. The contact stress distribution along the beam, for some load levels, is presented in Figure 35. From these results it is possible to notice the adhesive material rupture propagation, starting from both ends of the beam and preserving symmetry. Figure 36 shows the resulting residual contact stresses obtained after load $F = 0.95 F_\ell$ has been applied and then removed. The nonlinear nature of the numerical response can also be observed in the load-end displacement plots for both layers, as presented in Figures 37 and 38.

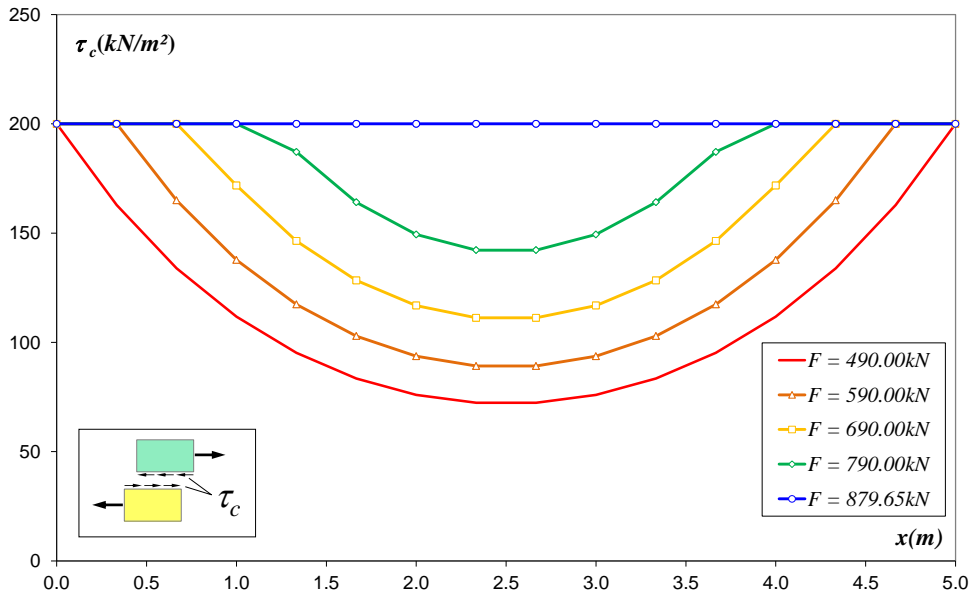


Figure 35: Contact Stresses at Interface – Slip with Static Friction.

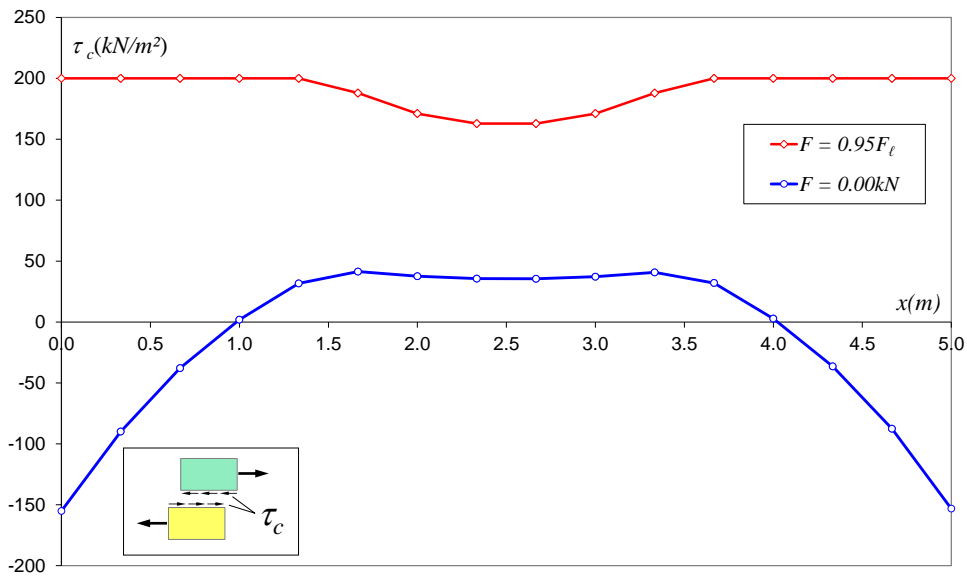


Figure 36: Residual Contact Stresses at Interface After Unloading – Slip With Static Friction.

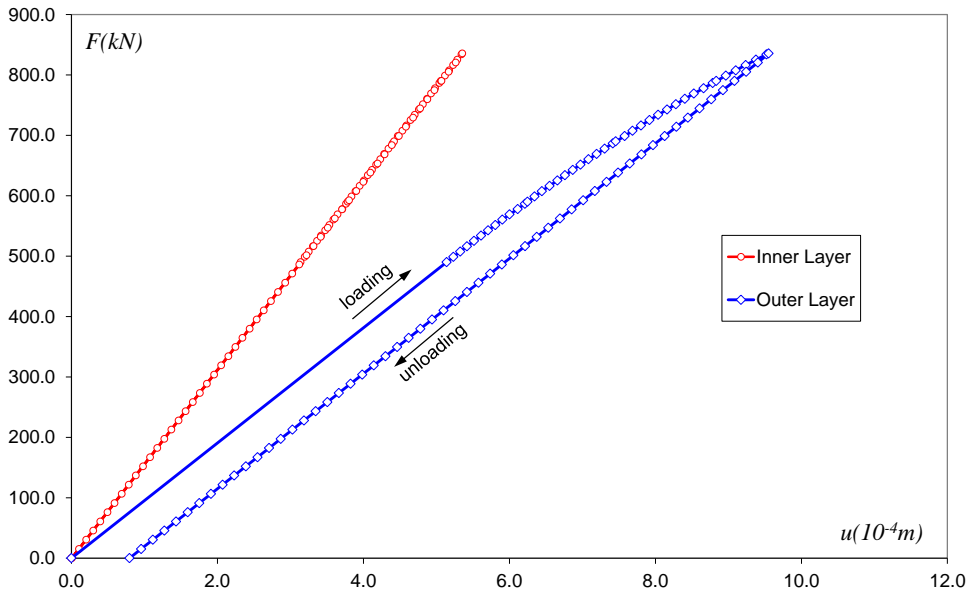


Figure 37: Applied Load vs. Axial Displacements at the Free End of Each Layer - Slip With Static Friction.

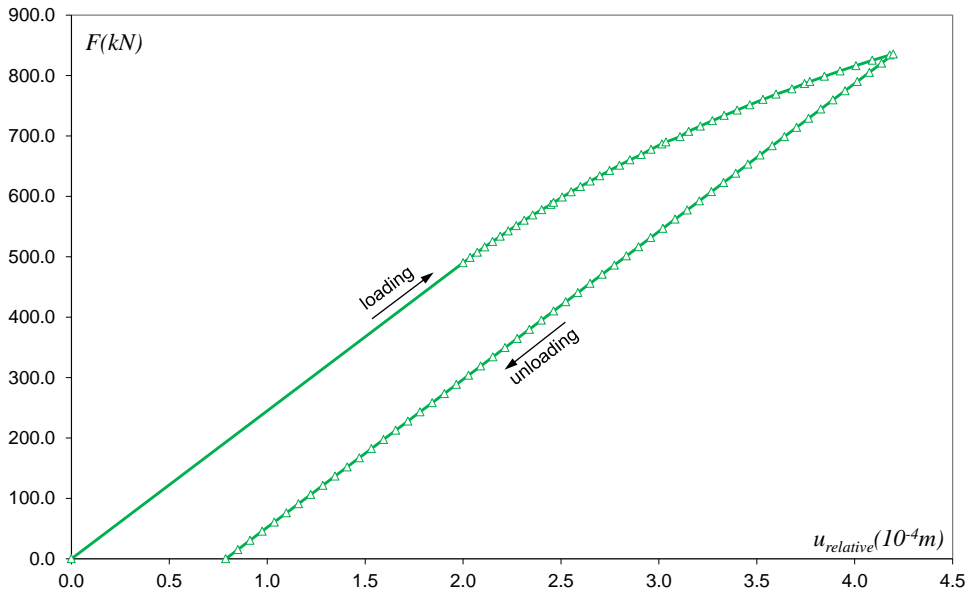


Figure 38: Applied Load vs. Relative Axial Displacement at the Beam Tip - Slip with Static Friction.

PUC-Rio - Certificação Digital N° 09125660/CB

6.2.2.

Two-Layer Cantilever Beam

The behavior of a two layer cantilever pipe beam under pure bending loading is investigated, as shown in Figure 39. Interlayer contact conditions are considered in the analysis with stiffness of $k_c = 10^6 \text{ kN/m}^3$. A bending moment was progressively applied, at the free end inner layer, up to $M_y = \frac{2\pi(EI)_{eq}}{L}$, in ten equal loading increments. This bending moment is the required load to curl the

beam into a complete circle. The parameter $(EI)_{eq}$ is the equivalent homogeneous beam bending stiffness, obtained from adding the inner and outer layer bending stiffness, i.e.: $(EI)_{eq} = E_i I_i + E_o I_o$.

Considering a perfect binding condition between layers, one obtains the analytical stress distribution along the pipe thickness from the expression:

$$\sigma_k = \frac{E_k M_y z}{(EI)_{eq}} \tag{148}$$

where k is layer index.

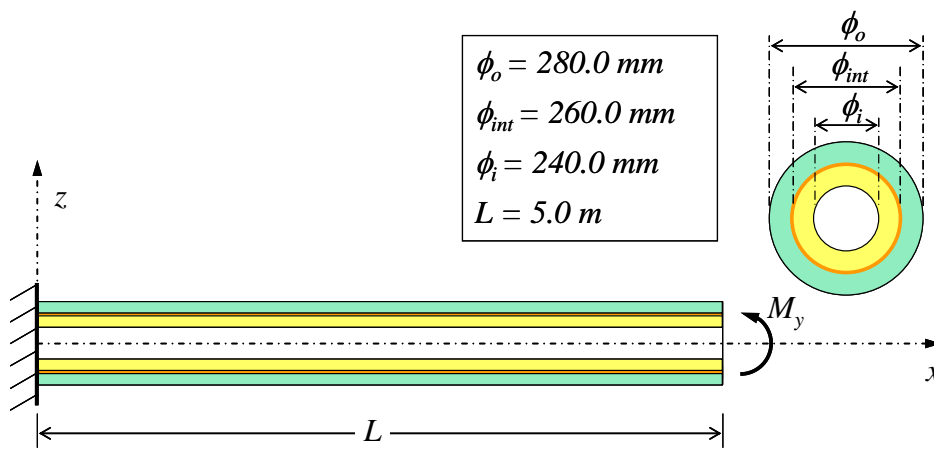


Figure 39: Two-Layer Cantilever Beam.

Figure 40 shows the bending moment distribution along each element layer considering the same material for both layers ($E_i = E_o = 200GPa$).

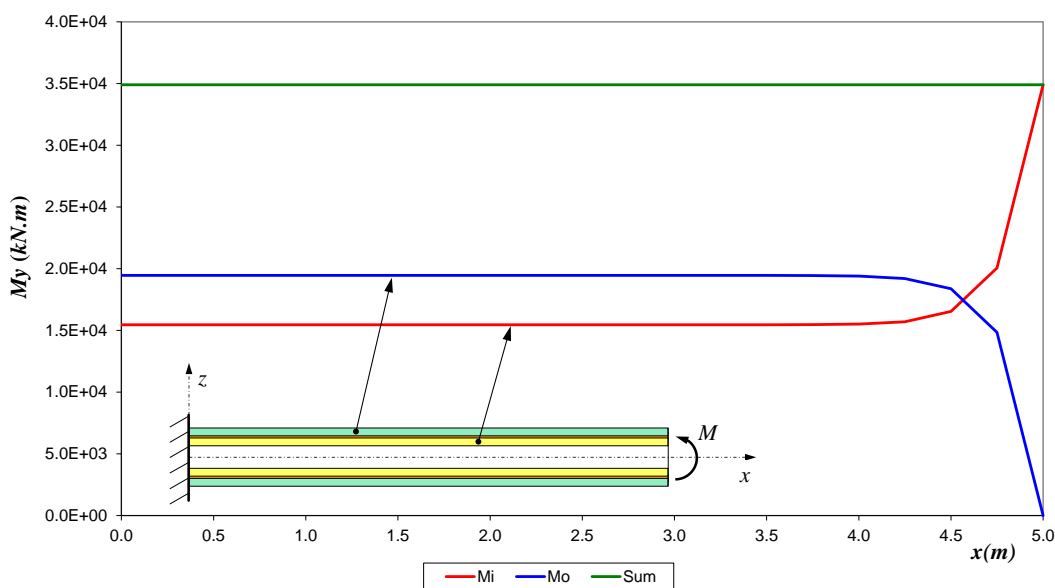


Figure 40: Bending Moment at Each Element Layer (One Material).

Considering the cross section in the middle of the beam, where pure bending is observed for each layer, one observes that the normal stress distribution along the pipe wall is linear, as shown in Figure 41. This figure also shows a good agreement between the exact solution for perfectly bonded beams, given by Eq. (148), and the stresses obtained from numerical bending moments at each layer.

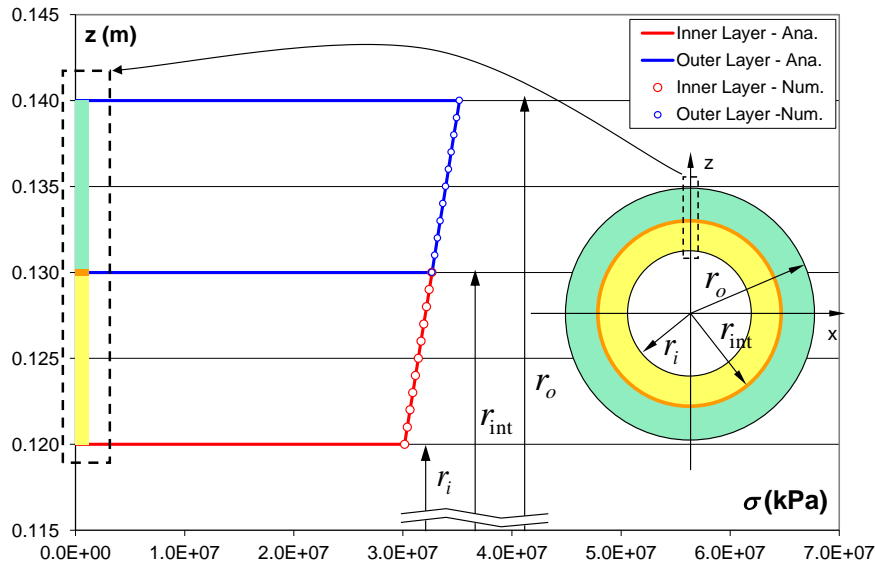


Figure 41: Axial Stress Distribution at Mid-Length Cross Section (One Material).

If different materials are considered at each layer ($E_i = 2E_o = 200GPa$), bending moment distributions along the beam is as shown in Figure 42.

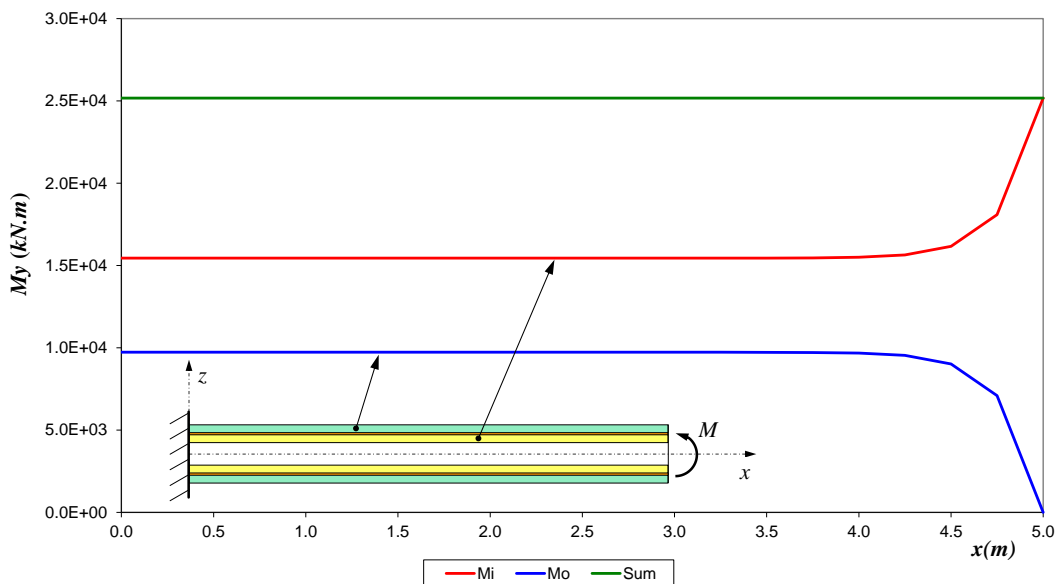


Figure 42: Bending Moment at Each Element Layer (Layers with Different Materials).

In this case, discontinuous normal stress distributions are observed in the mid-length cross section, as shown in Figure 43.

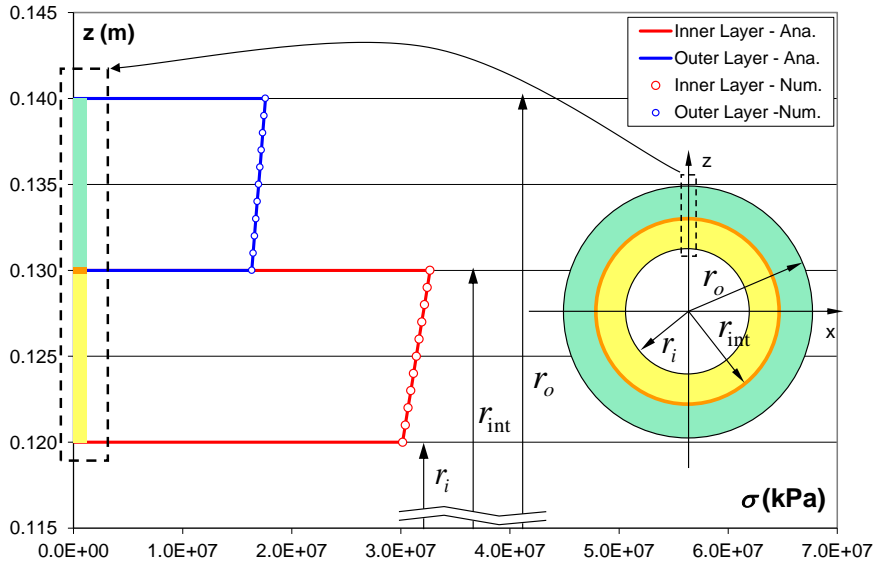


Figure 43: Axial Stress Distribution at Mid-Length Cross Section (Different Materials).

Figure 44 shows that displacement compatibility at both layers is well represented by the analysis results, as displacements at the tip of the beam are the same for both layers. Good agreement between numerical and analytical solutions is observed.

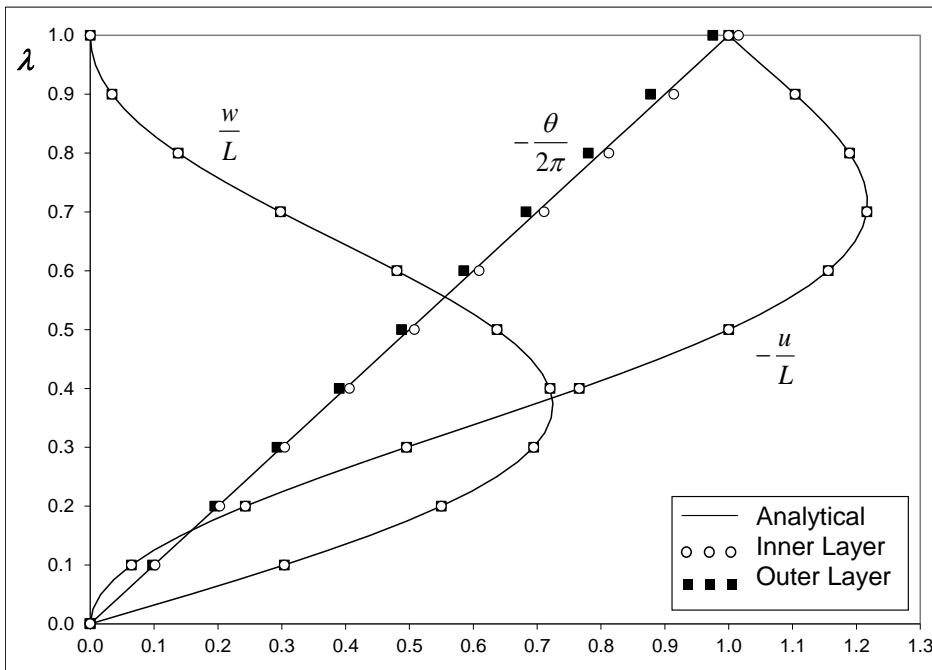


Figure 44: Normalized Displacements at the Two-Layer Cantilever Beam Tip.

6.2.3.

Two-Layer Cantilever Beam Submitted to Distributed Loading

The objective of this analysis is to test the multilayered pipe beam element under large displacement in static and dynamic loadings. The original model was originally proposed by Bathe and Bolourchi [22] for the representation of 3D beams in large displacement analysis. In this analysis a two-layer cantilever pipe beam under a uniformly distributed load was considered, as shown in Figure 45. The beam is modeled using 8 equally spaced elements with the load applied in the internal layer nodes, as in a pipe with internal fluid.

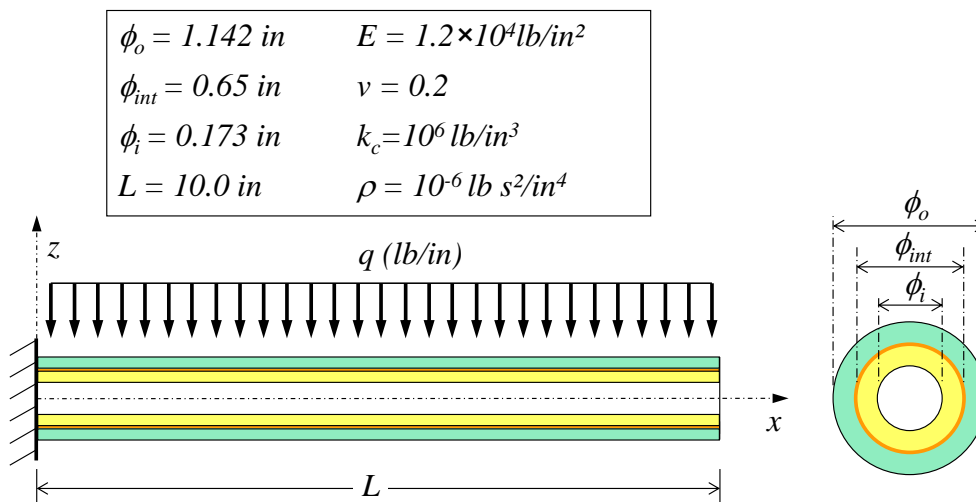


Figure 45: Properties for the Two-Layer Cantilever Beam Under Distributed Loading.

Static solution for the vertical displacement at the beam tip was obtained with applied load in 20 equal increments. As shown in Figure 46, numerically obtained results are in good agreement with the solution given in Bathe and Bolourchi [22]. Since a very high interlayer contact stiffness (k_c) was considered, vertical movements for both layers are equal, and thus, only inner layer movements are presented in Figure 46.

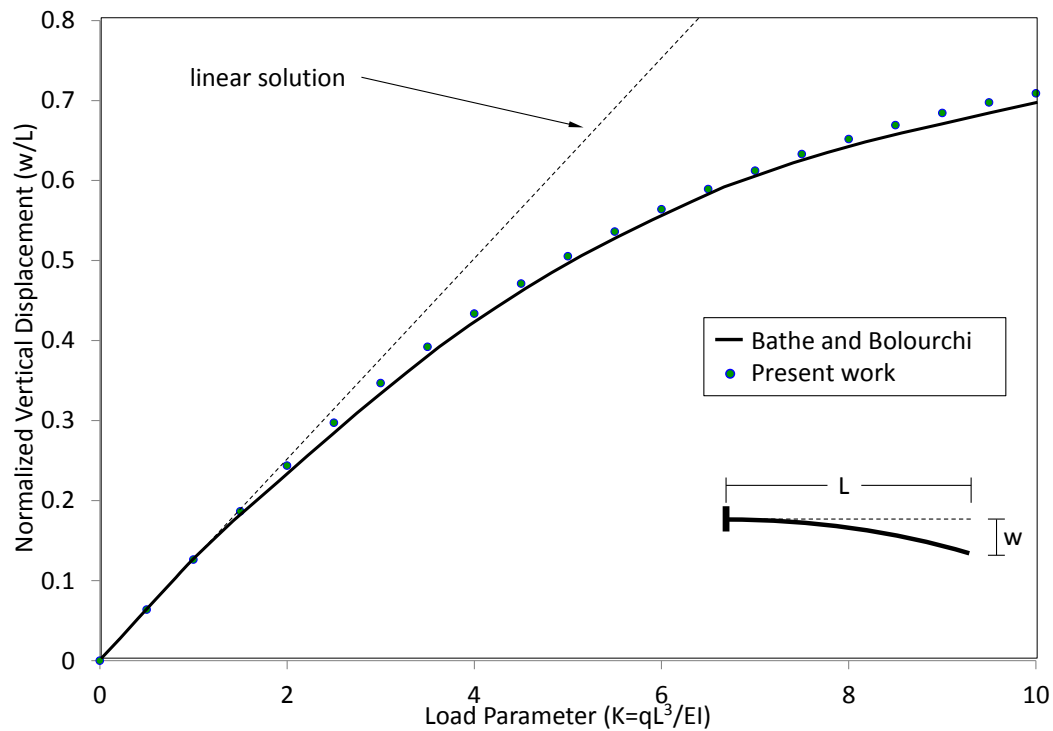


Figure 46: Beam Tip Displacements – Static Analysis

The dynamic analysis was performed with a step uniform load $q = 2.85 \text{ lb/in}$. A total time analysis of $1.215 \times 10^{-2} \text{ s}$ was used, with time increments of $\Delta t = 1.35 \times 10^{-4} \text{ s}$. The dynamic response for vertical displacements at the tip of the beam inner layer is presented in Figure 47, obtained using the HHT time integration algorithm along with the Newton-Raphson iterative scheme. As shown, the dynamic response presented in Bathe and Bolourchi [22] presents some damping effects, without any further information provided. Thus, considering a damping coefficient equals to 1.0%, proportional to the element stiffness, as in the Rayleigh proportional damping described by Mourelle [20], the model analysis provides a better agreement for the beam transverse amplitude results with a very good agreement in period, as shown in the results presented in Figure 47.

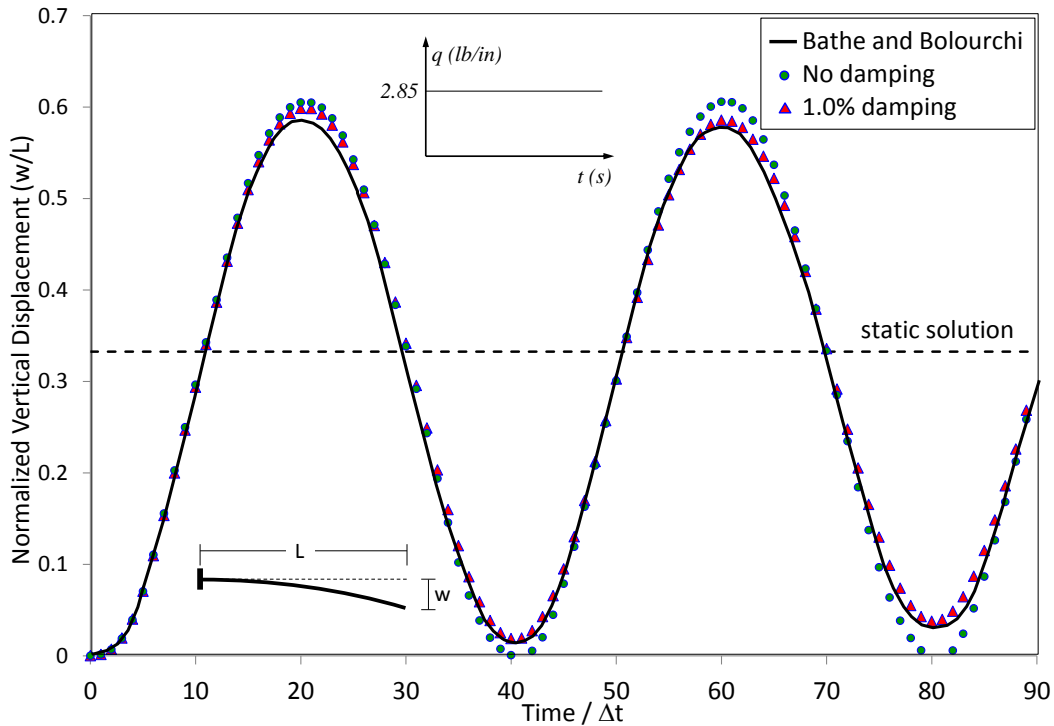


Figure 47: Beam Tip Displacements – Dynamic Analysis

6.2.4.

Dynamic Analysis of a Circular Two-Layer Cantilever Beam

In this analysis, the circular cantilever beam presented in section 6.1.3 for static analysis, is studied in dynamics with a two-layer cross section. Beam's geometrical and material properties are shown in Figure 48. The numerical analysis intends to evaluate the performance of the multilayered element in 3D large displacement dynamic analysis. This model was analyzed under dynamic loading by Chan [38], using the conventional homogeneous pipe beam formulation. Obtained tip displacements deflections, resulting from a suddenly applied load equal to $300lb$ are plotted in Figure 49 for a total time of $0.3s$, with a time increment $\Delta t = 0.002s$ used. Figure 49 shows a good agreement between the two-layered pipe beam displacement results and the ones obtained by Chan [38].

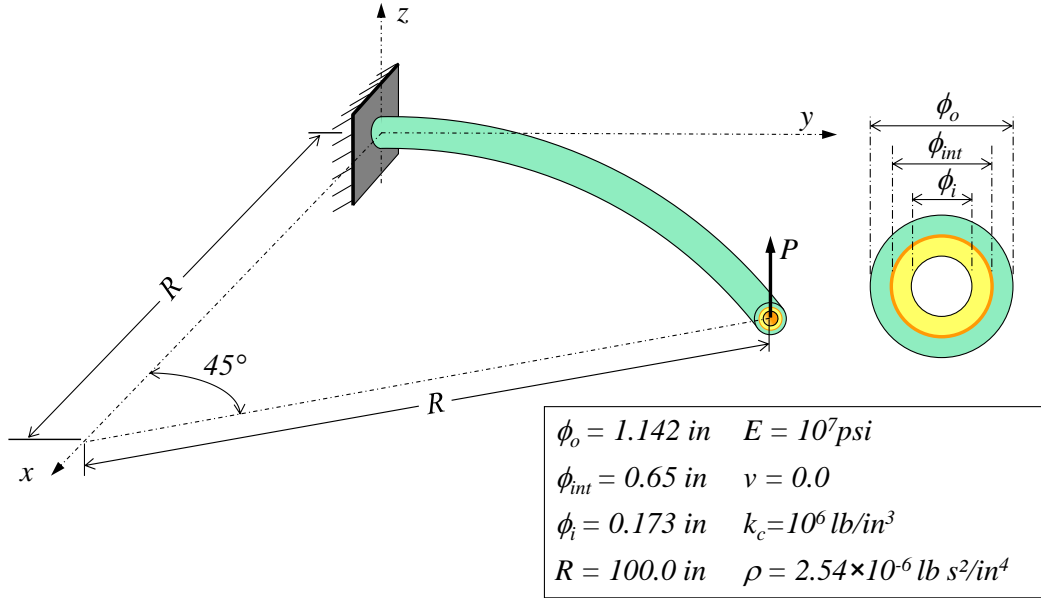


Figure 48: Geometrical and Material Properties for the Circular Two-Layer Cantilever Beam.

PUC-Rio - Certificação Digital N° 0912560/CB

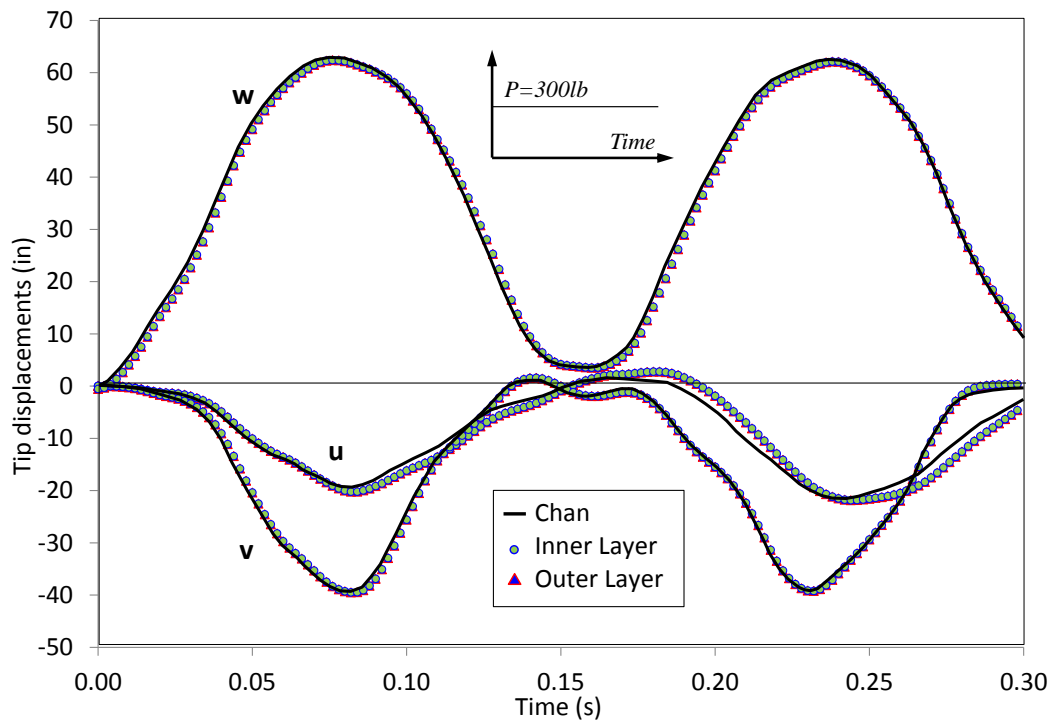


Figure 49: Circular Cantilever Beam Tip Displacements in Dynamics Analysis.

6.2.5.

Two-Layer Cantilever Under Hydrostatic and Hydrodynamic Loading

A two-layer submerged capped ends cantilever pipe, under vertical concentrated load at the free end is considered. The objective of this analysis is to

verify the behavior of the multilayer pipe beam element under gravity loading combined with external and buoyancy loads. This study was carried out by Yazdchi and Crisfield [40] using a 2D pipe beam formulation in static analysis. The material and geometrical properties are shown in Figure 50.

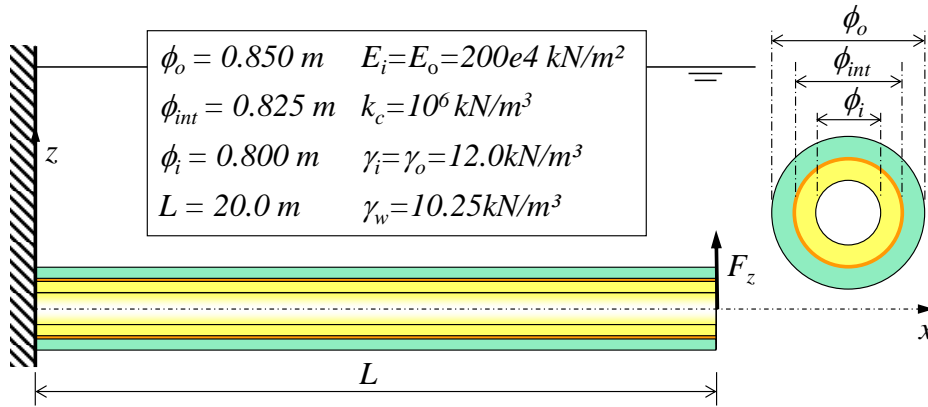


Figure 50: Submerged Cantilever Beam.

The beam was represented using a 20 equal element model under concentrate loadings applied to the internal layer node. Static deformed configurations obtained for four loading conditions are shown in Figure 51, which are in very good agreement with the ones presented by Yazdchi and Crisfield [40]. In dynamic analysis, a total time of 30s was considered for a constant time increment of 0.1s. In the numerical analysis an upward load was statically applied to the submerged beam and suddenly removed. Results for vertical displacements at the beam tip are shown in Figure 52, where hydrodynamic damping effects are noticeable. As shown, obtained results compared to the conventional homogeneous beam solution are good agreement.

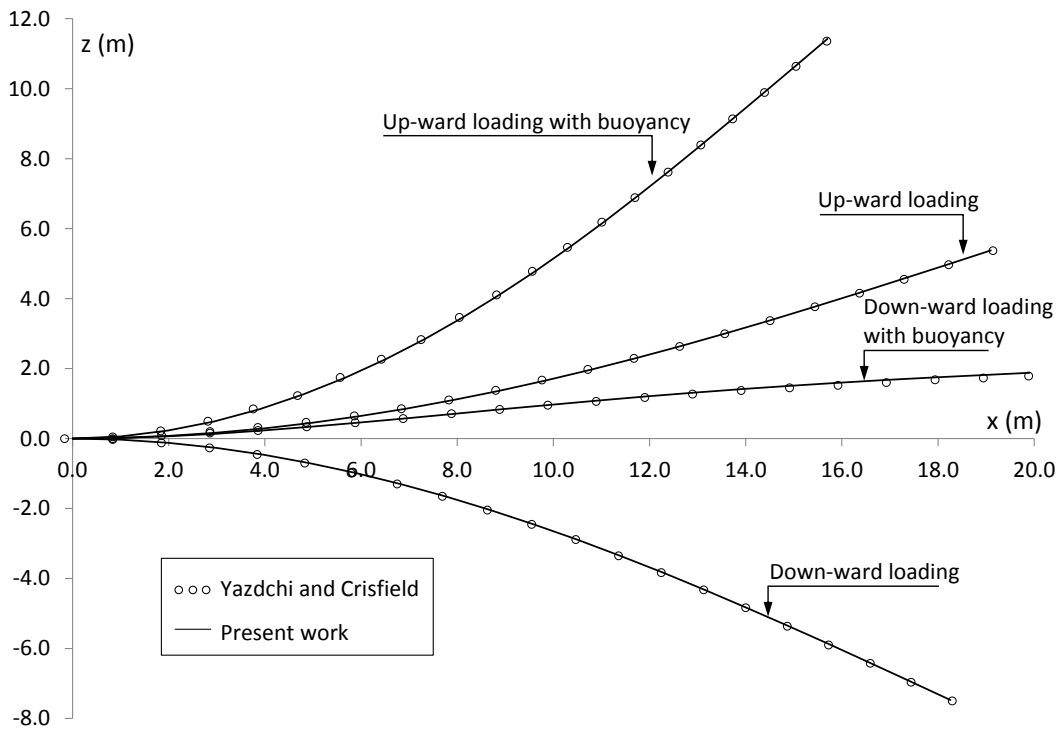


Figure 51: Deformed Shapes for Various Loading Conditions.

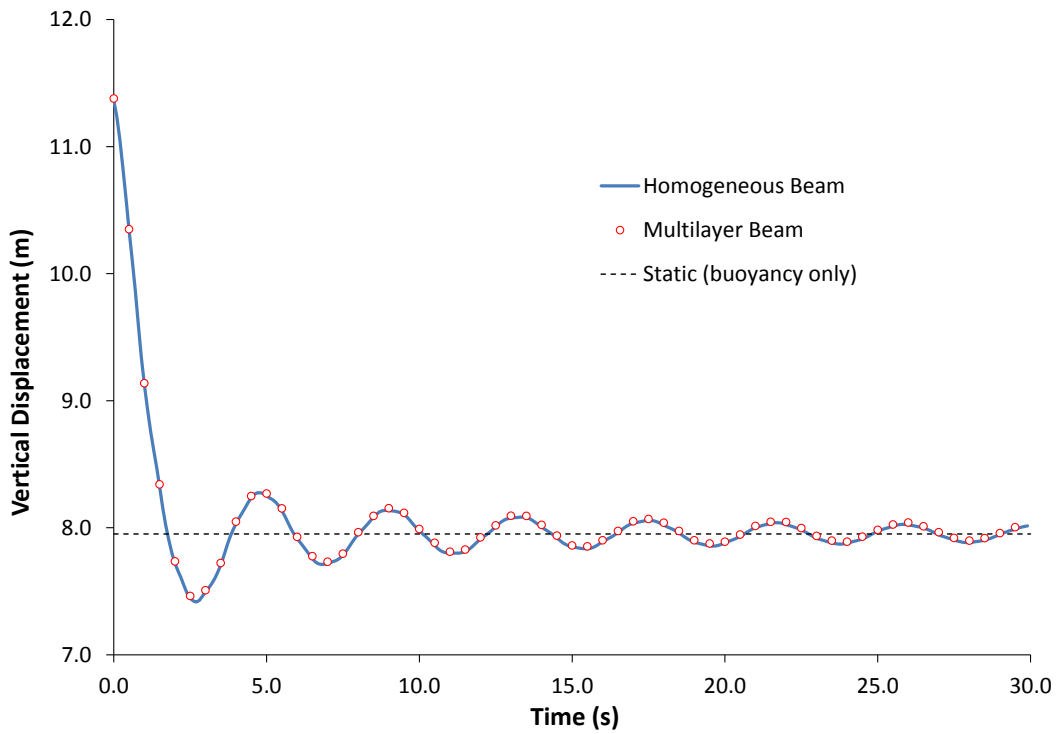


Figure 52: Vertical Displacements at Beam Tip.

6.3.

Multilayered Riser Analysis

6.3.1.

Flexible Riser in Catenary Configuration

In this example a 350.0m long flexible catenary riser is considered. In the set up, the riser is connected, at the top, to a floating unit and at the bottom to a sub-sea tower, at a water depth of 150.0m, which is horizontally displaced 150.0m from the top connection. The riser is assumed to be full of seawater. A finite element mesh employed 16 equal 20.0m elements, two 10.0m elements and two 5.0m long elements. Geometric, material and hydrodynamic properties used in the model, as well as details of the finite element mesh used, are shown in Figure 53. The same riser system has already been analyzed in various publications (McNamara et al. [41], Yazdchi and Crisfield [42], Kordkheili et al. [43]).

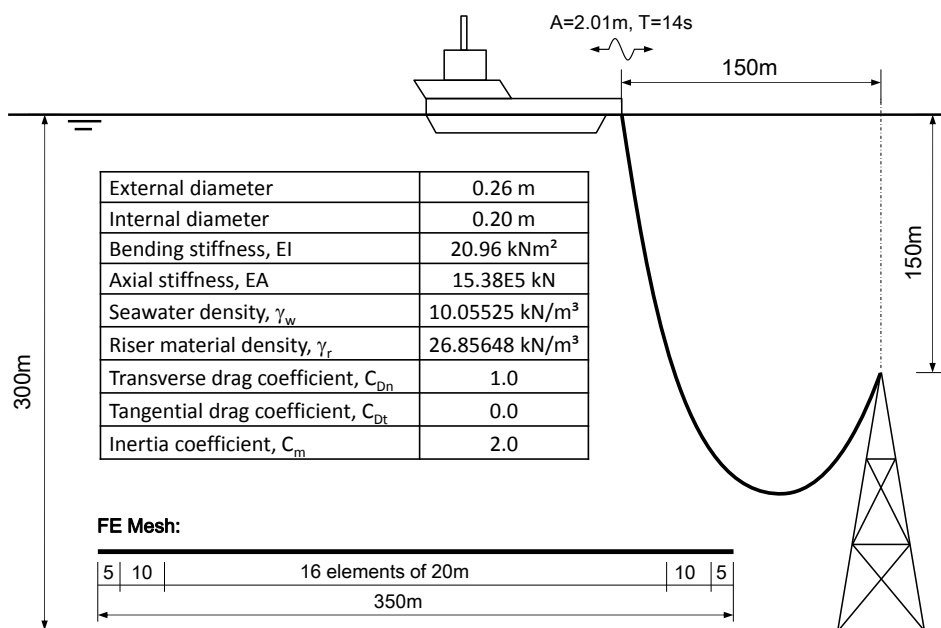
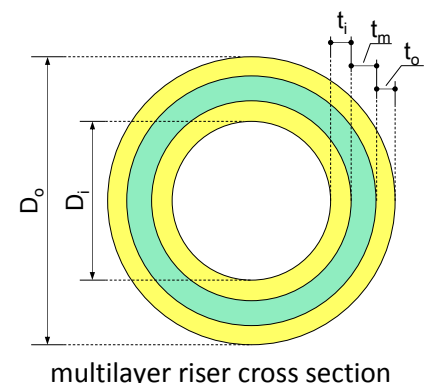


Figure 53: Flexible Riser in Catenary Configuration.

The riser was modeled with three layers with the properties shown in Table 6. A flexible riser is a composite construction of interlocked steel and polymeric layers designed to give the structure an axial stiffness approximately five orders of magnitude greater than the bending stiffness. Thus, to reproduce the stiffness properties presented in Figure 53, the numerical model was modified to consider a stiffening factor (EA/EI) in all layers.

Table 6: Multilayer Riser Properties.

| | | |
|-----------------------------------|----------------------------|--|
| Internal diameter, D_i | 0.20 m |  <p style="text-align: center;">multilayer riser cross section</p> |
| External diameter, D_o | 0.26 m | |
| Inner layer thickness, t_i | 0.003 m | |
| Middle layer thickness, t_m | 0.024 m | |
| Outer layer thickness, t_o | 0.003 m | |
| Inner layer Young modulus, E_i | 6.76E+05 kN/m ² | |
| Middle layer Young modulus, E_m | 6.76E+03 kN/m ² | |
| Outer layer Young modulus, E_o | 6.76E+05 kN/m ² | |
| Inner layer density, γ_i | 129.12 kN/m ³ | |
| Middle layer density, γ_m | 1.2912 kN/m ³ | |
| Outer layer density, γ_o | 129.12 kN/m ³ | |
| Stiffening factor, (EA/EI) | 7.3378E+04 | |
| Contact stiffness, k_c | 1.0E+06 kN/m ³ | |

A static analysis has been carried out considering self-weight and buoyancy forces only. Horizontal and vertical reactions at the support points are listed in Table 7. The good agreement with the given by McNamara et al. [41] and Yazdchi and Crisfield [42] verifies the accuracy of the multilayered element.

Table 7: Support Reactions at Top and Bottom Connections.

| Reference | V_{bottom} | V_{top} | H_{bottom} | H_{top} | |
|------------------|---------------------|------------------|---------------------|------------------|--------------|
| McNamara (FEM) | 35.83 | 91.45 | 11.92 | 11.57 | |
| McNamara (cable) | 35.77 | 91.51 | 12.02 | 12.02 | |
| Crisfield et al. | 35.86 | 91.61 | 12.04 | 12.04 | |
| Present work | inner | 12.60 | 30.34 | 3.85 | 3.83 |
| | middle | 1.36 | 3.45 | 0.45 | 0.45 |
| | outer | 21.88 | 57.84 | 7.72 | 7.74 |
| | sum | 35.84 | 91.63 | 12.02 | 12.02 |

The bending moment diagram along the riser is shown in Figure 54 and it is consistent with the ones obtained by McNamara et al. [41], Yazdchi and Crisfield [42] and Kordkheili et al. [43].

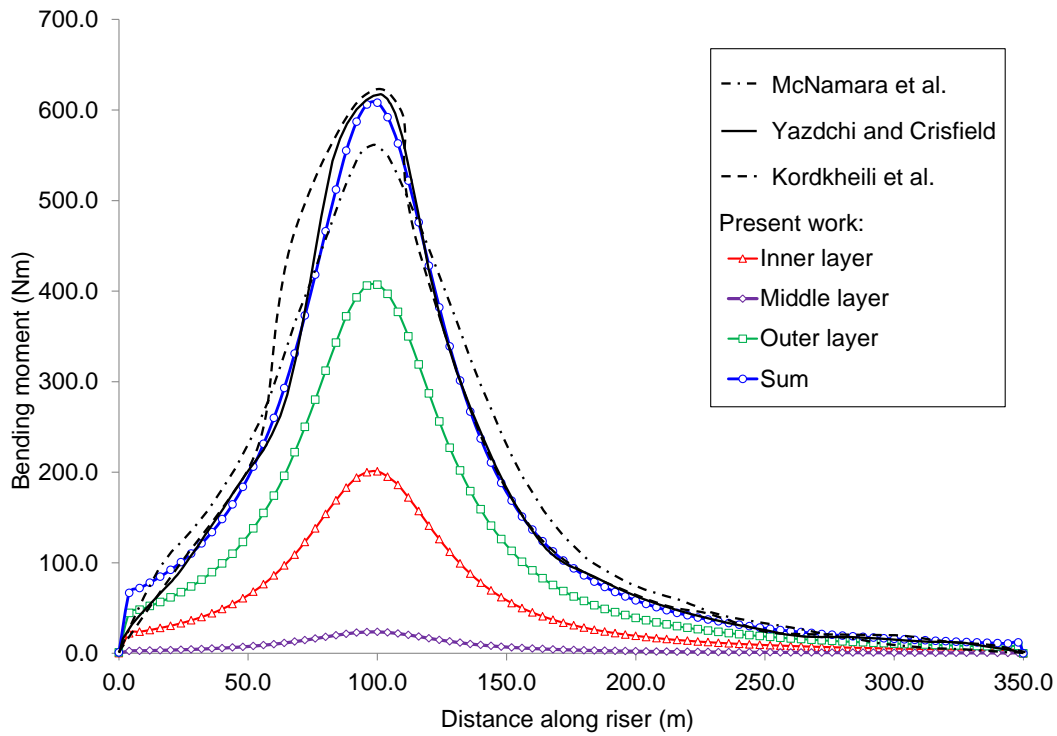


Figure 54: Bending Moment Distribution Along Multilayered Riser.

The riser was also analyzed dynamically with prescribed displacement at the top node due to ship movement. A horizontal harmonic excitation with amplitude of 2.01m and a corresponding period of 14.0s was considered. The results of this analysis are shown in Figure 55 and compared to the solution obtained by Yazdchi and Crisfield [42]. Both the top and bottom nodes vertical reaction are in good agreement with Crisfield's solutions.

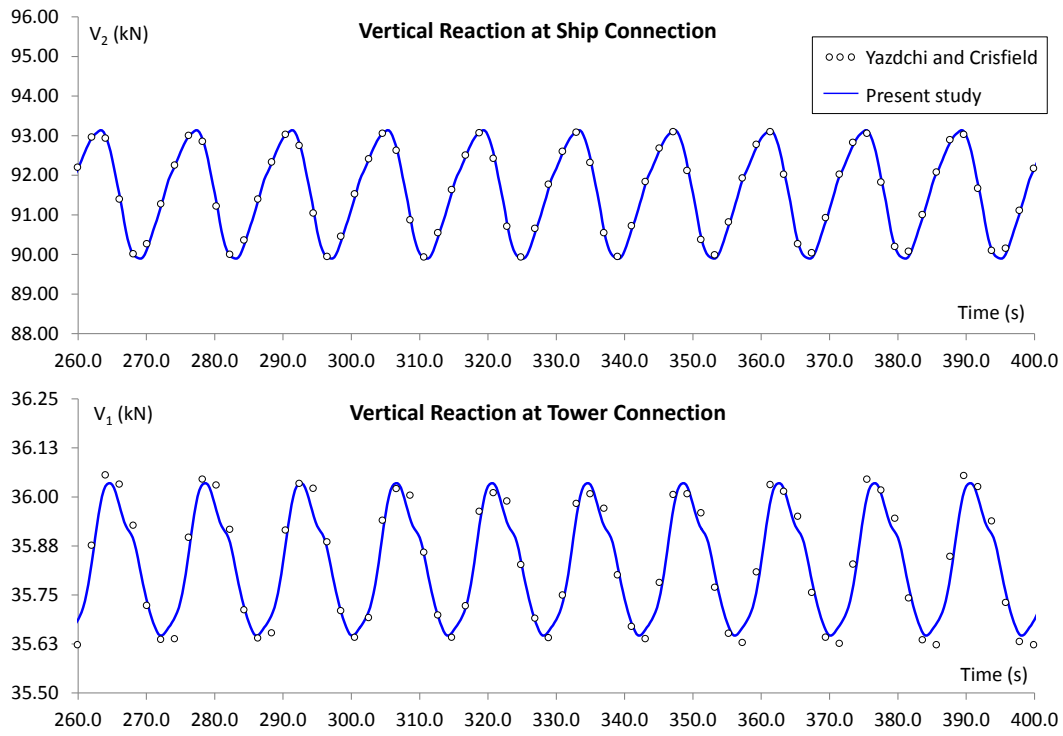


Figure 55: Dynamic Analysis Results for Multilayered Flexible Riser.

6.3.2.

Steel Catenary Riser

In this example, a 4000m long steel catenary riser (SCR) was considered in 3D analysis. The riser, installed in a water depth of 2220m, is connected to a floating production unit (FPU) 15m below the still water level (SWL) with a hang-off angle of 17° , as shown in Figure 56. A uniform finite element mesh with one thousand elements was used to model the SCR, with the top connection node assumed free to rotate while the bottom connection node was fixed.

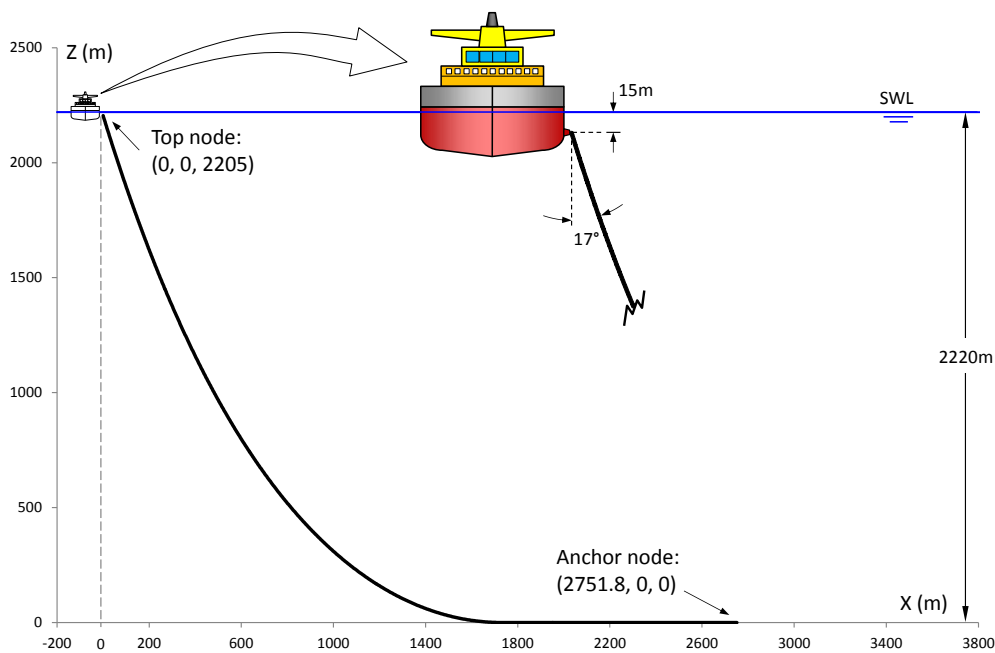


Figure 56: Initial Deformed Configuration for the Steel Catenary Riser.

The riser cross section is a carbon-steel pipe with a corrosion resistant alloy (CRA - clad or liner) as inner layer and two external layers of syntactic and solid polypropylene for thermal insulation. Dimensions and material properties of each layer cross section are shown in Table 8, while details on layer arrangements are shown in Figure 57.

Table 8: Multilayered SCR Cross Section Properties.

| | CRA | Steel | Syntactic PP | Solid PP |
|---|---------|------------------------|--------------|----------|
| Structural external diameter, D_i (m) | 0.185 | 0.225 | 0.375 | 0.387 |
| Structural internal diameter, D_o (m) | 0.175 | 0.185 | 0.225 | 0.375 |
| Pipe internal diameter, D_i (m) | 0.175 | 0.175 ^(*) | - | - |
| Layer thickness, t_i (m) | 0.005 | 0.020 | 0.075 | 0.006 |
| Young modulus, E (kN/m ²) | 1.96E08 | 2.07E08 | 1.08E06 | 1.30E06 |
| Material density, γ (kN/m ³) | 79.853 | 77.000 | 6.278 | 8.829 |
| Inertia coefficient, CM | - | 2.0 ^(*) | - | 2.0 |
| Drag coefficient, CD | - | 1.0 ^(*) | - | 1.0 |
| Contact stiffness, k_c (kN/m ³) ^(**) | 1.00E03 | | 1.00E06 | 1.00E06 |
| Hydrodynamic diameter (m) | - | 0.387 ^(*) | - | 0.387 |
| Internal/External coating weight (kN/m) | - | 0.73295 ^(*) | - | - |
| Internal/External coating buoyancy (kN/m) | - | 0.78298 ^(*) | - | - |

(*) These values are used only in the single layer homogeneous pipe;

(**) These values are used only in the unbonded multilayer model.

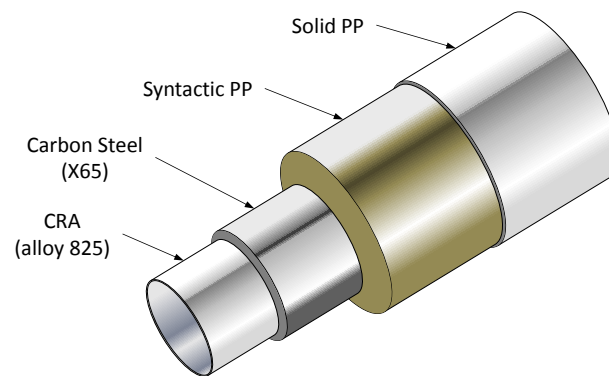


Figure 57: SCR Pipe Cross Section.

Nonlinear springs attached to the element nodes are used to represent vertical contact and friction reactions in longitudinal and lateral directions, at the horizontal seabed surface, considering the uncoupled soil model described in section 5.2.2. The soil springs properties are shown in Table 9.

Table 9: Soil Properties for the SCR Model.

| | |
|--|-------|
| Longitudinal elastic limit, u_{lx} (m) | 0.030 |
| Lateral elastic limit, u_{ly} (m) | 0.219 |
| Longitudinal friction coefficient, μ_x | 0.71 |
| Lateral friction coefficient, μ_y | 0.73 |
| Normal spring stiffness, k_n (kN/m) | 987.0 |

Static and dynamic analyses have been carried out considering self-weight, buoyancy forces, prescribed displacements at the top connection and a current profile along water depth. In the static analysis a horizontal prescribed

displacement of 111m (5% of water depth) was applied to the top node, aligned with the current profile, in a direction 45° from the XZ plane, as shown in Figure 58. The current profile is assumed linear, varying from 0.2m/s at seabed to 1.2m/s at the sea surface. The static analysis was performed with 21 load increments. In the first, only self-weight and buoyancy forces were applied in the model, while prescribed displacement and current were applied simultaneously in the following 20 load increments.

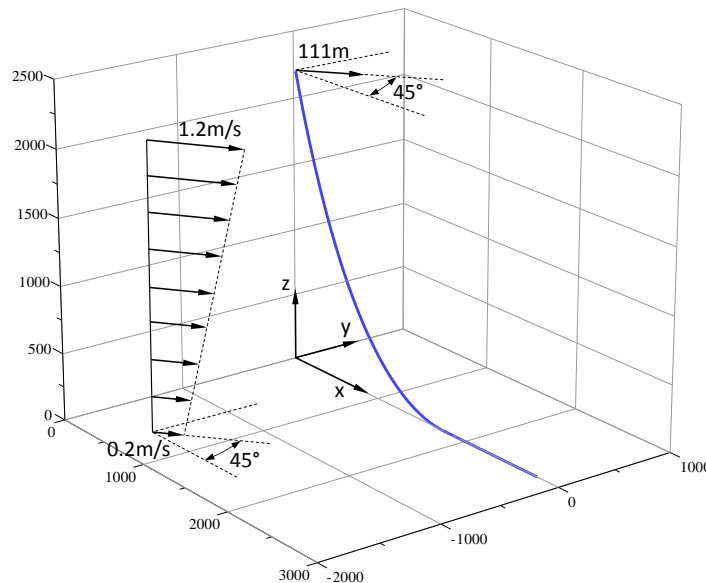


Figure 58: Static Loading for the SCR Model.

The dynamic analysis was carried out using final static configuration as initial condition with all static loading kept constant during dynamic simulation. A harmonic excitation was considered in the XZ plane with amplitudes of 3.4m and 5.1m in X and Z directions, respectively, and period of 11.2s. Figure 59 shows the displacement history applied to the riser's top connection during the total dynamic analysis simulation time of 70s in 700 equal time increments.

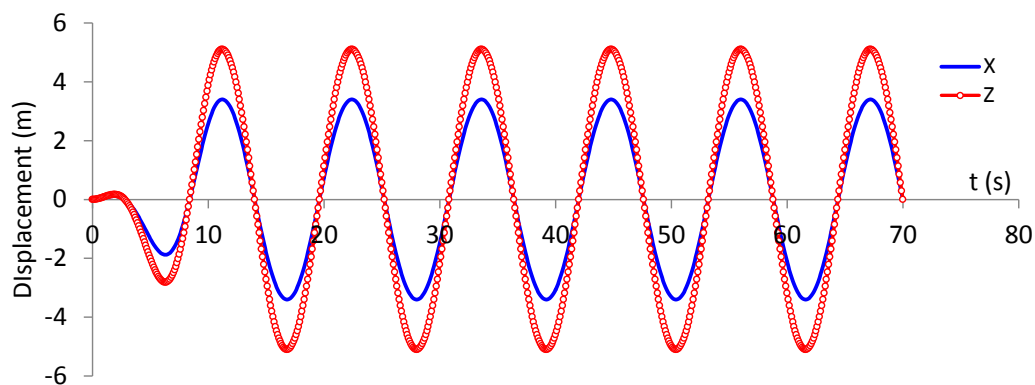


Figure 59: Dynamic Loading for the SCR Model.

In the analysis of the SCR three models were considered: single layer homogeneous beam, bonded multilayer beam (cladded pipe) and unbonded multilayer beam (lined pipe). In the first model, only the carbon steel layer is considered, while the stiffness of the remaining layers was neglected. This is a common assumption employed in global riser analysis. In this case, CRA and thermal insulation layers are considered in weight, buoyancy and drag load evaluations. In multilayered models however, all layers are detailed modeled.

The deformed configuration at the end of static analysis is essentially the same in all model analyses. It is compared to the initial deformed configuration in Figure 60.

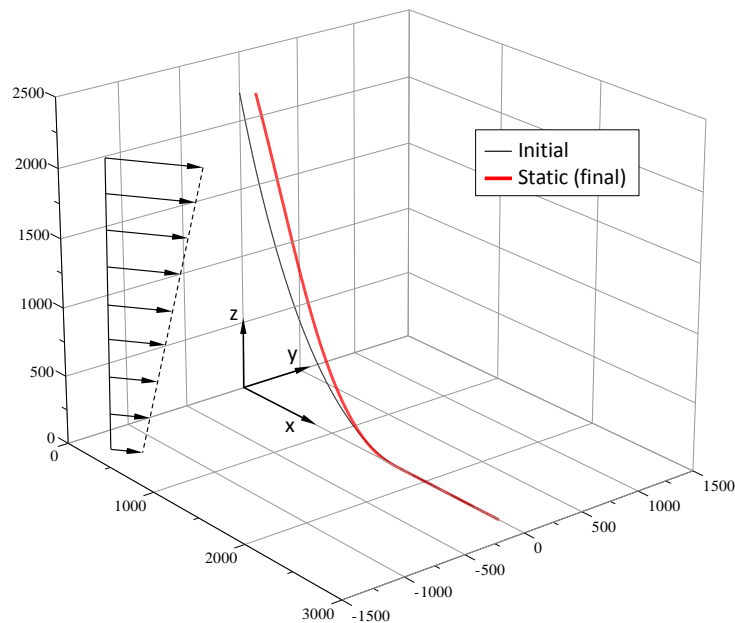


Figure 60: Deformed Configuration at the end of Static Analysis.

Results from the static analysis for axial forces, bending moments and stresses at top connection and touchdown point (TDP) are shown in Table 10.

Table 10: SCR Static Analysis Numerical Results.

| Model | Self-weight and Buoyancy | | | Self-weight, Buoyancy, Prescribed Movement and Current | | |
|---------------------|--------------------------|------------------------------|-------------------------------|--|------------------------------|-------------------------------|
| | Axial Force at Top (kN) | Bending Moment at TDP (kN·m) | von Mises Stress at TDP (MPa) | Axial Force at Top (kN) | Bending Moment at TDP (kN·m) | von Mises Stress at TDP (MPa) |
| Homogeneous (Steel) | 2134.87 | 15.56 | 83.12 | 1965.70 | 21.34 | 77.52 |
| Bonded Multilayer | | | | | | |
| Sum | 2139.52 | 19.20 | - | 1970.12 | 26.32 | - |
| CRA | 359.06 | 2.47 | 144.31 | 330.66 | 3.38 | 143.27 |
| Steel | 1722.53 | 15.54 | 72.36 | 1585.93 | 21.30 | 71.37 |
| Syntactic PP | 50.59 | 1.00 | - | 46.67 | 1.37 | - |
| Solid PP | 7.34 | 0.19 | - | 6.85 | 0.26 | - |
| Unbonded Multilayer | | | | | | |
| Sum | 2142.02 | 19.18 | - | 1972.46 | 26.29 | - |
| CRA | 358.92 | 2.47 | 144.31 | 331.84 | 3.38 | 143.26 |
| Steel | 1724.77 | 15.53 | 72.38 | 1586.75 | 21.28 | 71.36 |
| Syntactic PP | 50.16 | 1.00 | - | 46.21 | 1.37 | - |
| Solid PP | 8.17 | 0.19 | - | 7.67 | 0.26 | - |

The stresses in Table 10 were calculated at the external layer wall, by using the following expressions:

$$\begin{aligned}
 \sigma_{vM} &= \sqrt{(\sigma_{11} - \sigma_{22})^2 + (\sigma_{22} - \sigma_{33})^2 + (\sigma_{33} - \sigma_{11})^2 + 6(\sigma_{12}^2 + \sigma_{13}^2)} \\
 \sigma_{11} &= \frac{N}{A} + \frac{Mr}{I} + \frac{p_i r_i^2 - p_o r_o^2}{r_o^2 - r_i^2}, \quad M = M_y \text{ or } M_z \\
 \sigma_{22} &= \frac{p_i r_i^2 - p_o r_o^2}{r_o^2 - r_i^2} - \frac{r_i^2 r_o^2 (p_o - p_i)}{r^2 (r_o^2 - r_i^2)} \\
 \sigma_{33} &= \frac{p_i r_i^2 - p_o r_o^2}{r_o^2 - r_i^2} + \frac{r_i^2 r_o^2 (p_o - p_i)}{r^2 (r_o^2 - r_i^2)} \\
 \sigma_{12} &= \frac{4V}{3A} + \frac{M_x r}{J}, \quad V = V_y \text{ or } V_z \\
 \sigma_{13} &= \frac{4V}{3A}, \quad V = V_z \text{ or } V_y
 \end{aligned} \tag{149}$$

where σ_{vM} is the von Mises equivalent stress; M_x is the torsion moment, M_y and M_z are the bending moments in y and z directions, respectively; V_y and V_z are the shear forces in y and z directions, respectively; A , I and J are the layer cross section area, moment of inertia and polar moment of inertia, respectively; r_i

and r_o are the layer cross section inner and outer radius, respectively; p_i and p_o are the internal and external pressures in the pipe, respectively; and r is radius to the point where the stresses are calculated ($r_i \leq r \leq r_o$);

Envelopes for axial forces, bending moments and von Misses stresses along the line, from the dynamic analysis results of the bonded multilayered model are shown in Figures 61 to 63. Note that stresses (Figure 63) at TDP are very similar for homogeneous and multilayered models, but they are quite different at the top of the riser. This is because, at TDP, bending moment (Figure 62) contributions to stresses are predominant, and at the top, the axial forces (Figure 61) have more influence on the stresses.

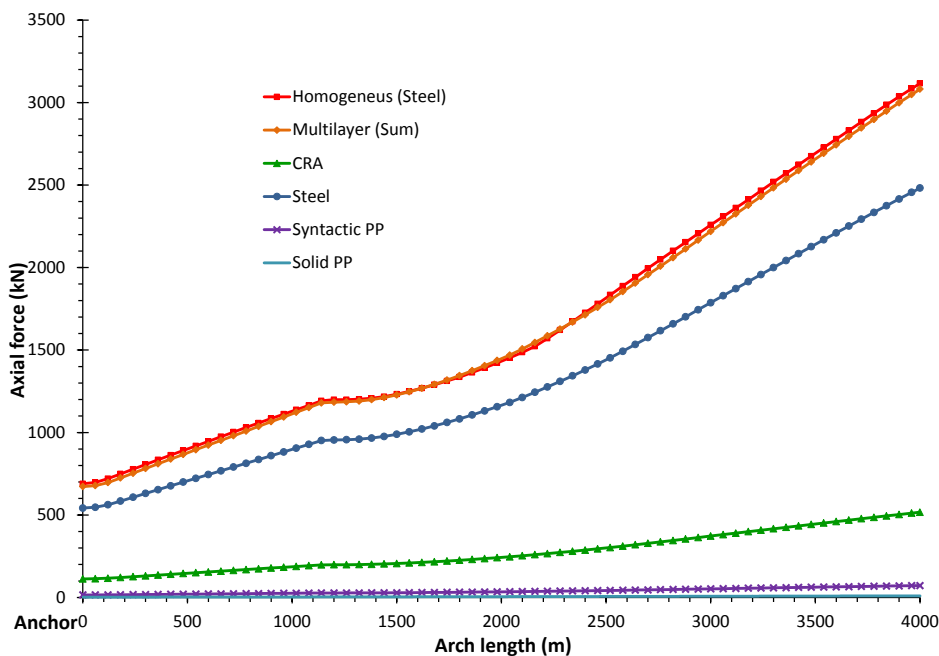


Figure 61: Axial Forces Envelope – Bonded Model.

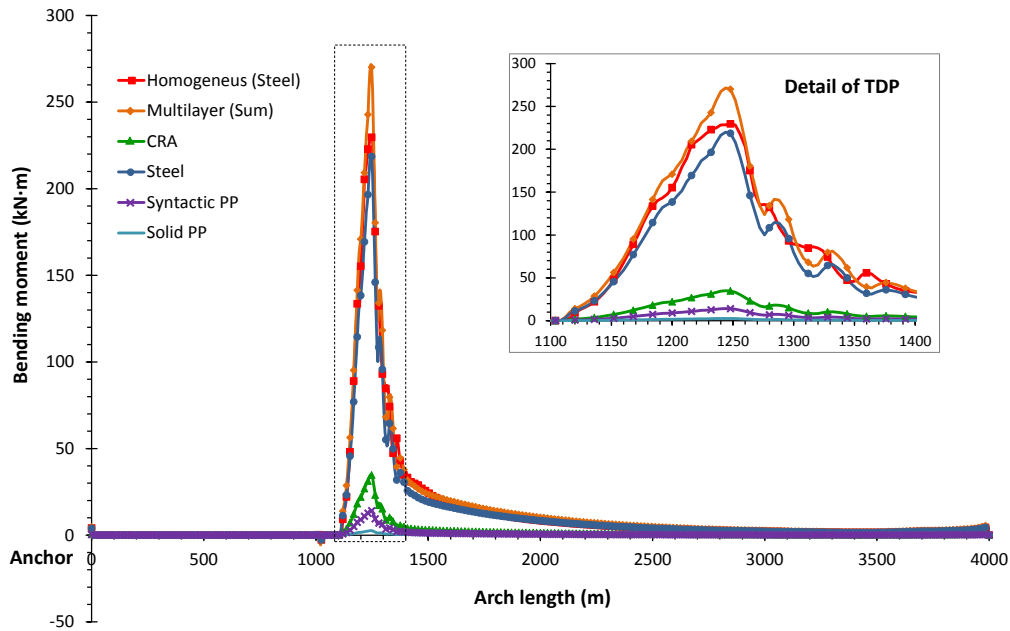


Figure 62: Bending Moment Envelope – Bonded Model.

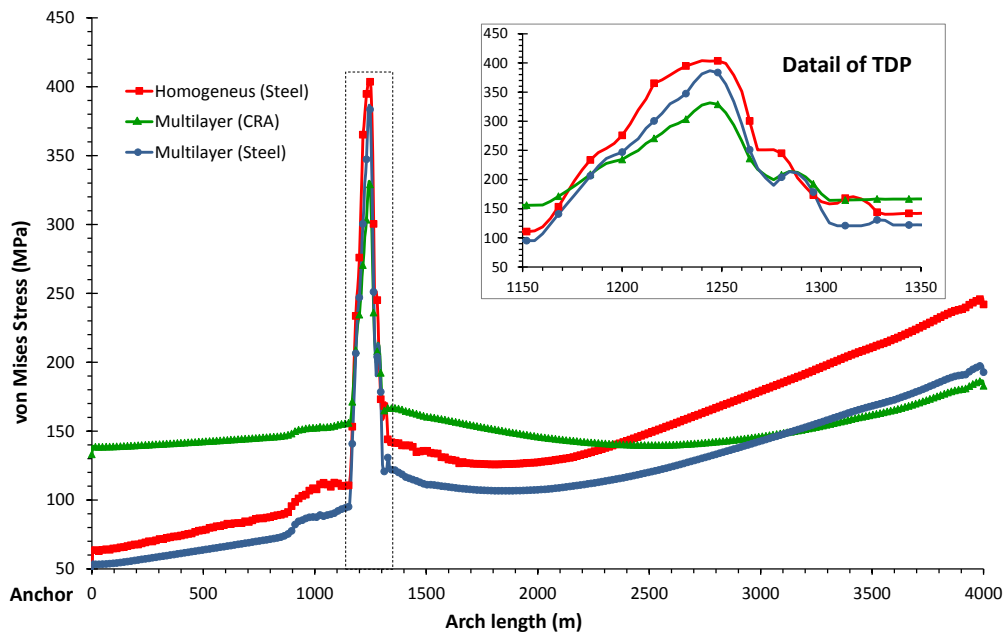


Figure 63: von Mises Stresses Envelope – Bonded Model.

Results obtained for the unbonded multilayered model are also compared to the homogeneous beam results in Figures 64 to 66. Bonded and unbonded multilayered beam solutions are very similar.

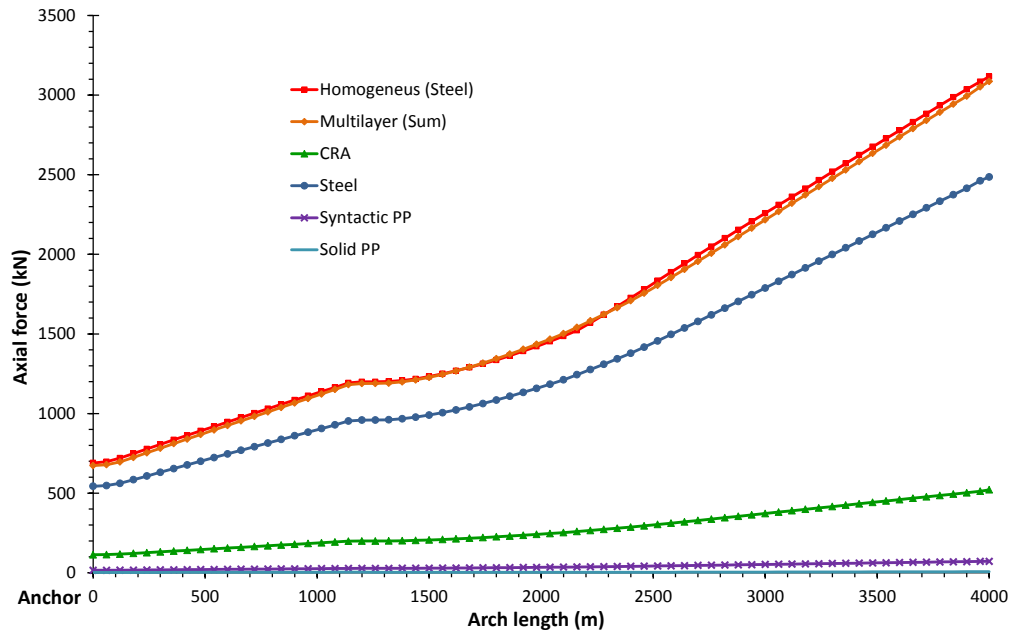


Figure 64: Axial Forces Envelope – Unbonded Model.

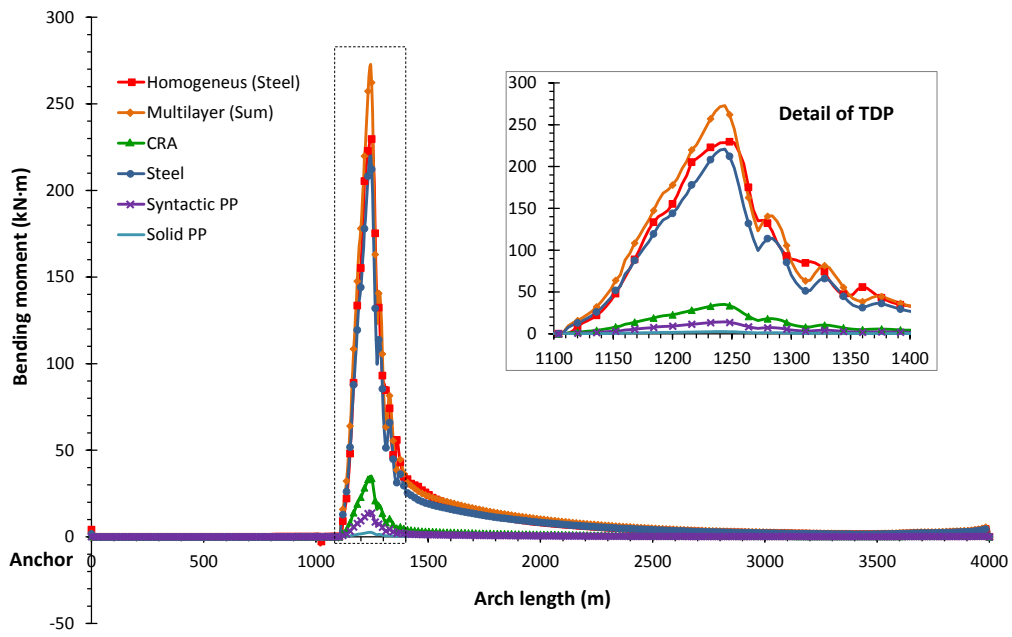


Figure 65: Bending Moment Envelope – Unbonded Model.

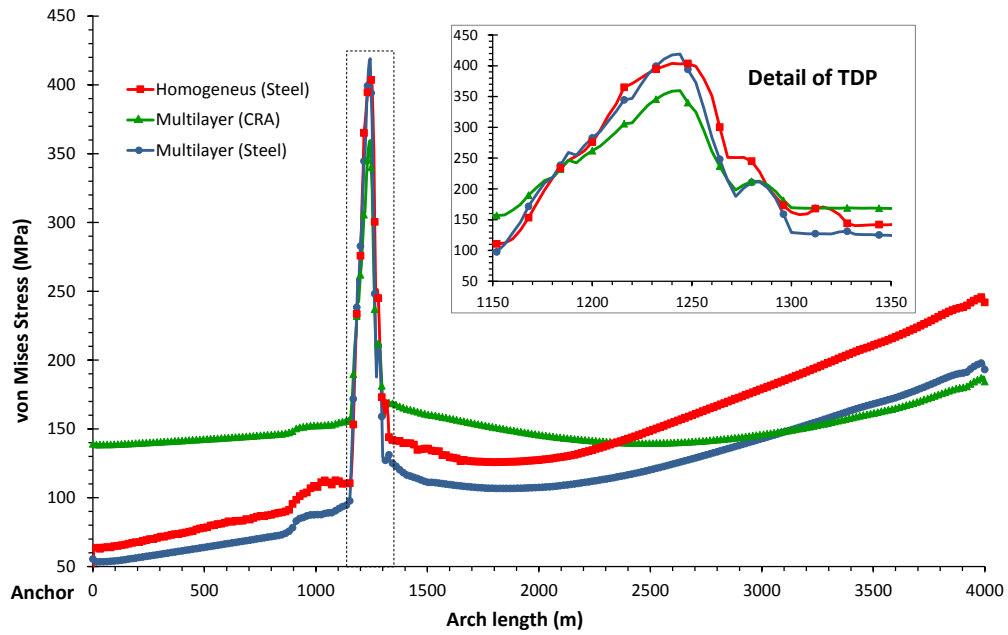


Figure 66: von Mises Stresses Envelope – Unbonded Model.

Time history for the axial forces at top connection and the bending moment at TDP are shown in Figures 67 and 68, respectively. These results show that the homogeneous beam model lead to conservative values for axial forces at the top of the riser.

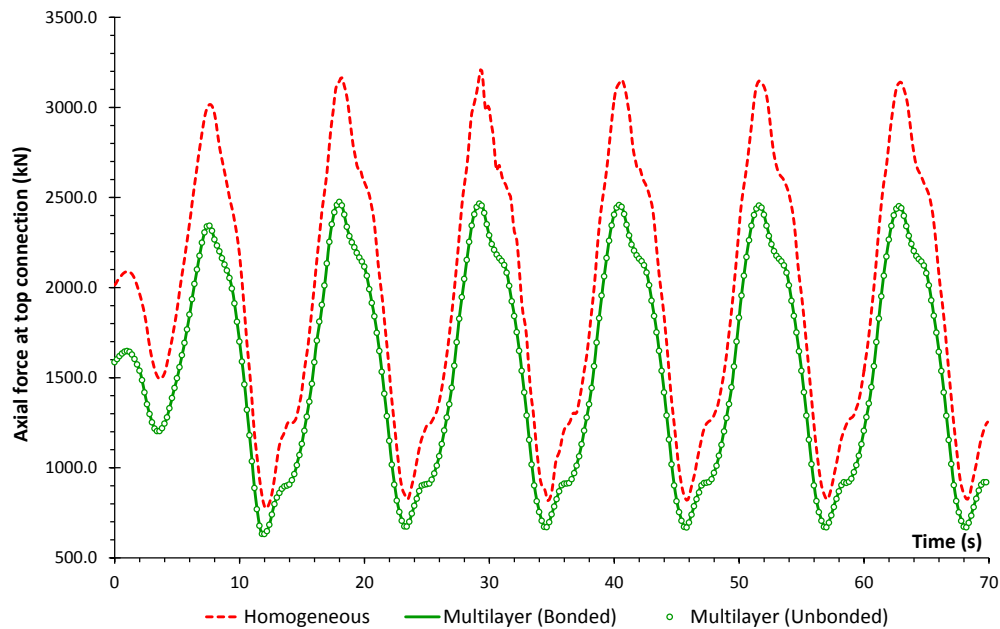


Figure 67: Time History for Axial Force at Top Connection.

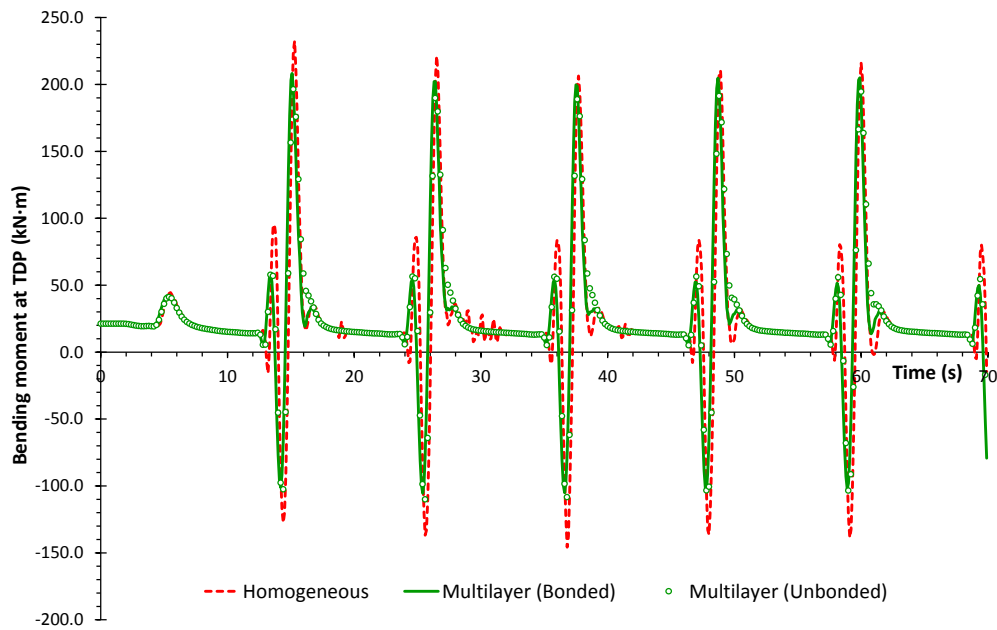


Figure 68: Time History for Bending Moment at Touchdown Point.

The computational efficiency of the multilayered element can be checked in Table 11. These results show that despite the higher number of degrees-of-freedom (unbonded) or the higher number of stiffness matrices and force vectors computations (bonded and unbonded), the multilayer element shows good computational efficiency.

Table 11: Time of analysis for SCR models.

| Model | Time (min.) |
|---------------------|-------------|
| Homogeneous | 0.42 |
| Bonded Multilayer | 0.89 |
| Unbonded Multilayer | 10.55 |

7.

Concluding Remarks

This work focused on representing the behavior of multilayered pipe beams considering possible slip conditions between layers, under general three-dimensional large displacements, in global riser and pipeline analysis. A new finite element formulation for nonlinear dynamic analysis of multilayered pipes, which is capable of an accurate and detailed representation of multilayered pipes, for large displacements and rotations has been presented. The element allows for the representation of both perfectly bonded and unbonded pipes. Global results, such as displacements and rotations at the element centerline, are in good agreement with traditional homogeneous beam formulations available in the literature. Additionally, the element provides detailed information on local results such as stress distribution and internal forces at each pipe layer, and also the contact stress distribution between layers.

In the first three examples (6.1.1 to 6.1.3) the formulation considering large displacements and rotations was tested and the results compared to the ones in literature, presenting a very good agreement. Due to lack of model solutions available in the literature for multilayered pipes, results from the proposed formulation were compared to the ones from traditional homogeneous beam formulations (examples 6.2.2 to 6.2.5) or analytical solutions for multilayered pipes under axial loading (example 6.2.1). All obtained results are in good agreement with the ones presented in the available literature and with the analytical solutions. Examples 6.2.5 and 6.3.1 show that the hydrostatic and hydrodynamic loadings are well represented in the multilayered pipe beam formulation. Applications to riser analysis show very little influence of the detailed multilayer representation in the global dynamic response of the riser, as indicated in examples 6.3.1 and 6.3.2. However, the results from example 6.3.2

illustrate that the homogenous model may lead to conservative values for stresses and axial forces at the top of the riser.

Although not addressed in the examples considered in this work, the FE implementation allows for the possibility to consider material layers of distinct constitutive models for each layer material. For example, considering the analysis of flexible risers, an accurate representation of the material behavior of each layer could improve the results of global analysis, leading directly to the stresses at each element layer, which is currently obtained with a detailed local analysis of the pipe cross section. Another example is the pipeline with an internal layer of corrosion resistant metal (cladded or lined pipes) where the cross section is made of materials with different yield stresses. In this case, one layer can be subjected to plastic strains while the other is still in the elastic regime. This may be the subject of a future work.

The new pipe beam formulation provides the detailed representation of multilayered pipes, yet remains very robust and efficient, even in large scale riser analysis, as shown by the numerical examples presented.

8.

References

- 1 Newmark N. M., Siess C. P., Viest I. M, Tests and Analysis of Composite Beams With Incomplete Interactions. Proc. Soc Exp Stress Anal, 9 (1): 75-92, 1951.
- 2 Schnabl, S., Saje, M., Turk, G. and Planinc, I., Analytical Solution of Two-Layer Beam Taking Into Account Interlayer Slip and Shear Deformation, Journal Of Structural Engineering, 133 (6): 886-894, 2007.
- 3 Foraboschi, P., Analytical Solution of Two-Layer Beam Taking into Account Nonlinear Interlayer Slip, Journal of Engineering Mechanics, 135 (10): 1129-1146, 2009.
- 4 Ecsedi, I., Baksa, A., Static Analysis of Composite Beams With Weak Shear Connection, Applied Mathematical Modelling, 35 (4): 1739-1750, 2011.
- 5 Girhammar U. A., Gopu V. K. A., Composite Beam-Columns With Interlayer Slip - Exact Analysis, Journal of Structural Engineering, 119 (4): 1265-1282, 1993.
- 6 Girhammar U. A., Pan D., Exact Static Analysis of Partially Composite Beams and Beam-Columns, Int. J. of Mechanical Sciences, 49 (2): 239-255, 2007.
- 7 Girhammar U. A., Composite beam-columns with interlayer slip – approximated analysis Int. J. of Mechanical Sciences 50 (12): 1636-1649, 2008.
- 8 Chen W. Q., Wu Y-F, Xu R. Q., State Space Formulation For Composite Beam-Columns With Partial Interaction. Composites Science and Technology, 67(11-12): 2500-2512, 2007.
- 9 Xu R, Wu R, Chen W, Static, dynamic and buckling analysis of partial interaction composite beam theory, Int. J. of Mechanical Sciences 49 (10): 1139-1155, 2007.
- 10 Wu, Y-F, Xu R, Chen W, Free vibrations of the partial-interaction composite members with axial force. J. of Sound and Vibration 299 (4-5): 1074-1093, 2007.
- 11 Schnabl, S., Saje, M., Turk, G. and Planinc, I., Locking-Free Two-Layer Timoshenko Beam Element With Interlayer Slip, Finite Elements in Analysis and Design, 43 (9): 705-714, 2007.
- 12 Čas, B., Saje, M., Planinc, I., Non-Linear Finite Element Analysis of Composite Planar Frames With an Interlayer Slip, Computers and Structures, 82 (23-26): 1901-1912, 2004.

- 13 Čas, B., Saje, M., Planinc, I., Buckling of Layered Wood Columns, *Advances in Engineering Software*, 38 (8-9): 586-597, 2007.
- 14 Krawczyk, P., Frey, F., Large Deflections of Laminated Beams With Interlayer Slips - Part 1: Model Development, *International Journal for Computer-Aided Engineering and Software*, 24 (1): 17-32, 2007.
- 15 Krawczyk, P., Frey, F., Large Deflections of Laminated Beams With Interlayer Slips - Part 2: Finite Element Development, *International Journal for Computer-Aided Engineering and Software*, 24 (1): 33-51, 2007.
- 16 Zona A, Ranzi, G, Finite Element Models For Nonlinear Analysis of Steel-Concrete Composite Beams With Partial Interaction In Combined Bending and Shear, *Finite Elements in Analysis and Design*, 47 (2): 98-118, 2011.
- 17 Sousa Jr. J. B. M., Silva, A. R., Analytical and Numerical Analysis of Multilayered Beams With Interlayer Slip, *Engineering Structures*, 32 (6): 1671-1680, 2010.
- 18 Aguiar, L. L. and Almeida, C. A., On Multi-Layered Pipe Analyses Considering Interface Binding Conditions .21st Brazilian Congress of Mechanical Engineering (COBEM), Oct. 24-28, Natal/RN, 2011.
- 19 Aguiar, L. L. and Almeida, C. A., Multi-Layered Pipe Beam Formulation With Interface Binding-Slip Conditions, *Iberian Latin American Congress on Computational Methods in Engineering (CILAMCE XXXII)*, Nov. 13-16, , Ouro Preto / MG, 2011.
- 20 Mourelle, M. M., *Análise Dinâmica de Sistemas Estruturais Constituídos por Linhas Marítmas*, COPPE/UFRJ, DSc, Engenharia Civil, 1993.
- 21 Crisfield, M., A Consistent Co-rotational Formulation For Non-Linear, Three-Dimensional, Beam-Elements. *Computer Methods in Applied Mechanics and Engineering*, 81 (2): 131-150, August 1990.
- 22 Bathe, K. J., Bolourchi, S., Large Displacement Analysis of Three-Dimensional Beam Structures, *International Journal For Numerical Methods In Engineering*, 14 (7): 961-986, 1979.
- 23 Argyris, J., An Excursion Into Large Rotations, *Computer Methods In Applied Mechanics and Engineering*, 32 (1-3): 85-155, 1982.
- 24 Bathe, K. J., *Finite Element Procedures*, New Jersey, Prentice-Hall, 1996.
- 25 Malvern, L. E., *Introduction to the Mechanics of a Continuous Medium*, Prentice Hall, 1969.
- 26 Pacoste, C., Eriksson, A., Beam Elements In Instability Problems, *Computer Methods for Applied Mechanical Engineer*, 144 (1-2): 163-197, 1997.
- 27 Nunes, C.C.; Soriano, H.L.; Venancio Filho, F. Geometric Nonlinear Analysis of Space Frame with Rotation Greater than 90°, with Euler Angles and Quasi-fixed Local Axes System. *Intl. J. Non-linear Mech.*, 38 (8): 1195-1204, 2003.
- 28 Romero Albino, J. C., *Materiais com Gradação Funcional no Comportamento Dinâmico de Linhas*, Pontifícia Universidade Católica do Rio de Janeiro, PhD Thesis, 2011.

- 29 Simo, J.C. and Vu-Quoc, L., A Three-Dimensional Finite Strain Rod Model. Part II: Computational Aspects, *Comput. Methods Appl. Mech. Engrg.* 58 (1): 79-116, 1986.
- 30 A. Cardona and M. Geradin, A Beam Finite Element Non-Linear Theory With Finite Rotations, *Internat. J. Numer. Methods Engrg.* 26 (11): 2403-2438, 1988.
- 31 Simo, J. C., Hughes, T. J. R., *Computational Inelasticity*, New York Springer-Verlag, 1998.
- 32 Wilkins, M.L., *Calculation of Elasto-plastic Flow, Methods of Computational Physics*, Academic Press, Vol. 3, 1964.
- 33 Lages, E.N., Paulino, G.H., Menezes, I.F.M., Silva, R.R., Nonlinear Finite Element Analysis using an Object-Oriented Philosophy – Application to Beam Elements and to the Cosserat Continuum, *Engineering With Computers*, 15 (1): 73-89, 1999.
- 34 Leon, S.E., Paulino, G.H., Pereira, A., Menezes, I.F.M., Lages, E.N., A Unified Library of Nonlinear Solution Schemes, *Applied Mechanics Reviews*, 64 (4): Article 040803, 2011.
- 35 Hilber, H. M., Hughes, T. J. R. and Taylor, R. L., Improved Numerical Dissipation for Time Integration Algorithms in Structural Dynamics, *Earthquake Engineering and Structural Dynamics*, 5 (3): 283-292, 1977.
- 36 Almeida, C.A., Albino, J.C.R., Menezes, I.F.M. and Paulino, G.H., Geometric Nonlinear Analysis of Functionally Graded Beams Using a Tailored Lagrangian Formulation, *Mechanics Research Communications*, 38 (8): 553-559, 2011.
- 37 Mourelle, M.M., Gonzalez, E.C., Jacob, B.P., ANFLEX – Computational System for Flexible and Rigid Riser Analysis, *Proceedings of the 9th International Symposium on Offshore Engineering, Brazil Offshore 95*, Rio de Janeiro, 1995.
- 38 Chan, S. L., Large Deflection Dynamic Analysis of Space Frames, *Computers and Structures*, 58 (2): 381-387, 1996.
- 39 Morison JR, O'Brien MP, Johnson JW, Schaaf SA. The Forced Exerted by Surface Waves on Piles, *Petroleum Transactions*, 2 (5): 149-154, 1950.
- 40 Yazdchi, M. and Crisfield, M. A., Buoyancy Forces and the 2D Finite Element Analysis of Flexible Offshore Pipes and Risers, *Int. J. Numer. Meth. Engrg.*, 54 (1): 61-88, 2002.
- 41 McNamara, J. F., O'Brien, P. J., Gilroy, S. G., Non-Linear Analysis of Flexible Risers Using Hybrid Finite Elements, *Journal of Offshore Mechanics and Arctic Engineering*, 110 (3): 197-204, 1988.
- 42 Yazdchi, M. and Crisfield, M. A., Non-linear Dynamic Behavior of Flexible Marine Pipes and Risers, *Int. J. Numer. Meth. Engrg.*, 54 (9): 1265-1308, 2002.
- 43 Kordkheili, S.A.H., Bahai, H., Mirtaheri, M., An Updated Lagrangian Finite Element Formulation For Large Displacement Dynamic Analysis of Three-

Dimensional Flexible Riser Structures, *Ocean Engineering*, 38 (5-6): 793-803, 2011.

Appendix A: Two Layer Pipe Beam

In this section the numerical formulation for a two layer pipe beam under axial and bending loadings is presented. Two simple models are then considered: axial (analytical solution) and bending (FEM) displacements. To obtain an analytical solution, the simplifying assumption of an "elastic slip" between layers was considered, allowing reducing the representation of the interaction between layers to a linear elastic effect. The weak formulation for the two layer pipe beam element was also obtained and implemented.

A.1.

Two Layer Pipe Under Axial Loading

Consider the two layer pipe bar with different materials in each layer shown in Figure A.1. The bar has both layers fixed at one end and is subjected to axial forces F_a and F_b at the free end, respectively to layers "a" (inner) and "b" (outer). An adhesive material of small thickness (h) is assumed at the interface between layers.

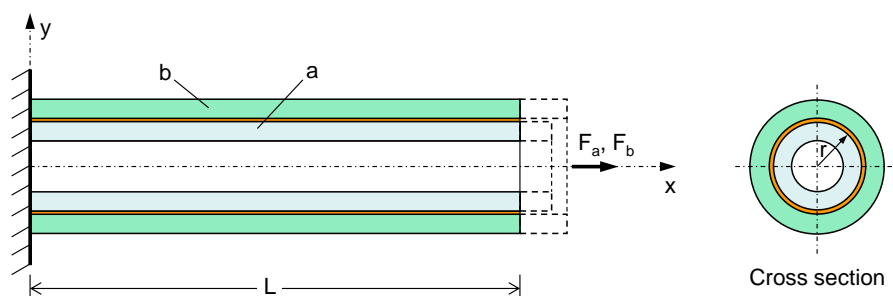


Figure A.1: Two Layer Pipe Bar Under Axial Loading.

Figure A.2 shows a detail of the interface between layers with the interlayer material under shear strain (γ), due to the different displacement fields $u_a(x)$ and $u_b(x)$ in each layer.

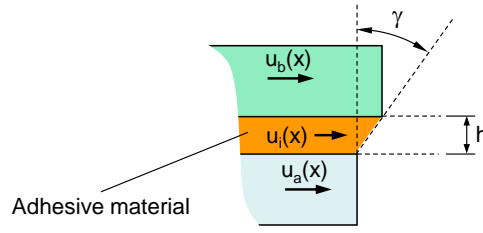


Figure A.2: Detail of the Interface Between Layers.

The interface thickness (h) is assumed very small, compared to the pipe cross section dimensions, and the distribution of shear strain through the interface thickness is assumed constant. Thus, the displacement field $u_i(x)$ within the interface material is given by:

$$u_i(x) = u_a(x) + \frac{u_b(x) - u_a(x)}{h} y \quad (\text{A.1})$$

Therefore, the shear strain (γ) and stress (τ) at the interface results in:

$$\gamma = \frac{du_i}{dy} = \frac{u_b - u_a}{h} \quad \text{and} \quad \tau = G\gamma = \frac{G}{h}(u_b - u_a) \quad (\text{A.2})$$

where G is the shear modulus of the adhesive material.

The equilibrium equation for the composite bar is obtained from the equilibrium of each layer. Figure A.3 shows all forces acting at a segment with length Δx of the inner layer:

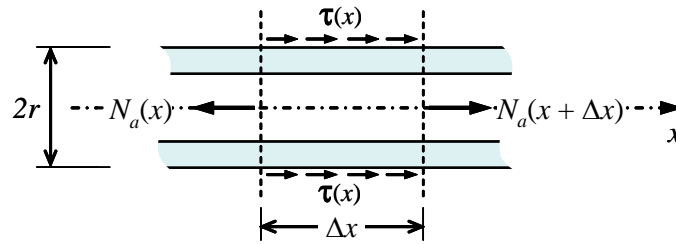


Figure A.3: Equilibrium of the Inner Layer "a".

By taking the equilibrium of forces in x direction, acting on this segment, one obtains:

$$N_a(x) + \frac{dN_a(x)}{dx} \Delta x - N_a(x + \Delta x) + \tau(x)(2\pi r)\Delta x = 0 \Rightarrow \frac{dN_a}{dx} = -\tau(x)(2\pi r) \quad (\text{A.3})$$

The axial strain at the inner layer cross section is given by:

$$\varepsilon_a(x) = \frac{du_a}{dx} = \frac{\sigma_a}{E_a} = \frac{N_a(x)}{E_a A_a} \Rightarrow N_a(x) = E_a A_a \frac{du_a}{dx} \quad (\text{A.4})$$

where E_a and A_a are the Young modulus and the cross section area of layer “a”, respectively.

Substituting Eq. (A.4) in (A.3), one obtains the equilibrium equation of layer “a”, i.e.:

$$E_a A_a \frac{d^2 u_a}{dx^2} = -\frac{G}{h} (2\pi r) (u_b - u_a) = -k(u_b - u_a), \quad \text{with } k = \frac{G}{h} (2\pi r) \quad (\text{A.5})$$

Likewise, considering a segment of outer layer “b”, as shown in Figure A.4, the equilibrium equation for this layer as follows is obtained by considering the equilibrium of forces in x direction, acting on this segment, as:

$$N_b(x) + \frac{dN_b(x)}{dx} \Delta x - N_b(x) - \tau(2\pi r) \Delta x = 0 \Rightarrow \frac{dN_b(x)}{dx} = \tau(2\pi r) \quad (\text{A.6})$$

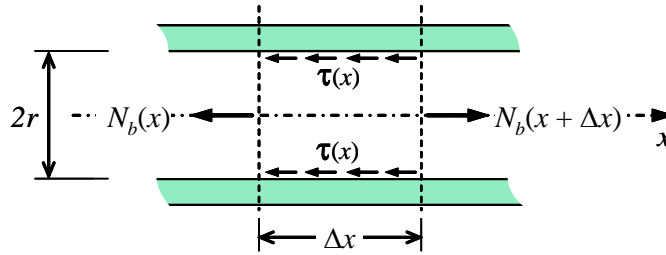


Figure A.4: Equilibrium of the External Layer “b”.

The axial strain at the external layer cross section is given by:

$$\varepsilon_b(x) = \frac{du_b}{dx} = \frac{\sigma_b}{E_b} = \frac{N_b(x)}{E_b A_b} \Rightarrow N_b(x) = E_b A_b \frac{du_b}{dx} \quad (\text{A.7})$$

Combining the results in Eqs. (A.6) and (A.7), one obtains:

$$E_b A_b \frac{d^2 u_b}{dx^2} = \frac{G}{h} (2\pi r) (u_b - u_a) = k(u_b - u_a) \quad (\text{A.8})$$

From Eq. (A.8), the displacement field at the inner layer is expressed in terms of the displacements at the external layer, i.e.:

$$u_a = u_b - \frac{E_b A_b}{k} \frac{d^2 u_b}{dx^2} \quad (\text{A.9})$$

The equilibrium equation for the composite bar is obtained by substituting Eq. (A.9) in Eq. (A.5). Thus, from Eq. (A.9), the second derivative of u_a with relation to x is obtained as:

$$\frac{d^2 u_a}{dx^2} = \frac{d^2 u_b}{dx^2} - \frac{E_b A_b}{k} \frac{d^4 u_b}{dx^4} \quad (\text{A.10})$$

Substituting Eqs. (A.9) and (A.10) in the equilibrium equation of the inner layer “a” (Eq. (A.5)), one obtains:

$$(E_a A_a + E_b A_b) \frac{d^2 u_b}{dx^2} - \frac{E_a A_a E_b A_b}{k} \frac{d^4 u_b}{dx^4} = 0 \quad (\text{A.11})$$

Which the solution results in:

$$u_b(x) = \frac{(C_1 + C_2 x)}{B} + C_3 e^{\frac{\sqrt{AB}}{A} x} + C_4 e^{-\frac{\sqrt{AB}}{A} x} \quad (\text{A.12})$$

where: $A = \frac{E_a A_a E_b A_b}{k}$ and $B = E_a A_a + E_b A_b$

Integration constants (C_1 , C_2 , C_3 and C_4) are evaluated from boundary conditions, as follows:

$$\begin{cases} u_b(0) = 0 \\ u_a(0) = 0 \Rightarrow \left. \frac{d^2 u_b}{dx^2} \right|_{x=0} = 0 \\ \left. \frac{du_b}{dx} \right|_{x=L} = \frac{F_b}{E_b A_b} \\ \left. \frac{du_a}{dx} \right|_{x=L} = \frac{F_a}{E_a A_a} = \frac{F_b}{E_b A_b} - \frac{E_b A_b}{k} \left. \frac{d^3 u_b}{dx^3} \right|_{x=L} \Rightarrow \left. \frac{d^3 u_b}{dx^3} \right|_{x=L} = \frac{k}{E_b A_b} \left(\frac{F_b}{E_b A_b} - \frac{F_a}{E_a A_a} \right) \end{cases} \quad (\text{A.13})$$

From (A.12), the derivatives in Eq. (A.13) results in

$$\begin{aligned} \frac{du_b}{dx} &= \frac{1}{B} C_2 + \frac{\sqrt{AB}}{A} C_3 e^{\frac{\sqrt{AB}}{A} x} - \frac{\sqrt{AB}}{A} C_4 e^{-\frac{\sqrt{AB}}{A} x} \\ \frac{d^2 u_b}{dx^2} &= \frac{B}{A} C_3 e^{\frac{\sqrt{AB}}{A} x} + \frac{B}{A} C_4 e^{-\frac{\sqrt{AB}}{A} x} \\ \frac{d^3 u_b}{dx^3} &= \frac{B\sqrt{AB}}{A^2} C_3 e^{\frac{\sqrt{AB}}{A} x} - \frac{B\sqrt{AB}}{A^2} C_4 e^{-\frac{\sqrt{AB}}{A} x} \end{aligned} \quad (\text{A.14})$$

and the boundary conditions with the result in Eq. (A.12) gives the following system of equations:

$$\begin{cases} u_b(0) = 0 & \Rightarrow \frac{1}{B} C_1 + C_3 + C_4 = 0 \\ \left. \frac{du_b}{dx} \right|_{x=L} = \frac{F_b}{E_b A_b} & \Rightarrow \frac{1}{B} C_2 + \frac{\sqrt{AB}}{A} e^{\frac{L\sqrt{AB}}{A}} C_3 - \frac{\sqrt{AB}}{A} e^{-\frac{L\sqrt{AB}}{A}} C_4 = \frac{F_b}{E_b A_b} \\ \left. \frac{d^2 u_b}{dx^2} \right|_{x=0} = 0 & \Rightarrow C_3 + C_4 = 0 \\ \left. \frac{d^3 u_b}{dx^3} \right|_{x=L} = \frac{k}{E_b A_b} \left(\frac{F_b}{E_b A_b} - \frac{F_a}{E_a A_a} \right) & \Rightarrow \frac{B\sqrt{AB}}{A^2} e^{\frac{L\sqrt{AB}}{A}} C_3 - \frac{B\sqrt{AB}}{A^2} e^{-\frac{L\sqrt{AB}}{A}} C_4 = \frac{k}{E_b A_b} \left(\frac{F_b}{E_b A_b} - \frac{F_a}{E_a A_a} \right) \end{cases} \quad (\text{A.15})$$

That results in the following set of solutions:

$$\begin{aligned}
C_1 &= 0 \\
C_2 &= \frac{BF_b}{E_b A_b} + \frac{kA}{E_b A_b} \left(\frac{F_a}{E_a A_a} - \frac{F_b}{E_b A_b} \right) \\
C_3 &= -C_4 = \frac{k}{E_b A_b} \frac{A^2}{B\sqrt{AB}} \left(\frac{F_a}{E_a A_a} - \frac{F_b}{E_b A_b} \right) \left(e^{\frac{L\sqrt{AB}}{A}} + e^{-\frac{L\sqrt{AB}}{A}} \right)^{-1}
\end{aligned} \tag{A.16}$$

Substituting Eq. (A.12) and the expression of its second derivative (Eq. (A.14)) in Eq. (A.9) one obtains the displacement field along layer “a”, in the form

$$u_a(x) = \frac{(C_1 + C_2 x)}{B} + \left(1 - \frac{E_b A_b B}{k A} \right) \left(C_3 e^{\frac{\sqrt{AB}}{A} x} + C_4 e^{-\frac{\sqrt{AB}}{A} x} \right) \tag{A.17}$$

From the results in Eqs. (A.12) and (A.17), the axial stress distribution along each layer is then obtained:

$$\begin{aligned}
\sigma_a(x) &= E_a \frac{du_a}{dx} = E_a \left(\frac{du_b}{dx} - \frac{E_b A_b}{k} \frac{d^3 u_b}{dx^3} \right) = E_a \left[\frac{C_2}{B} + \frac{\sqrt{AB}}{A} \left(1 - \frac{B}{A} \frac{E_b A_b}{k} \right) \left(C_3 e^{\frac{\sqrt{AB}}{A} x} - C_4 e^{-\frac{\sqrt{AB}}{A} x} \right) \right] \\
\sigma_b(x) &= E_b \frac{du_b}{dx} = E_b \left[\frac{C_2}{B} + \frac{\sqrt{AB}}{A} \left(C_3 e^{\frac{\sqrt{AB}}{A} x} - C_4 e^{-\frac{\sqrt{AB}}{A} x} \right) \right]
\end{aligned} \tag{A.18}$$

and the shear stress distribution along the interface between layers is given by:

$$\tau(x) = \frac{E_b A_b}{2\pi r} \frac{d^2 u_b}{dx^2} = \frac{B}{A} \frac{E_b A_b}{2\pi r} \left(C_3 e^{\frac{\sqrt{AB}}{A} x} + C_4 e^{-\frac{\sqrt{AB}}{A} x} \right) \tag{A.19}$$

This solution is verified in the example 6.2.1.

A.2.

Two Layer Pipe Beam Element Under Bending

Solutions for bending and torsional loadings cannot be obtained analytically. Thus, a numerical approach using FEM is employed. In this case, the formulation of the two-layer pipe beam element with interlayer slip is obtained under the following set of assumptions: small displacements, rotations and strains in both layers; each pipe layer follows Timoshenko’s beam theory; both layers are continuously connected with no separation; and interaction between layers is considered at interlayer material of small thickness (h). Let’s assume that the two layer pipe may also be subjected to in-plane loading, as shown in Figure A.5. The beam has both layers clamped at end “A” and is subjected to axial and transverse

forces and bending moment at the free end. All concentrated loads (Fx_a , Fx_b , Fy_a , Fy_b , M_a e M_b) are applied at point “B” as shown in Figure A.5.

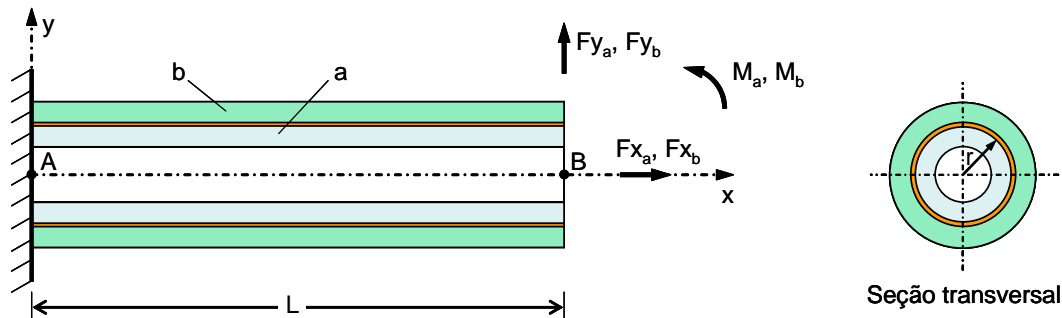


Figure A.5: Two Layer Pipe Beam – Initial Configuration.

Figure A.6 shows the beam in deformed configuration and its degrees-of-freedom, i.e., displacements and rotations, associated to each layer.

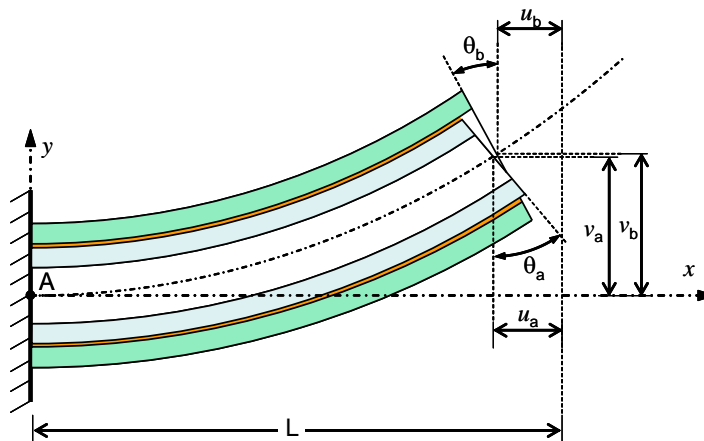


Figure A.6: Two Layer Pipe Beam – Deformed Configuration.

Following the Principle of Energy Conservation one obtains the equilibrium equations from the variation of the total potential energy (Π) of the beam. This functional consists of three parts: axial and shear strain energies of each layer, shear strain energy of the interlayer material and external loads work. The axial strain energy ($\pi_{\sigma_{xx}}$) of both layers is

$$\pi_{\sigma_{xx}} = \underbrace{\frac{1}{2} \int_0^L E_a \left[A_a \left(\frac{du_a}{dx} \right)^2 + I_a \left(\frac{d\theta_a}{dx} \right)^2 \right] dx}_{(\sigma_{xx}) \text{ innerlayer}} + \underbrace{\frac{1}{2} \int_0^L E_b \left[A_b \left(\frac{du_b}{dx} \right)^2 + I_b \left(\frac{d\theta_b}{dx} \right)^2 \right] dx}_{(\sigma_{xx}) \text{ outerlayer}} \quad (\text{A.20})$$

where I_a , I_b are each layer cross section moments of inertia, respectively; E_a , E_b and A_a , A_b are the Young modulus and the cross section area of layers “a” and “b”, respectively.

Assuming small displacements, small slip between layers and no separation between layers, lateral displacements are the same for both layers, i.e. $v_a = v_b = v$. Thus, the shear strain energy of both layers is given by

$$\pi_{\tau_{xy}} = \underbrace{\frac{m}{2} \int_0^L G_a A_a \left(\frac{dv}{dx} - \theta_a \right)^2 dx}_{(\tau_{xy}) \text{ innerlayer}} + \underbrace{\frac{m}{2} \int_0^L G_b A_b \left(\frac{dv}{dx} - \theta_b \right)^2 dx}_{(\tau_{xy}) \text{ outerlayer}} \quad (\text{A.21})$$

where m is a geometric correction factor associated for the shear stress distribution in each layer cross section; G_a and G_b are the shear modulus of layers “a” and “b”, respectively.

The total external loading work is given by:

$$W = -F_{xa} u_a(L) - F_{xb} u_b(L) - (F_{ya} + F_{yb}) v(L) - M_a \theta_a(L) - M_b \theta_b(L) \quad (\text{A.22})$$

Shear strains and stresses at the interface material, related to bending displacements are given by

$$\begin{aligned} \gamma_i(\varphi) &= \frac{u_b - u_a - r(\theta_b - \theta_a) \cos \varphi}{h} \\ \tau_i(\varphi) &= G \gamma_i(\varphi) = \frac{G}{h} (u_b - u_a - r(\theta_b - \theta_a) \cos \varphi) \end{aligned} \quad (\text{A.23})$$

where φ is the angular coordinate at the interface, as shown in Figure A.7.

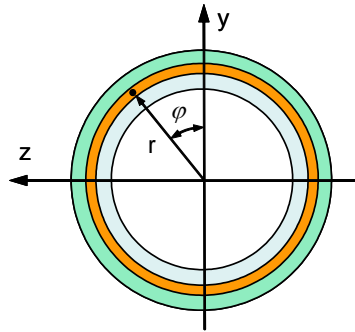


Figure A.7: Definition of φ Angle.

Finally, the interlayer material strain energy is

$$\pi_{\tau_i} = \frac{1}{2} \int_V \tau_i \gamma_i dV \quad (\text{A.24})$$

that combined with the results in Eq. (A.23) results in

$$\pi_{\tau_i} = \frac{1}{2} \int_0^L \int_0^{2\pi} \frac{rG}{h} (u_b - u_a - r(\theta_b - \theta_a) \cos \varphi)^2 d\varphi dx \quad (\text{A.25})$$

and, after angular integration, we have

$$\pi_{\tau_i} = \frac{1}{2} \int_0^L k \left[\frac{r^2}{2} (\theta_b - \theta_a)^2 + (u_b - u_a)^2 \right] dx, \quad \text{where } k = \frac{G}{h} (2\pi r) \quad (\text{A.26})$$

Thus, the total potential energy for the composite bar results in

$$\Pi = \pi_{\sigma_{xx}} + \pi_{\tau_{xy}} + \pi_{\tau_i} + W \quad (\text{A.27})$$

By applying the principle of virtual work ($\delta\Pi = 0$), one obtains

$$\delta\Pi = \delta\pi_{\sigma_{xx}} + \delta\pi_{\tau_{xy}} + \delta\pi_{\tau_i} + \delta W = 0 \quad (\text{A.28})$$

Each energy term in Eq. (A.28) is defined in Eqs. (A.20), (A.21), (A.25) and (A.22) which variation with respect to the displacement degrees-of-freedom results in

$$\begin{aligned} \delta\pi_{\sigma_{xx}} &= \int_0^L \left(E_a A_a \frac{du_a}{dx} \delta \frac{du_a}{dx} + E_a I_a \frac{d\theta_a}{dx} \delta \frac{d\theta_a}{dx} + E_b A_b \frac{du_b}{dx} \delta \frac{du_b}{dx} + E_b I_b \frac{d\theta_b}{dx} \delta \frac{d\theta_b}{dx} \right) dx \\ \delta\pi_{\tau_{xy}} &= \int_0^L m \left(G_a A_a \left(\frac{dv}{dx} - \theta_a \right) \delta \left(\frac{dv}{dx} - \theta_a \right) + G_b A_b \left(\frac{dv}{dx} - \theta_b \right) \delta \left(\frac{dv}{dx} - \theta_b \right) \right) dx \\ \delta\pi_{\tau_i} &= \int_0^L k \left(\frac{r^2}{2} (\theta_b - \theta_a) \delta (\theta_b - \theta_a) + (u_b - u_a) \delta (u_b - u_a) \right) dx \\ \delta W &= -F_{xa} \delta u_a(L) - F_{xb} \delta u_b(L) - (F_{ya} + F_{yb}) \delta v(L) - M_a \delta \theta_a(L) - M_b \delta \theta_b(L) \end{aligned} \quad (\text{A.29})$$

The element displacement fields are then obtained, from nodal displacements, by using a suitable interpolation matrix $\mathbf{H}(\xi)$ in the form

$$\begin{bmatrix} u_a(\xi) \\ u_b(\xi) \\ v(\xi) \\ \theta_a(\xi) \\ \theta_b(\xi) \end{bmatrix} = \mathbf{H}(\xi) \hat{\mathbf{u}} \quad (\text{A.30})$$

where ξ is the element local coordinate ($-\frac{\ell}{2} \leq \xi \leq \frac{\ell}{2}$); ℓ is the element length; $\mathbf{H}(\xi)$ is an interpolation matrix; $\hat{\mathbf{u}}$ is the vector of nodal displacements of the element.

In this work the three node quadratic Lagrangian element was considered, which interpolation functions are shown in Figure A.8.

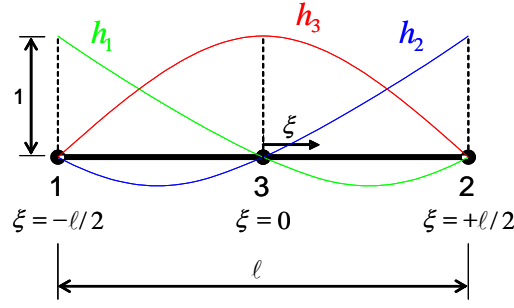


Figure A.8: Longitudinal Interpolation Functions.

These functions $h_i(\xi)$ are defined, in the local element system, as:

$$h_1(\xi) = \frac{\xi(2\xi - \ell)}{\ell^2}, h_2(\xi) = \frac{\xi(2\xi + \ell)}{\ell^2} \text{ and } h_3(\xi) = -\frac{(2\xi + \ell)(2\xi - \ell)}{\ell^2} \quad (\text{A.31})$$

Interpolation matrices ($\mathbf{H}(\xi)$) associated to each degree-of-freedom and referred to the element displacement vector ($\hat{\mathbf{u}}$), for the two layer pipe beam element, are defied as:

$$\begin{aligned} \mathbf{H}_{u_a} &= [h_1 \quad h_2 \quad h_3 \quad 0 \quad 0] \\ \mathbf{H}_{u_b} &= [0 \quad 0 \quad 0 \quad h_1 \quad h_2 \quad h_3 \quad 0 \quad 0] \\ \mathbf{H}_v &= [0 \quad 0 \quad 0 \quad 0 \quad 0 \quad 0 \quad h_1 \quad h_2 \quad h_3 \quad 0 \quad 0 \quad 0 \quad 0 \quad 0] \\ \mathbf{H}_{\theta_a} &= [0 \quad 0 \quad h_1 \quad h_2 \quad h_3 \quad 0 \quad 0] \\ \mathbf{H}_{\theta_b} &= [0 \quad 0 \quad h_1 \quad h_2 \quad h_3] \\ \hat{\mathbf{u}}^T &= [u_1^a \quad u_2^a \quad u_3^a \quad u_1^b \quad u_2^b \quad u_3^b \quad v_1 \quad v_2 \quad v_3 \quad \theta_1^a \quad \theta_2^a \quad \theta_3^a \quad \theta_1^b \quad \theta_2^b \quad \theta_3^b] \end{aligned} \quad (\text{A.32})$$

Thus, the integrals in Eq. (A.29) can be rewritten within the element domain sby considering the interpolation functions in Eq. (A.31), i.e.:

$$\begin{cases} \delta\pi_{\sigma_{xx}} = \int_{-\ell/2}^{\ell/2} (E_a A_a \frac{du_a}{d\xi} \delta \frac{du_a}{d\xi} + E_a I_a \frac{d\theta_a}{d\xi} \delta \frac{d\theta_a}{d\xi} + E_b A_b \frac{du_b}{d\xi} \delta \frac{du_b}{d\xi} + E_b I_b \frac{d\theta_b}{d\xi} \delta \frac{d\theta_b}{d\xi}) d\xi \\ \delta\pi_{\tau_{xy}} = \int_{-\ell/2}^{\ell/2} m [G_a A_a (\frac{dv}{d\xi} - \theta_a) \delta (\frac{dv}{d\xi} - \theta_a) + G_b A_b (\frac{dv}{d\xi} - \theta_b) \delta (\frac{dv}{d\xi} - \theta_b)] d\xi \\ \delta\pi_{\tau_t} = \int_{-\ell/2}^{\ell/2} k [\frac{\tau^2}{2} (\theta_b - \theta_a) \delta (\theta_b - \theta_a) + (u_b - u_a) \delta (u_b - u_a)] d\xi \end{cases} \quad (\text{A.33})$$

By taking displacements derivatives, one obtains:

$$\begin{bmatrix} \frac{du_a(\xi)}{d\xi} \\ \frac{d\theta_a(\xi)}{d\xi} \\ \frac{dv(\xi)}{d\xi} \\ \frac{du_b(\xi)}{d\xi} \\ \frac{d\theta_b(\xi)}{d\xi} \end{bmatrix} = \frac{d\mathbf{H}(\xi)}{d\xi} \hat{\mathbf{u}} = \mathbf{B}(\xi) \hat{\mathbf{u}} \text{ and } \begin{bmatrix} \delta \frac{du_a(\xi)}{d\xi} \\ \delta \frac{d\theta_a(\xi)}{d\xi} \\ \delta \frac{dv(\xi)}{d\xi} \\ \delta \frac{du_b(\xi)}{d\xi} \\ \delta \frac{d\theta_b(\xi)}{d\xi} \end{bmatrix} = \frac{d\mathbf{H}(\xi)}{d\xi} \delta \hat{\mathbf{u}} = \mathbf{B}(\xi) \delta \hat{\mathbf{u}} \quad (\text{A.34})$$

Equation (A.28) results, for the complete element assemblage, in the following system of equations:

$$\mathbf{K}\hat{\mathbf{U}} = \mathbf{F} \quad (\text{A.35})$$

where \mathbf{K} is the global stiffness matrix resulting from each element stiffness matrix (\mathbf{K}_e); $\hat{\mathbf{U}}$ is the nodal displacement vector for the entire structure; \mathbf{F} is the global external loading vector.

Thus, the element stiffness matrix associated to six degrees-of-freedom per node is obtained as

$$\begin{aligned} \mathbf{K}_e = & \int_{-\ell/2}^{\ell/2} (E_a A_a \mathbf{B}_{u_a}^T \mathbf{B}_{u_a} + E_a I_a \mathbf{B}_{\theta_a}^T \mathbf{B}_{\theta_a} + E_b A_b \mathbf{B}_{u_b}^T \mathbf{B}_{u_b} + E_b I_b \mathbf{B}_{\theta_b}^T \mathbf{B}_{\theta_b}) d\xi \\ & + \int_{-\ell/2}^{\ell/2} m [G_a A_a (\mathbf{B}_v^T - \mathbf{H}_{\theta_a}^T) (\mathbf{B}_v - \mathbf{H}_{\theta_a}) + G_b A_b (\mathbf{B}_v^T - \mathbf{H}_{\theta_b}^T) (\mathbf{B}_v - \mathbf{H}_{\theta_b})] d\xi \quad (\text{A.36}) \\ & + \int_{-\ell/2}^{\ell/2} k \left[\frac{r^2}{2} (\mathbf{H}_{\theta_b}^T - \mathbf{H}_{\theta_a}^T) (\mathbf{H}_{\theta_b} - \mathbf{H}_{\theta_a}) + (\mathbf{H}_{u_b}^T - \mathbf{H}_{u_a}^T) (\mathbf{H}_{u_b} - \mathbf{H}_{u_a}) \right] d\xi \end{aligned}$$

where:

$$\begin{aligned} \mathbf{B}_{u_a} &= \begin{bmatrix} \frac{dh_1}{d\xi} & \frac{dh_2}{d\xi} & \frac{dh_3}{d\xi} & 0 & 0 & 0 & 0 & 0 & 0 & 0 & 0 & 0 & 0 & 0 & 0 \end{bmatrix} \\ \mathbf{B}_{u_b} &= \begin{bmatrix} 0 & 0 & 0 & \frac{dh_1}{d\xi} & \frac{dh_2}{d\xi} & \frac{dh_3}{d\xi} & 0 & 0 & 0 & 0 & 0 & 0 & 0 & 0 & 0 \end{bmatrix} \\ \mathbf{B}_v &= \begin{bmatrix} 0 & 0 & 0 & 0 & 0 & 0 & \frac{dh_1}{d\xi} & \frac{dh_2}{d\xi} & \frac{dh_3}{d\xi} & 0 & 0 & 0 & 0 & 0 & 0 \end{bmatrix} \quad (\text{A.37}) \\ \mathbf{B}_{\theta_a} &= \begin{bmatrix} 0 & 0 & 0 & 0 & 0 & 0 & 0 & 0 & 0 & \frac{dh_1}{d\xi} & \frac{dh_2}{d\xi} & \frac{dh_3}{d\xi} & 0 & 0 & 0 \end{bmatrix} \\ \mathbf{B}_{\theta_b} &= \begin{bmatrix} 0 & 0 & 0 & 0 & 0 & 0 & 0 & 0 & 0 & 0 & 0 & 0 & \frac{dh_1}{d\xi} & \frac{dh_2}{d\xi} & \frac{dh_3}{d\xi} \end{bmatrix} \end{aligned}$$

By solving the integrals of Eq. (A.36), one obtains the two layer pipe beam stiffness matrix, in closed form:

The internal forces and bending moment in a beam element are calculated as follows:

$$N = EA \frac{du}{dx} \quad \text{and} \quad M = EI \frac{d\theta}{dx} \quad (\text{A.39})$$

Thus, considering each element layer interpolated nodal displacements and rotations, one obtains

$$\begin{aligned} M_a(\xi) &= \frac{E_a I_a}{\ell^2} (\theta_2^a(\ell + 4\xi) - \theta_1^a(\ell - 4\xi) - 8\xi\theta_3^a) \\ N_a(\xi) &= \frac{E_a A_a}{\ell^2} (u_2^a(\ell + 4\xi) - u_1^a(\ell - 4\xi) - 8\xi u_3^a) \\ M_b(\xi) &= \frac{E_b I_b}{\ell^2} (\theta_2^b(\ell + 4\xi) - \theta_1^b(\ell - 4\xi) - 8\xi\theta_3^b) \\ N_b(\xi) &= \frac{E_b A_b}{\ell^2} (u_2^b(\ell + 4\xi) - u_1^b(\ell - 4\xi) - 8\xi u_3^b) \end{aligned} \quad (\text{A.40})$$

From these internal forces the axial stresses along each element layer is calculated:

$$\begin{aligned} \sigma_a(\xi, y) &= \frac{N_a(\xi)}{A_a} + \frac{M_a(\xi)}{I_a} y \\ \sigma_b(\xi, y) &= \frac{N_b(\xi)}{A_b} + \frac{M_b(\xi)}{I_b} y \end{aligned} \quad (\text{A.41})$$

Interface shear stresses at each element node are calculated from Eq. (A.23):

$$\tau^{(i)}(y) = \frac{k}{2\pi r} [u_b^{(i)} - u_a^{(i)} - r(\theta_b^{(i)} - \theta_a^{(i)})y] \quad (\text{A.42})$$

where i is node index.

Appendix B: Nonlinear Multilayer Pipe Beam Element Matrices

B.1.

Linear Stiffness Matrix

By solving the integrals in Eq. (38), one can rewrite the linear stiffness matrix for element layer- k in closed form, as follows:

$$\mathbf{K}_L^k = \begin{bmatrix}
 \frac{E^k A^k}{\ell} & 0 & 0 & 0 & 0 & 0 & -\frac{E^k A^k}{\ell} & 0 & 0 & 0 & 0 & 0 & 0 & 0 \\
 \frac{12E^k I^k}{\ell^3} & 0 & 0 & 0 & \frac{6E^k I^k}{\ell^2} & 0 & -\frac{12E^k I^k}{\ell^3} & 0 & 0 & 0 & \frac{6E^k I^k}{\ell^2} & 0 & 0 & -\frac{12E^k I^k}{\ell^2} \\
 \frac{12E^k I^k}{\ell^3} & 0 & -\frac{6E^k I^k}{\ell^2} & 0 & 0 & 0 & 0 & -\frac{12E^k I^k}{\ell^3} & 0 & -\frac{6E^k I^k}{\ell^2} & 0 & -\frac{12E^k I^k}{\ell^2} & 0 & 0 \\
 \frac{G^k J^k}{\ell} & 0 & 0 & 0 & 0 & 0 & 0 & 0 & -\frac{G^k J^k}{\ell} & 0 & 0 & 0 & 0 & 0 \\
 \frac{4E^k I^k}{\ell} & 0 & 0 & 0 & 0 & \frac{6E^k I^k}{\ell^2} & 0 & \frac{2E^k I^k}{\ell} & 0 & \frac{6E^k I^k}{\ell} & 0 & 0 & 0 & 0 \\
 \frac{4E^k I^k}{\ell} & 0 & -\frac{6E^k I^k}{\ell^2} & 0 & 0 & 0 & 0 & 0 & \frac{2E^k I^k}{\ell} & 0 & 0 & 0 & -\frac{6E^k I^k}{\ell} & 0 \\
 \frac{E^k A^k}{\ell} & 0 & 0 & 0 & 0 & 0 & 0 & 0 & 0 & 0 & 0 & 0 & 0 & 0 \\
 \frac{12E^k I^k}{\ell^3} & 0 & 0 & 0 & 0 & 0 & -\frac{6E^k I^k}{\ell^2} & 0 & 0 & \frac{12E^k I^k}{\ell^2} & 0 & 0 & 0 & \frac{12E^k I^k}{\ell^2} \\
 \frac{12E^k I^k}{\ell^3} & 0 & 0 & 0 & 0 & 0 & 0 & 0 & \frac{6E^k I^k}{\ell^2} & 0 & \frac{12E^k I^k}{\ell^2} & 0 & 0 & 0 \\
 \frac{G^k J^k}{\ell} & 0 & 0 & 0 & 0 & 0 & 0 & 0 & 0 & 0 & 0 & 0 & 0 & 0 \\
 \frac{4E^k I^k}{\ell} & 0 & \frac{6E^k I^k}{\ell} & 0 & 0 & 0 & 0 & 0 & 0 & \frac{6E^k I^k}{\ell} & 0 & 0 & 0 & 0 \\
 \frac{4E^k I^k}{\ell} & 0 & 0 & 0 & 0 & 0 & 0 & 0 & 0 & 0 & 0 & 0 & -\frac{6E^k I^k}{\ell} & 0 \\
 \frac{12E^k I^k}{\ell} + G^k A^k \ell & 0 & 0 & 0 & 0 & 0 & 0 & 0 & 0 & 0 & 0 & 0 & 0 & 0 \\
 \frac{12E^k I^k}{\ell} + G^k A^k \ell & 0 & 0 & 0 & 0 & 0 & 0 & 0 & 0 & 0 & 0 & 0 & 0 & 0
 \end{bmatrix} \quad (\text{B.1})$$

symmetric

where E^k and G^k are material Young and shear modulus of layer- k , respectively; A^k , I^k and J^k are cross section area, moment of inertia with respect to the cross-section axis of symmetry, and polar moment of inertia with respect to the layer- k cross section geometric center, respectively.

B.2.**Geometric Stiffness Matrix**

Accordingly, the stiffness matrix associated to the nonlinear strain components defined in Eq. (12) is obtained in closed form as:

$$\mathbf{K}_G^k = \begin{bmatrix} -\frac{F_1^k}{\ell} & 0 & 0 & 0 & -\frac{F_5^k}{\ell} & -\frac{F_6^k}{\ell} & \frac{F_1^k}{\ell} & 0 & 0 & 0 & \frac{F_5^k}{\ell} + F_3^k & \frac{F_6^k}{\ell} - F_2^k & F_3^k & F_2^k \\ & -C_1 F_1^k & 0 & \frac{F_5^k}{\ell} & -\frac{F_4^k}{\ell} & -C_2 F_1^k & 0 & C_1 F_1^k & 0 & -\frac{F_5^k}{\ell} - F_3^k & \frac{F_4^k}{\ell} & -C_2 F_1^k & 0 & C_1 \ell F_1^k \\ & & -C_1 F_1^k & \frac{F_6^k}{\ell} & C_2 F_1^k & -\frac{F_4^k}{\ell} & 0 & 0 & C_1 F_1^k & F_2^k - \frac{F_6^k}{\ell} & C_2 F_1^k & \frac{F_4^k}{\ell} & C_1 \ell F_1^k & 0 \\ & & & -\frac{JF_1^k}{A\ell} & \frac{\ell F_2^k}{6} & \frac{\ell F_3^k}{6} & 0 & -\frac{F_5^k}{\ell} & -\frac{F_6^k}{\ell} & \frac{JF_1^k}{A\ell} & -\frac{\ell F_2^k}{6} & -\frac{\ell F_3^k}{6} & -F_6^k & -F_5^k \\ & & & & -C_3 F_1^k & 0 & \frac{F_5^k}{\ell} & \frac{F_4^k}{\ell} & -C_2 F_1^k & -\frac{\ell F_2^k}{6} & C_4 F_1^k & -\frac{F_4^k}{2} & -C_2 \ell F_1^k & \frac{F_4^k}{2} \\ & & & & & -C_3 F_1^k & \frac{F_6^k}{\ell} & C_2 F_1^k & \frac{F_4^k}{\ell} & -\frac{\ell F_3^k}{6} & \frac{F_4^k}{2} & C_4 F_1^k & \frac{F_4^k}{2} & C_2 \ell F_1^k \\ & & & & & & -\frac{F_1^k}{\ell} & 0 & 0 & 0 & -F_3^k - \frac{F_5^k}{\ell} & F_2^k - \frac{F_6^k}{\ell} & -F_3^k & -F_2^k \\ & & & & & & & -C_1 F_1^k & 0 & F_3^k + \frac{F_5^k}{\ell} & -\frac{F_4^k}{\ell} & C_2 F_1^k & 0 & -C_1 \ell F_1^k \\ & & & & & & & & -C_1 F_1^k & -C_1 F_1^k & \frac{F_6^k}{\ell} - F_2^k & -C_2 F_1^k & -\frac{F_4^k}{\ell} & -C_1 \ell F_1^k & 0 \\ & & & & & & & & & & -\frac{JF_1^k}{A\ell} & \frac{\ell F_2^k}{6} & \frac{\ell F_3^k}{6} & F_6^k - \ell F_2^k & F_5^k + \ell F_3^k \\ & & & & & & & & & & & -C_3 F_1^k & 0 & -C_2 \ell F_1^k & -\frac{F_4^k}{2} \\ & & & & & & & & & & & & -C_3 F_1^k & -\frac{F_4^k}{2} & C_2 \ell F_1^k \\ & & & & & & & & & & & & & -C_1 \ell^2 F_1^k & 0 \\ & & & & & & & & & & & & & & -C_1 \ell^2 F_1^k \end{bmatrix} \quad (\text{B.2})$$

symmetric

with:

$$C_1 = \left(\frac{6}{5\ell} + \frac{12I^k}{A^k \ell^3} \right), \quad C_2 = \left(\frac{1}{10} + \frac{6I^k}{A^k \ell^2} \right), \quad C_3 = \left(\frac{2\ell}{15} + \frac{4I^k}{A^k \ell} \right) \quad \text{and} \quad C_4 = \left(\frac{\ell}{30} - \frac{2I^k}{A^k \ell} \right)$$

B.3.

Mass Matrix

The layer mass matrix is obtained by solving integrals in Eq. (42) in closed form, as follows:

$$\begin{matrix}
 M^k = \bar{m}^k & \left[\begin{array}{cccccccccccc}
 \frac{1}{3} & 0 & 0 & 0 & 0 & 0 & \frac{1}{6} & 0 & 0 & 0 & 0 & 0 \\
 C_1 & 0 & 0 & 0 & C_2 & 0 & C_3 & 0 & 0 & 0 & C_4 & \\
 & C_1 & 0 & -C_2 & 0 & 0 & 0 & C_3 & 0 & -C_4 & 0 & \\
 & & \frac{2I}{3A} & 0 & 0 & 0 & 0 & 0 & \frac{I}{3A} & 0 & 0 & \\
 & & & C_5 & 0 & 0 & 0 & C_4 & 0 & -C_6 & 0 & \\
 & & & & C_5 & 0 & -C_4 & 0 & 0 & 0 & -C_6 & \\
 & & & & & \frac{1}{3} & 0 & 0 & 0 & 0 & 0 & \\
 & & & & & & C_1 & 0 & 0 & 0 & -C_2 & \\
 & & & & & & & C_1 & 0 & C_2 & 0 & \\
 & & & & & & & & \frac{2I}{3A} & 0 & 0 & \\
 & & & & & & & & & C_5 & 0 & \\
 & & & & & & & & & & C_5 & \\
 \text{symmetric} & & & & & & & & & & & \\
 & & & & & & & & & & & C_5
 \end{array} \right]
 \end{matrix} \tag{B.3}$$

where:

$$\bar{m}^k = \rho^k V^k, \quad C_1 = \left(\frac{13}{35} + \frac{6I^k}{5A^k \ell^2} \right), \quad C_2 = \left(\frac{11\ell}{210} + \frac{I^k}{10A^k \ell} \right), \quad C_3 = \left(\frac{9}{70} - \frac{6I^k}{5A^k \ell^2} \right), \quad C_4 = \left(\frac{I^k}{10A^k \ell} - \frac{13\ell}{420} \right), \quad C_5 = \left(\frac{\ell^2}{105} + \frac{2I^k}{15A^k} \right), \quad \text{and} \quad C_6 = \left(\frac{\ell^2}{140} + \frac{I^k}{30A^k} \right)$$

with V^k being the volume of layer- k .

